NUMERICAL INVESTIGATION OF COMPLEX HYDRAULIC FRACTURE NETWORK PROPAGATION IN LAMINATED, NATURALLY FRACTURED RESERVOIRS

A Dissertation

by

HAN LI

Submitted to the Office of Graduate and Professional Studies of
Texas A&M University
in partial fulfillment of the requirements for the degree of

DOCTOR OF PHILOSOPHY

Chair of Committee,	Peter P. Valko
Committee Members,	Christine A. Ehlig-Economides
	Walter B. Ayers
	Benchun Duan
Head of Department,	A. Daniel Hill

December 2017

Major Subject: Petroleum Engineering

ABSTRACT

Horizontal wells with multistage hydraulic fractures (HFs) are required for maximizing the oil and gas production from unconventional reservoirs. Since the characterization of complex fracture geometry with high accuracy is still challenging by fracture diagnostic techniques such as microseismic event interpretation, modeling approaches of complex hydraulic fracture propagation become powerful tools for predicting complex fracture geometry and optimizing hydrocarbon production.

In this research, a novel two–dimensional (2D) finite–discrete element model (FDEM) was developed to describe complex fracture propagation in unconventional formations. This coupled fluid flow and geomechanics model can also be applied for multi–fracture, multi–well scenarios. Key physical processes for complex hydraulic fracture propagation in unconventional reservoirs, including hydraulic fracture–natural fracture (NF) interaction, stress shadow effect, hydraulic fracture–bedding plane (BP) interaction, fluid flow in fracture network, leak–off from fracture network, mechanical anisotropy of formations, etc., were successfully incorporated into the model.

The numerical model was utilized to investigate physical mechanisms of complex fracture propagation and offers insights for optimizing hydraulic fracturing treatments design. For multi–fracture propagation scenarios, stress shadow effect induced by opening fractures can affect the propagation direction of fractures, and non–planar fracture geometry may emerge resulting from the effect.

NFs play an important role during the evolution of fracture network geometry. With the increase of initial horizontal stress difference and the angle of NFs, the fracture tends to cross the NFs instead of opening them. For cases with small horizontal stress difference, when there is only one set of NFs with narrow range of strike orientation in the formation, fractures tend to propagate along the strike orientation of NFs. However, for cases with more than one set of NFs, the course of events is more difficult to predict.

Laminated bedding in shale formations typically result in anisotropic elastic properties, including Young's modulus and the Poisson's ratio. This fact highly influences the hydraulic fracturing treatment execution. The lamina can confine the hydraulic fracture height, but sometimes they can act as potential fracture propagation paths. Our simulation results show that without considering the mechanical anisotropy effect, the treatment design will be corrupted by the inaccurate prediction of fracture height. Different BP properties, including strength, dip angle, permeability–thickness, etc., also have strong influence on the predicted fracture height.

We also consider fracture height growth in multi–fracture schemes, when the stress shadow effects give rise to non–planar vertical growth and possible fracture branching. The simulations show that hydraulic fracture height growth is substantially restricted in laminated formations.

This work provides a framework for more realistic prediction of complex fracture geometry in unconventional formations that are laminated and naturally fractured. The results offer comprehensive insights for optimizing hydraulic fracturing treatment design.

DEDICATION

To my advisor, committee members and my family for their help and support

ACKNOWLEDGMENTS

I would like to thank my advisor, Dr. Peter Valko, and my committee members, Dr. Christine Economides, Dr. Walter Ayers and Dr. Benchun Duan, for their guidance and support throughout the course of this research.

Thanks also go to my friends and colleagues and the department faculty and staff in Petroleum Engineering Department for making my time at Texas A&M University a great experience.

Finally, thanks to my mother and father for their encouragement and to my wife for her patience and love.

CONTRIBUTORS AND FUNDING SOURCES

Contributors

This work was supervised by a dissertation committee consisting of Professor Peter Valko and Walter Ayers of the Department of Petroleum Engineering, Professor Benchun Duan of the Department of Geophysics, and Professor Christine Ehlig-Economides of the Department of Petroleum Engineering at University of Houston.

All work for the dissertation was completed by Han Li, in collaboration with Dr. Yushi Zou of the Unconventional Natural Gas Institute at China University of Petroleum Beijing.

Funding Sources

Graduate study was supported by a graduate research assistantship from Texas A&M University.

NOMENCLATURE

w	Fracture width/crack opening, m
E	Young's modulus, Pa
P	Pressure, Pa
t	Time, s
v	Poisson's ratio
h_f	Fracture height, m
x_f	Fracture half length, m
u	Displacement, m
u_c	Continuous displacement, m
u_{enrich}	Enriched displacement, m
μ	Fluid viscosity, Pa.s
Q	Injection volumetric flow rate, m^2/s
q_m	Leak–off rate per unit length into matrix rocks, m/s
q_{lbp}	Leak–off rate per unit length through intact bedding planes, m/s
q_{lnf}	Leak–off rate per unit length through intact natural fractures, m/s
C_t	Total compressibility of the reservoir, Pa^{-1}
φ	Reservoir porosity, dimensionless
μ_f	Fracturing fluid viscosity, Pa.s
μ_r	Reservoir fluid viscosity, Pa.s

w_0	Unbroken fracture aperture, m
σ_{ij}	Cauchy tensor, Pa
b_i	Body force, N
ρ	Density, kg/m^3
c	Damping factor, dimensionless
ε_{ij}	Strain, dimensionless
D_{ijst}	Elasticity tensor, Pa^{-1}
E_h	Young's modulus in horizontal direction, Pa
E_v	Young's modulus in vertical direction, Pa
v_h	Poisson's ratio in horizontal direction, dimensionless
v_v	Poisson's ratio in vertical direction, dimensionless
G	Shear modulus, Pa
k	Stiffness, N/m
k_n	Normal stiffness, N/m
k_s	Shear stiffness, N/m
m	Mass, kg
A	Contact area, m^2
L	Characteristic length of a contact plane, m^2
B_0	Pseudo block size, m
T_0	Tensile strength, Pa
S_0	Cohesion, Pa
ϑ	Internal friction angle, degree

φ_j^e	Approximation function at node j
w_i	Weight function, dimensionless
Ω	Domain, dimensionless
$[K^e]$	Coefficient matrix, $m^2 . s^{-1} . Pa^{-1}$
$\{f^e\}$	Column vector, m^2/s
h_e	Element size, m
N_i	Shape function, dimensionless
$\triangle X$	Change of the displacement
$[M^e]$	Mass matrix, kg
$[C^e]$	Damping matrix, dimensionless
c_0	Damping coefficient, dimensionless
ε	Convergence threshold, dimensionless
σ_h	Minimum horizontal stress, Pa
σ_H	Maximum horizontal stress, Pa
σ_v	Vertical stress, Pa
S_{nf}	Cohesion of natural fractures, Pa
ϑ_{nf}	Internal friction angle of natural fractures, degree
A_{eff}	Effective fractured area, m^2
α	Power law exponent, dimensionless
K_0	Mechanical anisotropy factor, dimensionless

TABLE OF CONTENTS

Page

LIST OF FIGURES

Page

LIST OF TABLES

Page

1. INTRODUCTION

1.1 Background

Hydraulic fracturing as a method for production stimulation in oil and industry dates to the 1930s. The first non–acid hydraulic fracturing experiment was applied in 1947, which marked the beginning of hydraulic fracturing, and the technique was successfully commercialized in 1950 (Veatch et al. 1989). Today, more than a million wells in the U.S. have been subjected to hydraulic fracturing (Klopott 2015). In recent years, combining horizontal wells with hydraulic fracturing has significantly impacted on oil and gas industry. The Society of Petroleum Engineers has estimated that 2.5 million of fracturing treatments have been conducted world–wide, and tens of thousands of horizontal wells have been drilled in the past 60 years (King 2012).

Although affected by recent decline in oil prices, tight oil production in the U.S. was 4.9 million barrels per day (b/d) in 2015 and contributed to 52.1% of total crude oil production, which was 9.4 million b/d in 2015 (Energy Information Administration 2016). EIA predicted that shale gas production will continually increase, and become a major contribution to dry natural gas production in the U.S. (**Fig. 1**) (Energy Information Administration 2017). Dong et al. (2011) conducted a global estimation of unconventional gas in–place (OGIP) and conventional hydrocarbons (oil and gas) in–place in seven regions around the world (**Fig. 2)**. They showed that unconventional OGIP is significantly greater than conventional OGIP, and it continues to be discovered throughout the world.

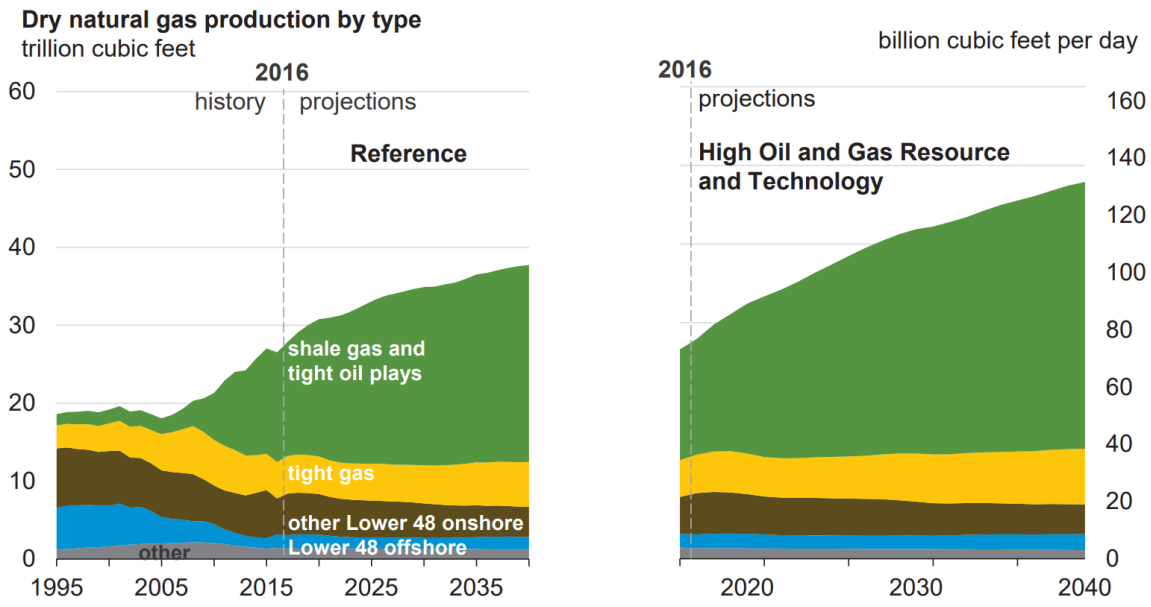

Fig. 1-Forecast of U.S. dry natural gas production (U.S. Energy Information Administration, Annual Energy Outlook 2017) (https://www.eia.gov/outlooks/aeo/pdf/0383(2017).pdf).

Region	Total unconventional OGIP, Tcf			Conventional hydrocarbons (oil plus gas) in-place, Tcfe		
	P90	P50	P10	P90	P50	P10
CIS	29,623	45,343	65,197	4,111	5,997	12,154
MET	21,330	30,872	44,718	8,047	11,900	24,612
NAM	11,833	18,318	27,787	14,661	20,693	39,788
AAO	6,108	10,291	16,217	4,903	7,605	16,805
AFR	5,461	7,901	11,428	19,303	29,699	64,922
LAM	4,957	7,122	10,283	2,422	3,552	7,252
EUP	4,066	5,895	8,592	4,822	7,404	16,139
World	83,378	125,742	184,222	58,268	86,850	181,671

Fig. 2-Summary of conventional hydrocarbon and unconventional gas by region (Dong et al. 2011).

1.2 Statement of the problem

In unconventional reservoirs, the combination of horizontal drilling and multistage hydraulic fracturing have been demonstrated as a highly effective completion method (Bunger et al. 2012). However, complex heterogenetic geological properties of unconventional reservoirs and diversified designs of hydraulic fracturing treatments have a lot to be investigated. Several aspects, including design and evaluation of hydraulic fracturing treatments, understanding of rock deformation, fluid flow in fractures, and understanding of typical fracture geometry including fracture width, length and height, are crucial to improve quality of reservoir stimulation. Stress shadow effect between fractures during pumping in unconventional reservoirs can result in a complex fracture network rather than a simple bi–wing planar fracture (Roussel and Sharma 2010; Wu et al. 2014). In addition, pre–existing NFs and laminated structures in unconventional reservoirs play a key role for affecting fracture geometry and raise the possibility of generating complex fracture networks (Kresse et al. 2013a).

While characterization of complex fracture geometry by fracture diagnostic techniques is a controversial tool, non–uniqueness is still a problem (Cipolla 2000). The accuracy of microseismic event interpretation is controversial, and the characterization of opening fractures induced by tensile failure is even more complicated when relying only on microseismic event interpretation (Eisner et al. 2011). Therefore, realistic modeling of complex hydraulic fracture propagation is indispensable for predicting complex fracture geometry and optimizing hydrocarbon production.

Researchers have been developing hydraulic fracturing models for decades (Olson 2008; Cheng 2009; Roussel and Sharma 2011; Perkins and Kern 1961). Classical hydraulic fracture propagation models, such as PK and KGD models (Perkins and Kern 1961; Khristianovich et al. 1955), can describe the evolution of planar bi–wing fractures, based on the assumption of 2D plane strain theory. These pioneering works have significantly impacted this field and still can be applied in various situations. However, for unconventional reservoir stimulation, the conventional fracture models are of limited use, because they are unable to simulate the development of the complex fracture network. In unconventional reservoirs, the role of the complex fracture network is crucial. Propagation direction, fracture branching and similar phenomena are influenced by mechanical interaction between distinct hydraulic fractures, as well as with pre–existing NFs and BPs. Therefore, modeling the hydraulic fracturing process in such formations should emphasize the network development. Moreover, heterogeneity of unconventional formations may result in anisotropy of rock properties, including Young's modulus, Poisson's ratio, and permeability. Conventional hydraulic fracturing models are not designed to include such effects, driving researchers to develop advanced models to overcome the limitations of the classical models.

1.3 Research objectives

There are two main objectives of this research. Firstly, we wish to improve a coupled fluid flow and rock deformation fracture propagation model for simulating complex fracture propagation in naturally fractured, laminated unconventional reservoirs. This is achieved by streamlining and optimization of the finite–discrete element solution

algorithm and constructing new modules for BPs, mechanical anisotropy of the formations, building discretized natural fracture sets, etc.

Second, we wish to investigate the fundamental mechanisms of complex hydraulic fracture propagation under realistic conditions, to optimize completion design. In details, investigation was conducted for studying complex fracture propagation in naturally, fractured reservoirs. We developed a NF network builder to represent the NFs network considering all available observations. Moreover, we studied single and multiple fractures growth in laminated unconventional reservoirs, to investigate HF–BP interaction under different scenarios.

1.4 Overview of the development of laminated, naturally fractured reservoirs

Multi–stage, multi–well hydraulic fracturing with horizontal wells has been demonstrated as an effective technique for the development of unconventional reservoirs (Bunger et al. 2012). However, the hydraulic fracturing process becomes very complex due to the rock heterogeneity and complex discontinuous rock structure of unconventional reservoirs. Particularly, pre–existing NFs and laminated structures of formations are commonly in unconventional reservoirs, and they play key roles on rock properties and hydraulic fracture pattern evolution. Pre–existing NFs and fine lamination commonly exist in the Eagle Ford formation (Suppachoknirun et al. 2016). The existence of horizontal microfractures results in relatively low tensile strength of rock in the Eagle Ford formation (Padin et al. 2016). McGinley et al. (2015) stated that Young's modulus and Poisson's ratio are directionally–sensitive in laminated formations such as the Marcellus, and fracture conductivity is highly affected by fracture orientation only when anisotropy of the

rock's mechanical properties is pronounced. Tavallali et al. (2010) conducted Brazilian tests on layered sandstone, and concluded that layer orientation has a deterministic effect on fracture pattern. In details, when fracture is initiated aligned with BPs, fracture cleanly propagate along the interface. When fracture propagates perpendicular to the BPs, vertical fractures are formed, and they are appeared to be tortuous. AlTammar et al. (2017) conducted experimental studies to investigate the effect of laminated structures on hydraulic fracture initiation and propagation. They found that a fracture tends to initiate and propagate parallel to BPs interfaces under small far–field differential stress.

NFs are classified based on the displacement direction relative to the orientation of the discontinuity (Pollard et al. 1988). Terms joint or vein suggest for a NF formed predominantly by mode I movement. A fault is a discrete fracture formed predominantly by mode II and/or mode III movements (Gale et al. 2014). Three modes of fracture surface displacement are illustrated in **Fig. 3** (Philipp et al. 2013). Dershowitz and Doe (2011) concluded that NFs have three major influences on the exploration of unconventional shale reservoirs. First, NFs act as weak planes that may affect HF propagation path; second, slip on NFs caused by high pressures from hydraulic fracturing treatments can increase their conductivity; and third, conductive pre–existing NFs can expand wells' drainage volume. Pre–existing NFs are usually characterized by their size, occurrence, orientation, intensity, aperture width and numbers of pattern etc. (Gale et al. 2014). Typical techniques and tools for characterization of NFs are CT scanning, reservoir models, wireline logs, outcrops observation, image logs, production logging tools, and well test data etc. (Hussain et al. 2016). Gale et al. (2014) summarized the occurrence of different types of natural fractures

in eighteen shale formations based on outcrop and observation of core samples. An overview is presented in **Table 1**. It shows that all common types of NFs can be observed in a wide range of shale formations.

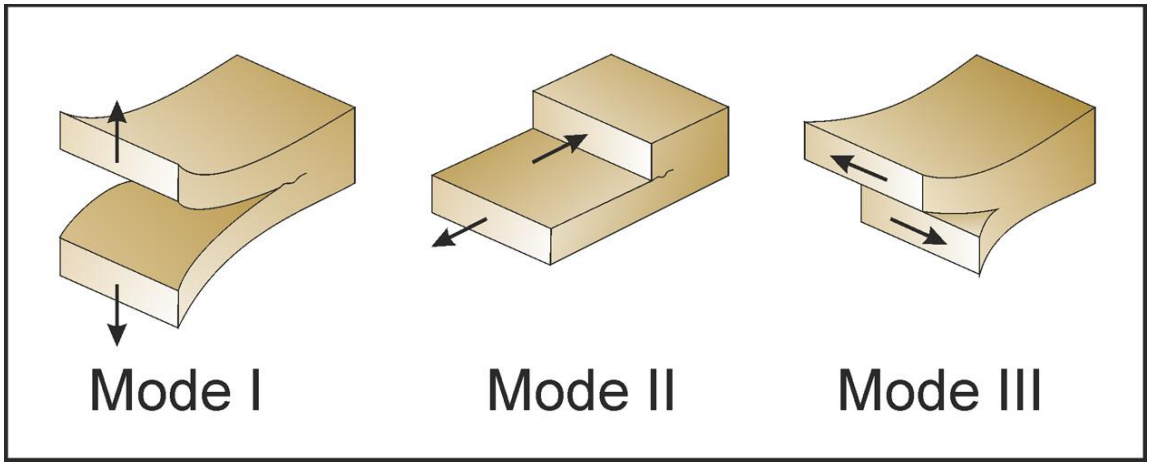

Fig. 3-Three loading modes of cracked specimens: mode I: tensile opening; mode II: in–plane shearing; and mode III: anti–plane shearing (Philipp et al. 2013).

Mode	Fracture type	The number of formations containing this type
Opening mode	Fractures at a high angle to bedding (mostly sub–vertical)	18
Shear mode	Bedding parallel	14
	Compacted	7
	Faults	13

Table 1-Overview of data from eighteen shale formations based on core samples and outcrop (Gale et al. 2014).

Mechanical anisotropy of shales is resulted from the existence of different types of cementation sediments between shale layers during the compaction process (Zhou et al. 2016). Typically, horizontal Young's modulus (E_h) is higher than vertical Young's modulus (E_v), and horizontal Poisson's ratio (V_h) is higher than vertical Poisson's ratio (V_v) (Li et al. 2016a). Variation in mineral composition and fabric properties highly affect elastic properties, and it can result in stress anisotropy in unconventional reservoirs (Sone 2012). Unconventional laminated rock typically exhibits anisotropy in different scales, ranging from microscopic to macroscopic (Hamza et al. 2015). Ouchi et al. (2017) stated that crack branching and diversion are resulted from variations in elastic moduli and stress concentration at grain scale. They concluded that complex fracture geometry and

surrounding damage zone can be caused by the contrasts in mineral grains' mechanical properties and their pattern and distribution. Li et al. (2016a) investigated the effect of mechanical anisotropy of formations on fracture initiation pattern and pressure. As can be seen in **Fig. 4**, mechanical anisotropy of formations highly affects the initiation pressure of transverse fractures and longitudinal fracture under different perforation depth.

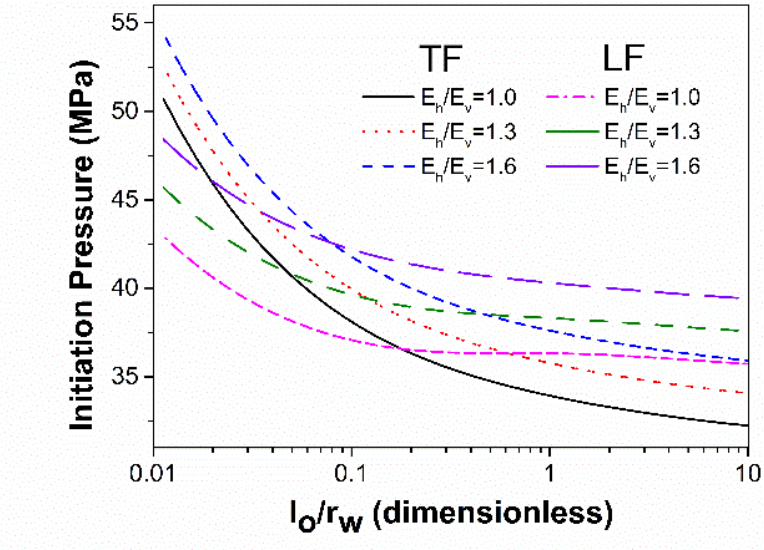

Fig. 4-The effect of E_h/E_v on fracture initiation pressures under different perforation depth for elastic anisotropic cases (Li et al. 2016a).

Zhou et al. (2016) stated that laminated structures with high dip were observed in Lujiaping shale gas formation. In this formation, pre–existing NFs and BPs were highly developed. Dip and dip angles significantly change with the change of the formation depth **(Fig. 5)**.

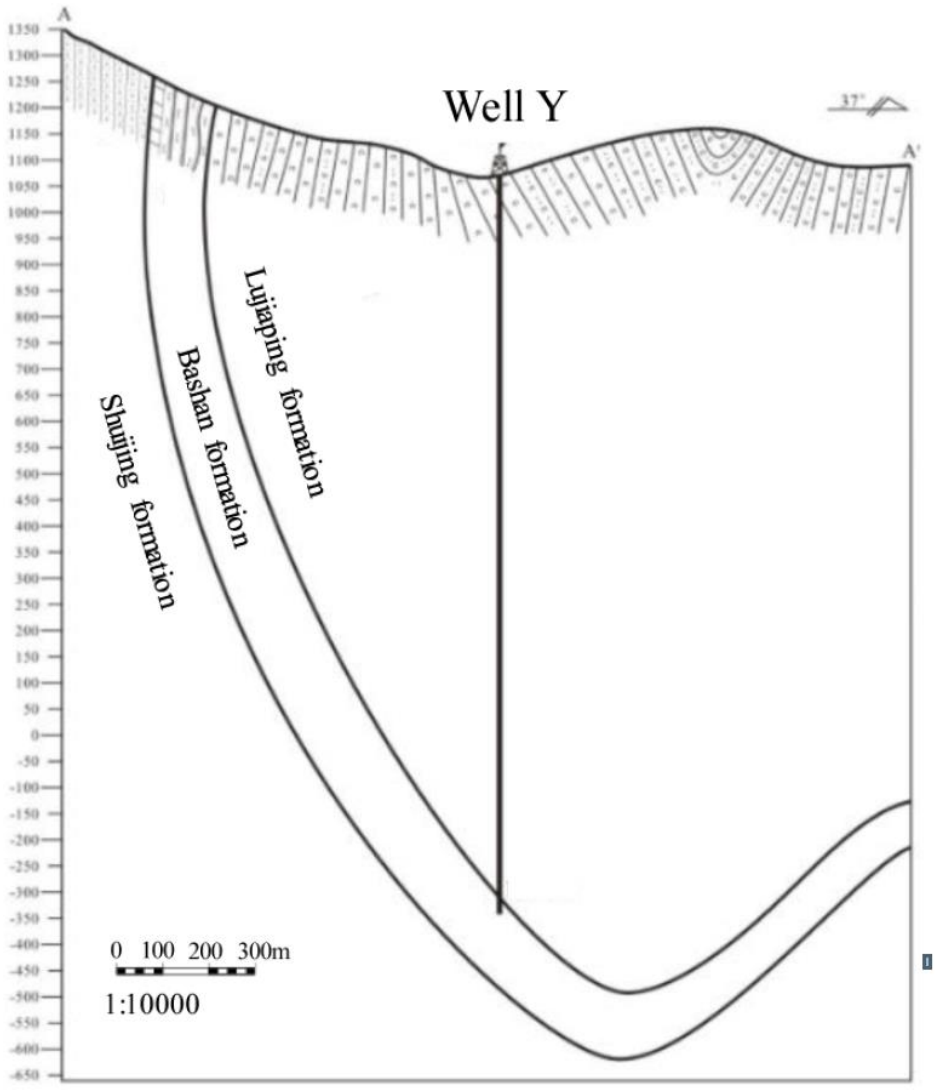

Fig. 5-Regional geological cross section of the Liujiaping formation at well Y (Zhou et al. 2016).

1.5 Review of fracture propagation models

For several decades, researchers have been developing hydraulic fracture propagation models for optimizing hydraulic fracturing treatment designs (Weng 2015). However, most of the traditional approaches consider single bi–winged planar fractures.

In unconventional reservoirs, such a configuration is unlikely to evolve. Rather, a complex fracture system develops. The required model is complex not only because of the coupling of fluid flow and rock mechanics and heterogeneity of geological structures, but also because a multiplicity of computational methods is needed for accuracy and computer efficiency. Even a basic form of hydraulic fracturing model should involve some major physical processes: Fluid flow within fractures; Rock deformation caused by fluid pressure inside fractures; Fracture propagation, and fluid leak–off into the formation etc.

For the development of hydraulic fracture propagation simulations, different numerical techniques were utilized in recent years, such as finite element method (FEM), boundary element method (BEM), discrete element method (DEM), peridynamics method, and derived and combined techniques based on the above methods. Different techniques have their own advantages and limits for various focused applications, in terms of computational efficiency, simulation scale, reservoir properties, etc.

1.5.1 Conventional hydraulic fracturing models

Hydraulic fracturing models can be classified into two–dimensional (2D) and three–dimensional (3D) models. A 2D PK fracture model developed by Perkins and Kern (1961) is one of the most well–known models which is widely used in this field. Nordgren (1972) proposed the PKN model based on PK model by considering the effects of fluid loss into the formation. The PKN model assumes constant fracture height and plane–strain condition in vertical planes that are normal to the fracture propagation direction. The vertical cross section of the fracture is of elliptical shape (**Fig. 6)**. The PKN model is a

reasonable approximation for the case when the fracture length is much larger than the height.

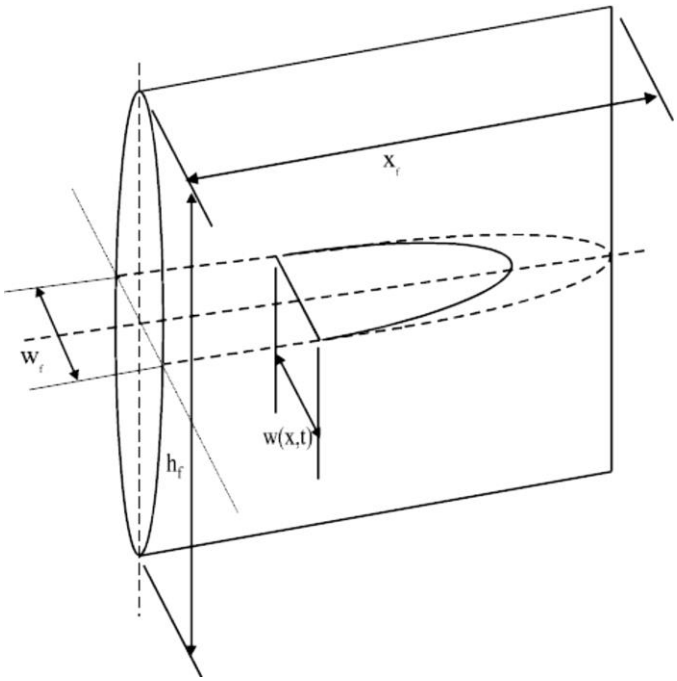

Fig. 6-Schematic illustration of PKN fracture model (Rahman et al. 2010).

The KGD model (Khristianovich et al. 1955; Geertsma et al. 1969) is another classical 2D analytical model widely used in this industry. The KGD model assumes plane–strain in the horizontal planes, constant width along the vertical direction. The horizontal cross section of the fracture is of elliptical shape (**Fig. 7**). The KGD model is considered as a good approximation for the case when the fracture height is larger than the length. Fracture height in the PKN and KGD models is assumed to be constant and

known, and both models are based on the classic Sneddon (1946) plane–strain crack analytical solution:

$$w(x) = \frac{4(1-v^2)p}{E}\sqrt{c^2 - x^2} \quad \ldots\ldots\ldots\ldots\ldots\ldots (1.1)$$

Here, $\boldsymbol{w(x)}$ is the crack opening along the coordinate $\boldsymbol{x}$, $\boldsymbol{E}$ is Young's modulus, $\boldsymbol{v}$ is Poisson's ratio, $\boldsymbol{p}$ is net pressure within the crack, and $\boldsymbol{c}$ is crack half length. In the PKN approach, $\boldsymbol{c}$ is identified with $h_f/2$ and in the KGD approach it is taken as x_f.

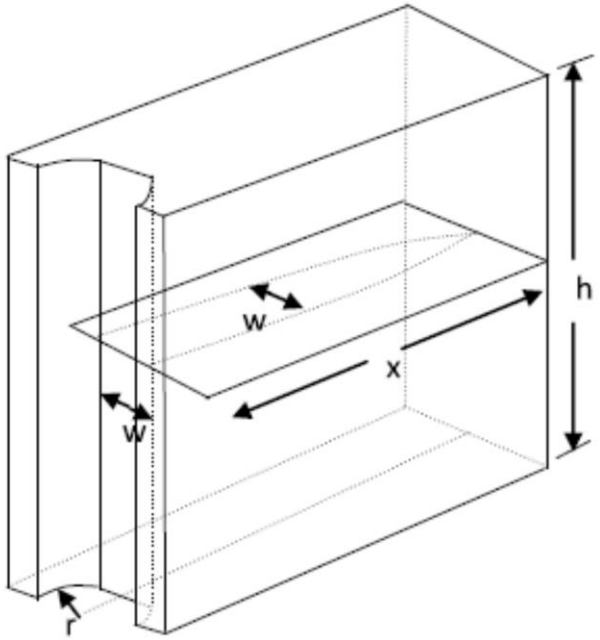

Fig. 7-Schematic illustration of KGD fracture model (Rahman et al. 2010).

3D hydraulic fracturing models have been developed to simulate more realistic fracture propagation scenarios. These models include fracture height growth with the injection of fracturing fluid. Settari et al. (1982) developed a pseudo–3D model with the incorporation of lateral fluid flow, fracture opening and coupling with a scheme to process fracture growth at each cross section into the model (**Fig. 8**). For this model, finite differences method is utilized to solve equations for lateral flow, and the vertical propagation problem is solved by numerical implementation of a singular integral equation on a suitable set of Chebyshev points.

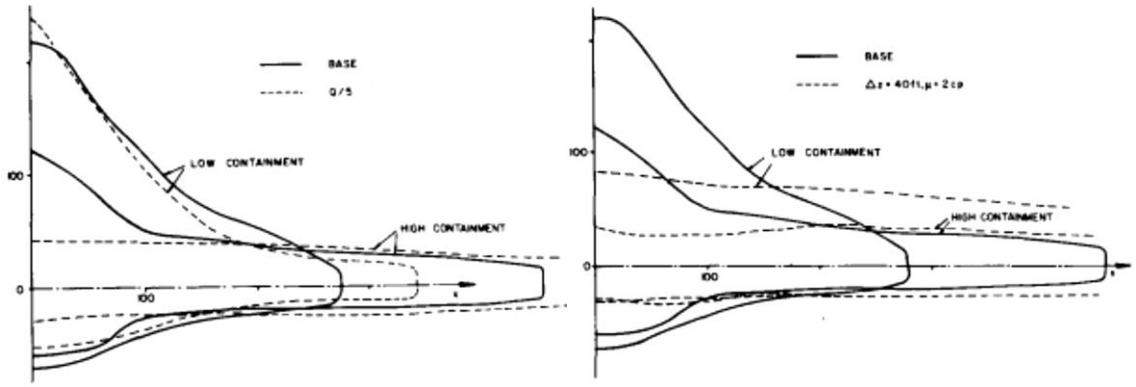

Fig. 8-Fracture propagation maps with different properties. (Left): effect of reduced pumping rate. (Right): effect of reservoir thickness (Settari et al. 1982).

Pseudo–3D models are approximate but efficient to capture the behavior of fracture height growth by employing special schemes. Castonguay et al. (2013) developed a fully 3D propagation model by using BEM. In this model, multiple fractures can

propagate simultaneously, and non–planar fractures are formed because of stress shadow effect induced by opening fractures (**Fig. 9**).

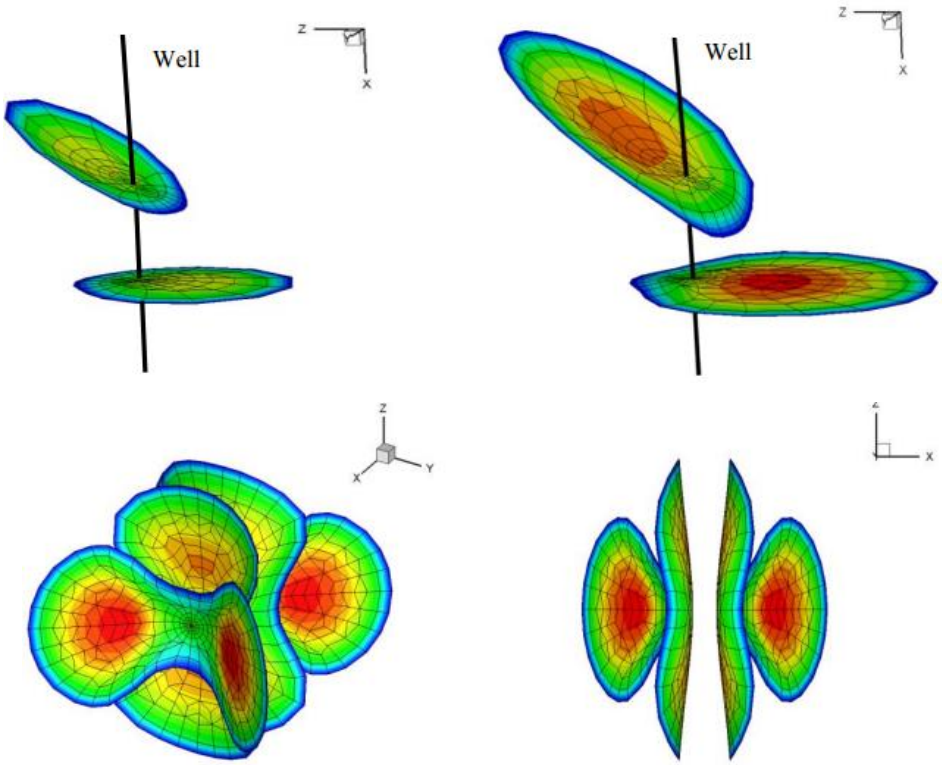

Fig. 9-3D Multi–fracture propagation for different cases (Castonguay et al. 2013).

1.5.2 Modeling of complex fracture propagation in unconventional reservoirs

For the models mentioned above, the critical issue is the interaction of HFs and NFs (Weng 2015). Several important physical processes should be incorporated into these types of models, such as fluid flow in fracture networks, interaction between various HFs

(stress shadow effect), interaction between HFs and NFs, interaction between HFs and BFs, and proppant transport in fracture networks, etc.

Various models for simulating complex fracture networks have been developed in recent years. Meyer and Bazan (2011) developed a lumped elliptic P3D models with discretized fracture networks. This model consists of two orthogonal sets of parallel uniformly spaced fractures, in the directions of maximum and minimum horizontal stresses (**Fig. 10**). Extended frictional pressure loss in the wellbore, wellbore storage effect and other important engineering effects are incorporated in the model, and proppant transport in the fracture networks is also considered. The model does not involve interaction between the HFs and NFs.

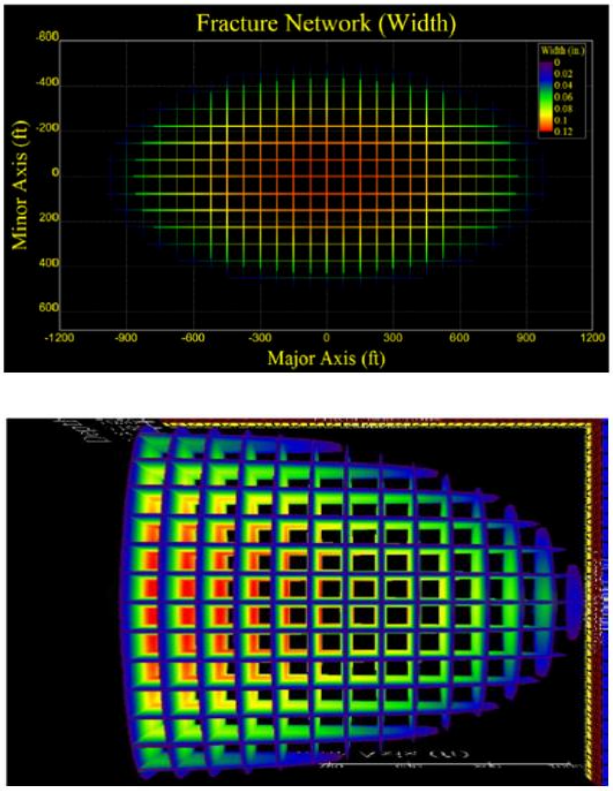

Fig. 10-2D (x–y plane) and 3D (x–y plane) aerial views of fracture network by Meyer and Bazan (2011).

Kresse et al. (2013b) developed a Pseudo–3D based complex fracture network model, which is called the UFM model, to simulate complex fracture propagation in naturally fractured reservoirs. For this model, 2D plane strain assumption is made for each vertical cross section. A fracture is divided into numbers of cells along the fracture length and each cell has different fracture height. The system of equations is solved using the damped Newton–Raphson method to obtain the new pressure and flow distribution (Kresse et al. 2013b). Weng et al. (2015) summarized this example, and integrated them with the microseismic events of the examples, which is presented in **Fig. 11**.

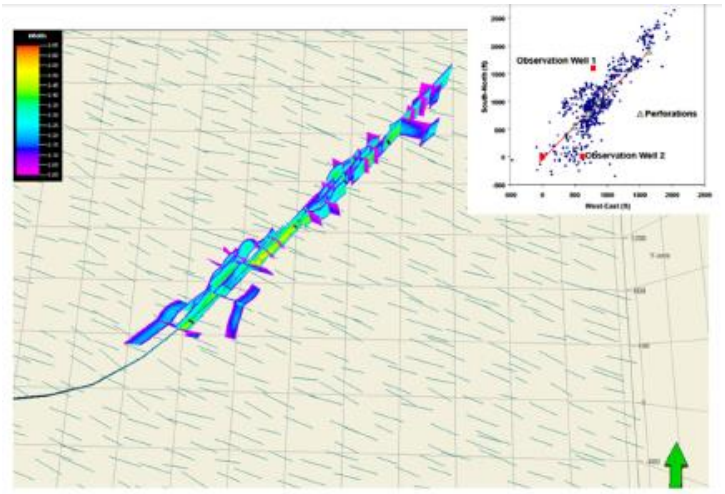

(a) Crosslinked gel treatment.

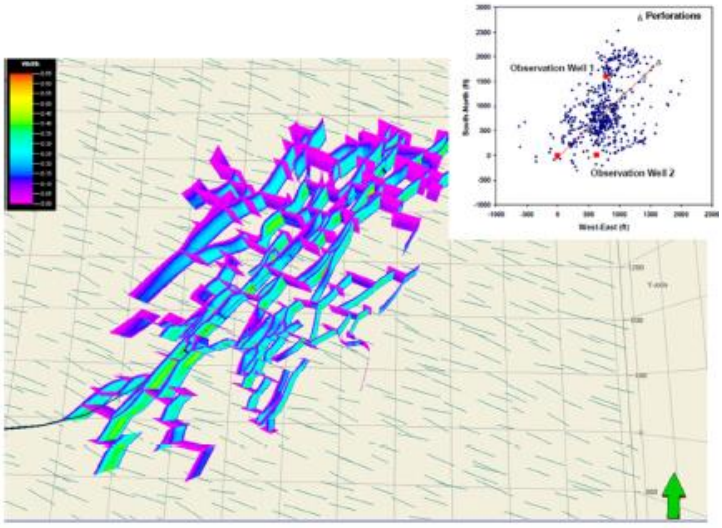

(b) Slickwater refracturing.

Fig. 11-Inferred hydraulic fracture network simulated by the UFM model for Barnett Shale; thin blue lines represent traces of the NFs on a horizontal plane (Weng et al. 2015). The insets of the microseismic map are from Warpinski et al. (2005).

The discrete element method (DEM) was introduced by Cundall (1971), as a numerical technique to simulate mechanical behavior of discontinuous rock masses

(Cundall 1971). Compared with the existing continuum theories, DEM provides a different path that is capable for handling discontinuous problems (Lemos 2011). Itasca Consulting group produced two popular codes based on DEM, Universal Distinct Element Code, and (UDEC) and Three–Dimensional Distinct Element Code (3DEC), for modeling mechanical, structural and fluid flow behaviors of discontinuous rock mass (Itasca 2007, 2011). In these codes, deformable or rigid blocks are subdivided in a mesh in 2D or 3D dimensions, and the interactions between two neighboring blocks are governed by normal and tangential stiffness in normal and shear directions (Israelsson 1996).

In recent years, several numerical models based on DEM were purposed by many researchers to study hydraulic fracturing propagation and microseismic observations (Zhao et al. 2014; Nagel et al. 2012). Fu et al. (2011) purposed a FDEM model which is capable of modeling new fracture initiation and propagation through the DEM blocks by incorporating an adaptive remeshing module. In the model, fractures are treated as mechanical joint elements (**Fig. 12)**. A FDEM based code, called Y–Geo, was developed by a group of researchers for geomechanical applications (Mahabadi et al. 2012; Lisjak et al. 2014). The simulation model includes several features, such as material heterogeneity, rock joint shear strength criterion, a materials mapping function for an exact representation of heterogeneous models, and a quasi–static friction law etc.

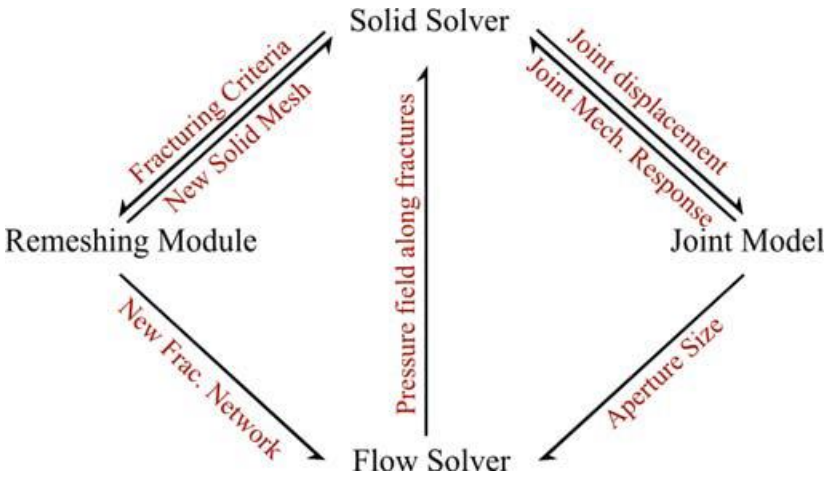

Fig. 12-Information exchange between important modules in FDEM simulations (Fu et al. 2011).

McClure (2012) developed a coupled fluid flow and rock deformation model to simulate hydraulic fracture propagating in naturally fractured reservoirs based on a developed discrete fracture network. The induced stresses are calculated by the displacement discontinuity method. The model is capable of modeling hydraulic fracture–natural fracture interaction, and investigating the induced seismicity during fracture evolution.

The extended finite element method (XFEM) developed based on traditional FEM, and finite element space is enriched by additional functions (Moës et al. 1999):

$$u = u_c + u_{enrich} \quad (1.2)$$

Here $\boldsymbol{u_c}$ is the continuous displacement field and $\boldsymbol{u_{enrich}}$ is the enriched displacement field. As a result, crack can propagate independently of the mesh configuration by minimal remeshing. Taleghani et al. (2009) developed a 2D XFEM model to simulate hydraulic

fracture interaction with natural fractures. Moës et al. (2002) developed a 3D model by combining XFEM formulation with level set method to simulate non–planar fracture growth. The fracture can be updated or evolve by just changing the level sets without remeshing.

1.6 Outline of the dissertation

The main objective of this dissertation is to investigate complex fracture network propagation in laminated, naturally fractured reservoirs. Section 2 presents the methodology and physical processes of the FDEM model. Section 3 validates the simulation. Section 4–6 investigate single fracture and complex fracture networks propagation in homogenous, naturally fractured, and laminated reservoirs respectively. Section 7 summarizes the conclusions of this research work. This work is about characterizing the important factors affecting hydraulic fracture growth and predicting fracture network geometry under different geological and operational scenarios, and it provides some unique insights for optimizing hydraulic fracturing treatment designs for the development of unconventional reservoirs.

Section 2 introduces the mechanisms and meshing strategy of the finite–discrete element model. Governing equations regarding fluid flow, rock deformation, mechanical interaction between contacted elements, and rock failure criteria etc. are introduced in this section. The numerical algorithm and coupling mechanisms are illustrated by following the finite–discrete element architecture.

Section 3 focuses on the details for the validation of the model which is described in section 2. Firstly, following the tradition in the field of hydraulic fracturing propagation

simulator development, the classical 2D PKN model is utilized to validate the simulation. Comparison of the evolution of fracture half length, wellbore maximum fracture width and wellbore net pressure between the FDEM model and 2D PKN model are discussed. Secondly, simulations for a bi–wing HF intersecting two NFs were conducted to compare the simulation results with published experimental results.

Section 4 presents the results of multiple fracture propagation in unconventional reservoirs. Several sensitivity studies have been conducted to investigate the fracture propagation behavior under different geological and operational circumstances. Moreover, fracture propagation simulations have been conducted based on several modern hydraulic fracturing strategies, such as sequential fracturing and alternating fracturing, to analyze fracture propagation and optimize hydraulic fracturing design.

Section 5 discusses single fracture and complex fracture network propagation in naturally fractured reservoirs. Simulations of single fracture and multiple fractures interacting with NFs under different geological and operational scenarios were conducted. Moreover, a discrete natural fracture builder was developed, capable to construct a discrete NF network based on geological observations.

Section 6 presents the investigation of HF propagation in laminated unconventional reservoirs. Simulations of single fracture and multiple fractures interacting with BP interfaces under different geological and operational scenarios were conducted. A novel multi–fracture, multi–stage fracture design is proposed, which can create larger Stimulated Reservoir Volume (SRV) than classical Texas two–steps techniques in laminated shale formations under some specific scenarios.

The last section outlines the main results obtained from the numerical investigation and provides the conclusions of the research.

2. FRACTURE PROPAGATION MODEL*

2.1 Introduction

In recent years, complex fracture propagation models have been developed for understanding the fracture propagation mechanisms and providing important insights for optimizing hydraulic fracturing designs. Developing complex fracture propagation models which are capable for simulating fracture propagation in laminated, naturally fractured reservoirs has become a hot discipline in oil and gas industries, because these models can simulate more realistic fracture propagation behavior in complex unconventional reservoirs. This section introduces details of the mechanisms of the novel complex fracture propagation model that is based on the finite–discrete element method.

The finite–discrete element model is a 2D coupled fluid flow and rock deformation model for simulating complex fracture propagation in unconventional reservoirs. It is capable of modeling single and multiple fracture propagation in laminated reservoirs and naturally fractured reservoirs. The algorithms, including governing equations, coupling schemes, contact functionalities, and failure criteria, etc. are explained in detail.

2.2 Finite−discrete element simulation

Pioneered by Munjiza et al. (1995), FDEM is a numerical technique that is capable of modeling physical behavior of the transition from continuum systems to discontinuous

* Part of this section is reprinted with permission from "Hydraulic Fracture Height Predictions in Laminated Shale Formations Using Finite Element Discrete Element Method" by Li, H., Zou, Y., Valko, P.P. and Ehlig-Economides, C.A. Paper SPE 179129 presented at the SPE Hydraulic Fracturing Technology Conference, The Woodlands, Texas, USA. 9-11 February.

systems. In FDEM, simulation domain is discretized into elements. Neighboring elements do not share a node, and contact techniques are utilized to process the interaction between neighboring elements (Sun et al. 2016). Compared with some traditional numerical methods, FDEM is designed to process both continuous and discontinuous mechanical behavior of materials which overcomes the limit of continuum codes. Due to the discontinuous nature of rocks in unconventional reservoirs, FDEM is one of the prime numerical technique to simulate complex fracture propagation in unconventional reservoirs (Lemos 2011).

FDEM has been developed for geomchanical application, including rock damage, frictional interaction between rock blocks, and material nonlinearity etc. (Itasca 2007, 2011; Zivaljic et al. 2013). Ma et al. (2014) utilized a combined FDEM model to simulate materials behavior under tri–axial loading. Damjanac et al. (2007) used Itasca PFC and UDEC software to investigate micro–mechanical behavior of lithophysal rocks. Zhao et al. (2014) developed a 2D FDEM code to model hydraulic fracture propagation and associated microseismic activities. Moreover, DEM has been widely applied to many fields in science and engineering, including concrete dam foundations, underground evacuation in rocks, masonry structures, etc. (Lemos 2011).

This section describes the 2D finite–discrete element model used. **Fig. 13** shows the basic idea of the model.

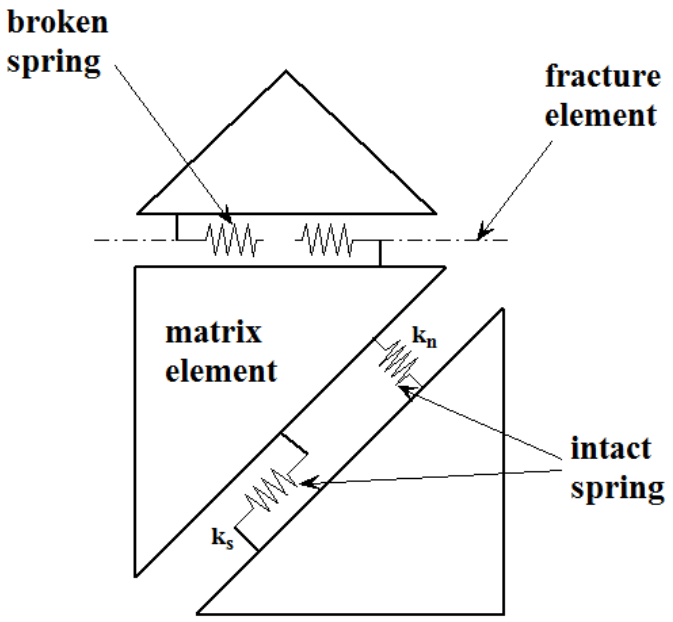

Fig. 13-Schematic of combined model of the finite–discrete element method.

The simulation domain is discretized to matrix elements. Neighboring rock matrix elements are connected by two virtual springs that are charged for tension and shear stresses, and account for strain delivery. The failure of the spring represents the creation of a fracture element between the matrix elements. Connected fracture elements then provide a continuous flow network. For typical finite element models, neighboring three–node triangular elements share two nodes during the simulation, representing continuous behavior of materials. However, as presented in **Fig. 13**, DEM has different meshing strategy. **Fig. 14** shows two neighboring elements with their vortices labeled. For instance, at the initial state, nodes 2 and 4 have the same location, which suggests that the width between two elements boundary is 0. We say that nodes 2 and 4 are in the same nodal

group A (nodal group B has other two nodes: 3 and 5). After boundary conditions are applied and mechanical analysis starts, nodes in the same nodal group may have different coordinates and designated mass, and the relative location of nodes in the same nodal group are determined by the mechanical interaction between neighboring elements.

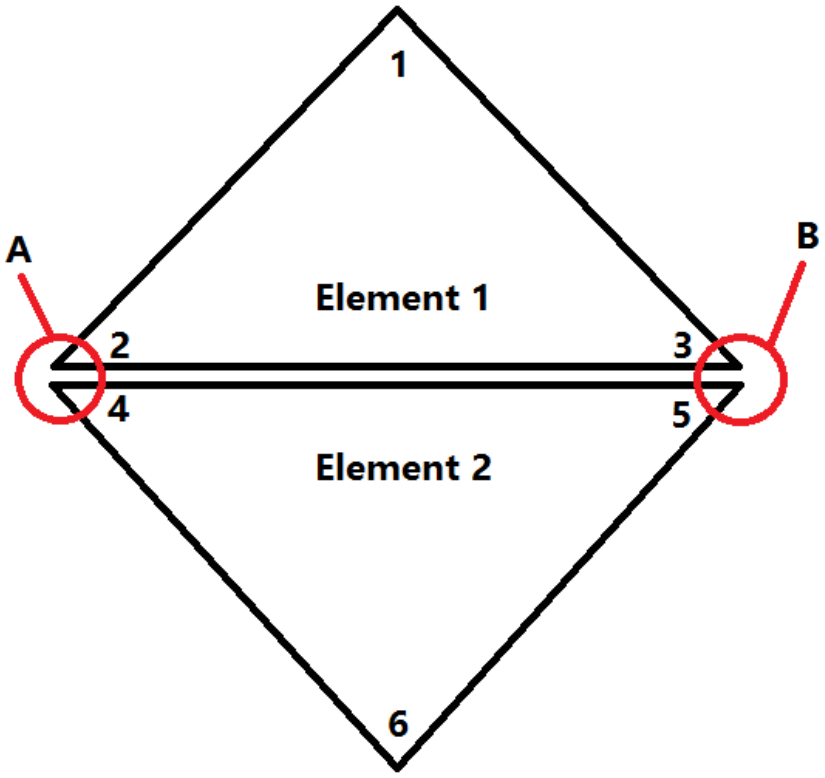

Fig. 14-Schematic of nodes and nodal groups between two neighboring elements.

We utilize Mohr–Coulomb theory and maximum tension strength criteria for the detection of the failure of springs. Once the stress state at an element contact satisfies the

rock failure criterion, either in tension mode or in shear mode, the rock failure is triggered (**Fig. 15**). A fracture can propagate along matrix elements interfaces, only, and the insides of matrix elements are treated as deformable bodies.

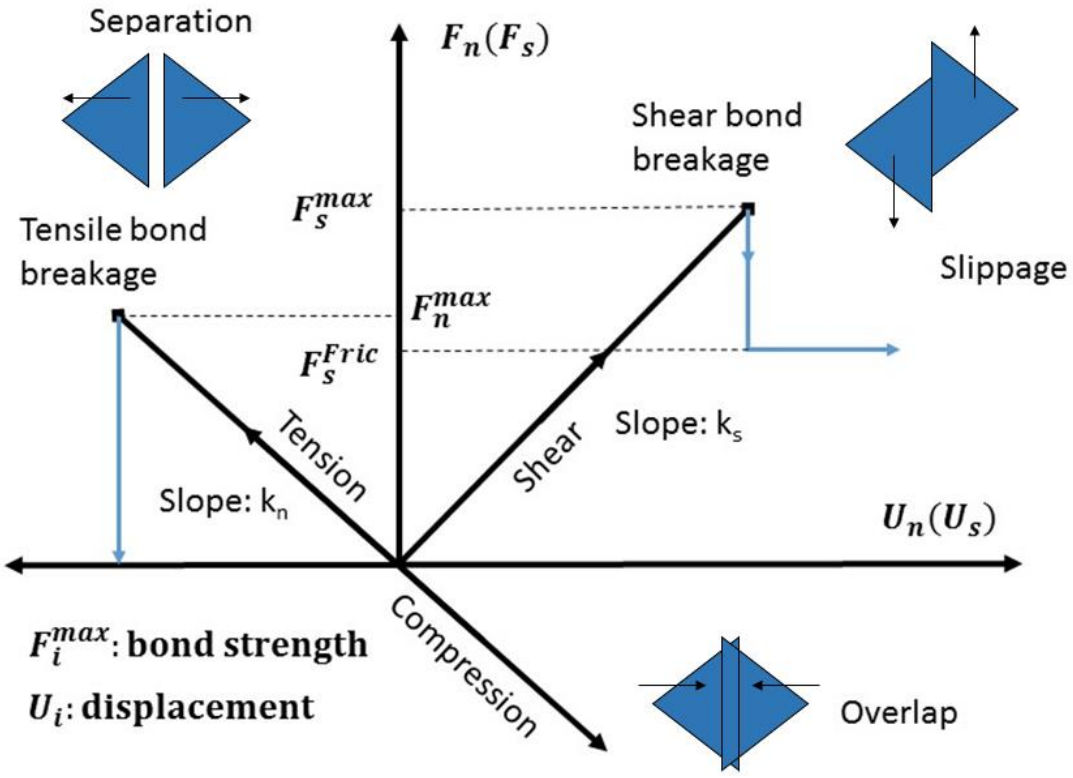

Fig. 15-Constitutive behavior in tension and shear modes.

To increase the accuracy of the model, finer matrix elements should be generated. Based on our results, when the number of matrix elements is more than 8000 and averaged matrix block size is smaller than 1.2 m, predicted fracture patterns and fluid pressure

evolution are independent from matrix block size and geometry. The model can also be used for simulating multi–fracture propagation in multi–well schemes.

2.3 Governing equations

2.3.1 Fluid flow within fractures

Some assumptions are made for this model: we assume constant temperature for the whole simulation domain, and we ignore the thermal effect of the model. We assume formation rocks are brittle materials, and linear elastic mechanics theory is applied. It is emphasized that fractures can only propagate along the interfaces of the matrix elements. To increase the simulation accuracy, the element size should be decreased.

The governing equation for fluid flow is expressed as (Batchelor 1967):

$$\frac{\partial w(s,t)}{\partial t} = \frac{1}{12\mu}\frac{\partial}{\partial s}\left[w^3(s,t)\frac{\partial p(s,t)}{\partial s}\right] \quad (2.1)$$

Here $\boldsymbol{p(s,t)}$ is the fluid pressure, $\boldsymbol{t}$ is time, $\boldsymbol{w(s,t)}$ is fracture width, $\boldsymbol{\mu}$ is viscosity, and $\boldsymbol{s}$ is the distance along the fracture. The global fluid volume balance in the domain is expressed as:

$$Q = \int_{\Omega}\frac{\partial w(s,t)}{\partial t}dS + \int_{\Omega} q_m\, dS + \int_{\Omega_{BP}} q_{lbp}\, dS + \int_{NF} q_{lnf}\, dS \quad (2.2)$$

Here $\boldsymbol{Q}$ is the injection volumetric flow rate, $\boldsymbol{q_m}$ is the leak–off rate per unit length into matrix rocks, $\boldsymbol{q_{lbp}}$ is the leak–off rate per unit length through the intact BPs and $\boldsymbol{q_{lnf}}$ is the leak–off rate per unit length through the intact NFs. We developed the BP and NF leak–off module which is based on exact solutions of an incompressible fluid displacing a compressible reservoir fluid (Dean et al. 1984). This module is well suited for studying leak–off in a shale gas reservoir.

The equations describing the leak–off mechanisms are (Dean et al. 1984):

$$q = \frac{2C_t}{\sqrt{t - \tau(s)}} \quad (2.3)$$

$$C_t = \frac{2C_1C_2}{C_1 + \sqrt{{C_1}^2 + {C_2}^2}} \quad (2.4)$$

$$C_1 = \sqrt{\frac{k\varphi\Delta P}{2\mu_f}} \quad (2.5)$$

$$C_2 = \sqrt{\frac{k\varphi C_t}{\pi\mu_r}}\Delta P \quad (2.6)$$

$$\Delta P = p_f - p_r \quad (2.7)$$

Here $\boldsymbol{\Delta P}$ is the pressure difference between the pressure inside the fracture and the reservoir pressure, $\boldsymbol{\mu_f}$ is fracturing fluid viscosity, $\boldsymbol{\mu_r}$ is the reservoir fluid viscosity and $\boldsymbol{C_t}$ is the total compressibility of the reservoir. For $q = q_m$, $\boldsymbol{k}$ is the rock matrix permeability, $\boldsymbol{\varphi}$ is reservoir porosity. For $q = q_{lbp}$, $\boldsymbol{k}$ is the intact BP permeability, $\boldsymbol{\varphi}$ is the intact BP porosity. For $q = q_{lnf}$, $\boldsymbol{k}$ is the intact NF permeability, $\boldsymbol{\varphi}$ is the intact NF porosity. $\boldsymbol{\tau(s)}$ represents the opening time of the location $\boldsymbol{s}$ along the fracture.

The initial (unbroken) fracture aperture is set as

$$w_0 = \sqrt{12k_f} \quad (2.8)$$

Here, $\boldsymbol{w_0}$ is fracture aperture, and $\boldsymbol{k_f}$ is the unbroken fracture permeability.

There are several basic assumptions involved: fractures are assumed to be completely filled with fracturing fluids, and no flow occurs at fracture tip, i.e., $q(s_{tip}, t) =$

0. The initial pressure inside the fracture network is equal to the initial pore pressure, i.e., $p(s,0) = p_{init}$.

2.3.2 Rock deformation

Since the rock mass is represented as a system of discontinuous deformable blocks, interaction force between neighboring matrix elements are represented by two virtual springs, and it is calculated by the contact constitutive law with normal stiffness $\boldsymbol{k_n}$ and shear stiffness $\boldsymbol{k_s}$, which defines the rock mechanical behavior. For the rock deformation, we consider the dynamic equations (Jaeger et al. 2007):

$$\sigma_{ij,j} + b_i - \rho u_{i,tt} - c u_{i,t} = 0 \quad (2.9)$$

$$\varepsilon_{ij} = \frac{1}{2}\left(u_{i,j} + u_{j,i}\right) \quad (2.10)$$

Here $\boldsymbol{\sigma_{ij}}$ is the Cauchy tensor, $\boldsymbol{b_i}$ is a body force, $\boldsymbol{\rho}$ is rock density, $\boldsymbol{c}$ is damping factor, $\boldsymbol{u_i}$ is the displacement, $\boldsymbol{\varepsilon_{ij}}$ is the strain

Equations of 2D motion for dynamic equations are:

$$\frac{\partial \sigma_{xx}}{\partial x} + \frac{\partial \sigma_{xy}}{\partial y} + b_x = \rho \frac{\partial^2 u_x}{\partial t^2} + c \frac{\partial u_x}{\partial t} \quad (2.11)$$

$$\frac{\partial \sigma_{xy}}{\partial x} + \frac{\partial \sigma_{yy}}{\partial y} + b_y = \rho \frac{\partial^2 u_y}{\partial t^2} + c \frac{\partial u_y}{\partial t} \quad (2.12)$$

The stress–strain relationship follows the linear elastic constitutive law:

$$\sigma_{ij} = D_{ijst} \varepsilon_{st} \quad (2.13)$$

Here, $\boldsymbol{\varepsilon_{st}}$ is the strain and $\boldsymbol{D_{ijst}}$ is the elasticity tensor which has various definitions for each mechanical case.

For typical conventional reservoirs with mechanical isotropy, the stress–strain relationship is written as (Amadei 1983):

$$\begin{pmatrix}\varepsilon_x\\ \varepsilon_y\\ \varepsilon_z\\ \varepsilon_{xy}\\ \varepsilon_{xz}\\ \varepsilon_{yz}\end{pmatrix} = \frac{1}{E}\begin{vmatrix} 1 & -v & -v & & & \\ -v & 1 & -v & & 0 & \\ -v & -v & 1 & & & \\ & & & 1+v & 0 & 0 \\ & 0 & & 0 & 1+v & 0 \\ & & & 0 & 0 & 1+v \end{vmatrix}\begin{pmatrix}\sigma_x\\ \sigma_y\\ \sigma_z\\ \sigma_{xy}\\ \sigma_{xz}\\ \sigma_{yz}\end{pmatrix} \quad \ldots\ldots\ldots\ldots\ldots\ldots\ldots\ldots (2.14)$$

Here $\boldsymbol{E}$ and $\boldsymbol{v}$ are Young's modulus and Poisson's ratio. These two parameters are the only two independent elastic constants in the elasticity tensor for mechanical isotropic cases.

Since shale formations have laminated structures in the form of stratification and bedding layers, they typically exhibit directionally isotropic rock properties. Shale rock can be often considered as a transversely isotropic material, which means that there are five independent elastic constants: $\boldsymbol{E_h, E_v, V_h, V_v, G}$ (Thiercelin et al. 1994). Therefore, for shales, the stress–strain relation becomes:

$$\begin{pmatrix}\varepsilon_x\\ \varepsilon_y\\ \varepsilon_z\\ \varepsilon_{xy}\\ \varepsilon_{xz}\\ \varepsilon_{yz}\end{pmatrix} = \begin{vmatrix} \frac{1}{E_h} & \frac{-V_h}{E_h} & \frac{-V_v}{E_v} & & & \\ \frac{-V_h}{E_h} & \frac{1}{E_h} & \frac{-V_v}{E_v} & & 0 & \\ \frac{-V_v}{E_v} & \frac{-V_v}{E_v} & \frac{1}{E_v} & & & \\ & & & \frac{2(1+V_h)}{E_h} & 0 & 0 \\ & 0 & & 0 & \frac{1}{G_v} & 0 \\ & & & 0 & 0 & \frac{1}{G_v} \end{vmatrix}\begin{pmatrix}\sigma_x\\ \sigma_y\\ \sigma_z\\ \sigma_{xy}\\ \sigma_{xz}\\ \sigma_{yz}\end{pmatrix} \quad \ldots\ldots\ldots\ldots\ldots\ldots\ldots\ldots (2.15)$$

Based on laboratory testing, Lekhnitskii (1963) mentioned that $\boldsymbol{G_v}$ can be determined by:

$$G_v = \frac{E_v E_h}{E_h(1+2v_v)+E_v} \ldots\ldots\ldots\ldots\ldots\ldots\ldots\ldots\ldots\ldots\ldots\ldots\ldots\ldots\ldots\ldots (2.16)$$

The model is also capable to handle mechanically orthotropic materials, and nine elastic constants are needed for characterization: three Young's moduli $\boldsymbol{E_x}$**,** $\boldsymbol{E_y}$ and $\boldsymbol{E_z}$, three Poisson's ratios $\boldsymbol{V_{yz}}$**,** $\boldsymbol{V_{zx}}$ and $\boldsymbol{V_{xy}}$ and the three shear moduli $\boldsymbol{G_{yz}}$**,** $\boldsymbol{G_{zx}}$ and $\boldsymbol{G_{xy}}$. The stress–strain relationship becomes:

$$\begin{pmatrix} \varepsilon_x \\ \varepsilon_y \\ \varepsilon_z \\ \varepsilon_{xy} \\ \varepsilon_{xz} \\ \varepsilon_{yz} \end{pmatrix} = \left| \begin{matrix} \frac{1}{E_x} & \frac{-V_{yx}}{E_y} & \frac{-V_{zx}}{E_z} & & & \\ \frac{-V_{xy}}{E_x} & \frac{1}{E_y} & \frac{-V_{zy}}{E_z} & & 0 & \\ \frac{-V_{xz}}{E_x} & \frac{-V_{yz}}{E_y} & \frac{1}{E_z} & & & \\ & & & \frac{1}{2G_{yz}} & 0 & 0 \\ & 0 & & 0 & \frac{1}{2G_{zx}} & 0 \\ & & & 0 & 0 & \frac{1}{2G_{xy}} \end{matrix} \right| \begin{pmatrix} \sigma_x \\ \sigma_y \\ \sigma_z \\ \sigma_{xy} \\ \sigma_{xz} \\ \sigma_{yz} \end{pmatrix} \ldots\ldots\ldots\ldots\ldots\ldots\ldots\ldots (2.17)$$

where $\frac{V_{yz}}{E_y}=\frac{V_{zy}}{E_z}$, $\frac{V_{xz}}{E_x}=\frac{V_{zx}}{E_z}$, and $\frac{V_{xy}}{E_x}=\frac{V_{yx}}{E_y}$ (Amadei 1983).

2.2.3 Mechanical interaction between neighboring matrix elements

For DEM with deformable blocks, mechanical interaction between two neighboring matrix elements is represented by two virtual springs. Neighboring elements are initially bonded together at their contact points by two springs, and springs become failure once the failure criteria (maximum tensile stress criterion and/or Coulomb criterion) are satisfied. Some assumptions have been made for this model:

1. Rock matrix elements are considered as deformable blocks.

2. Mechanical interaction between two neighboring matrix elements is represented by superposition of forces from two virtual springs.
3. Interaction forces between two neighboring matrix elements are represented by normal force and shear force, which are proportional to normal displacement and shear displacement respectively.

The mechanical interaction between two neighboring matrix elements is calculated by the contact constitutive law with normal stiffness $\boldsymbol{k_n}$ and shear stiffness $\boldsymbol{k_s}$, which defines the rock mechanical behavior. The concept of stiffness of a spring is originated from Hooke's law. For a massless spring, the relationship between applied force $\boldsymbol{F}$ and deformation $\Delta\boldsymbol{X}$ has the form:

$$F = -k\Delta X \quad (2.18)$$

Here $\boldsymbol{k}$ is the stiffness characterizing the rigidity of a spring. For the vibration of single degree of freedom systems, the motion of the spring–mass system is described by a second–order homogeneous linear ordinary differential equation:

$$m\ddot{x} = -kx + F(t) \quad (2.19)$$

Here $\boldsymbol{m}$ is the mass, $\ddot{\boldsymbol{x}}$ is the second derivative of displacement with respect to time $\boldsymbol{t}$. $\boldsymbol{F(t)}$ is the force applied on the mass. The schematic plot of the vibration of single degree of freedom systems can be seen in the **Fig. 16** in below. When $F(t) = 0$, the vibration of system is called free vibration system.

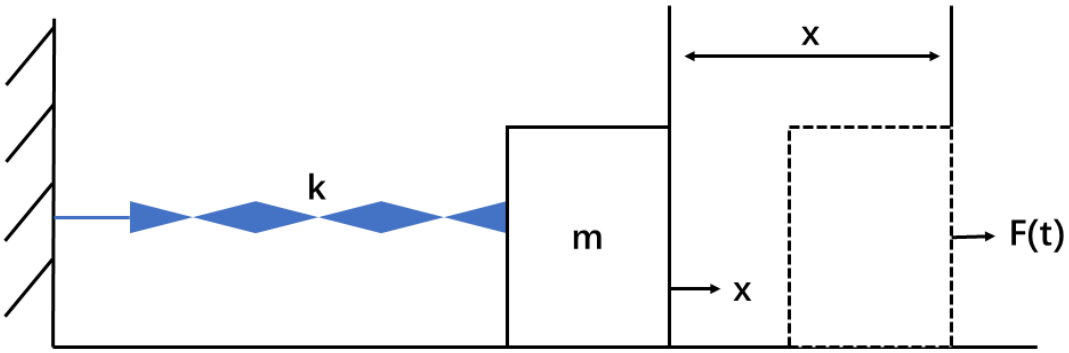

Fig. 16-Schematic of the vibration of spring–mass system with single degree of freedom.

For damped vibration of single degree of freedom systems, the spring–mass system with an energy loss represented by the damping force is shown in **Fig. 17**. Based on Newton's second law, the governing equation for this model is a linear differential equation:

$$m\ddot{x} + c\dot{x} + kx = F(t) \quad (2.20)$$

Here $\boldsymbol{c}$ is the damping coefficient. For damped vibration of multiple degree of freedom system, it has the same basic form of the governing equation as Equation 2.20, and the difference is that it is a matrix equation:

$$[M^e]\{\ddot{x}\} + [C^e]\{\dot{x}\} + [K^e]\{x\} = \{F(t)\} \quad (2.21)$$

Here $[\boldsymbol{M^e}]$ is a mass matrix, $[\boldsymbol{C^e}]$ is a damping matrix and $[\boldsymbol{K^e}]$ is stiffness matrix. $\{\boldsymbol{F(t)}\}$ is the loading vector.

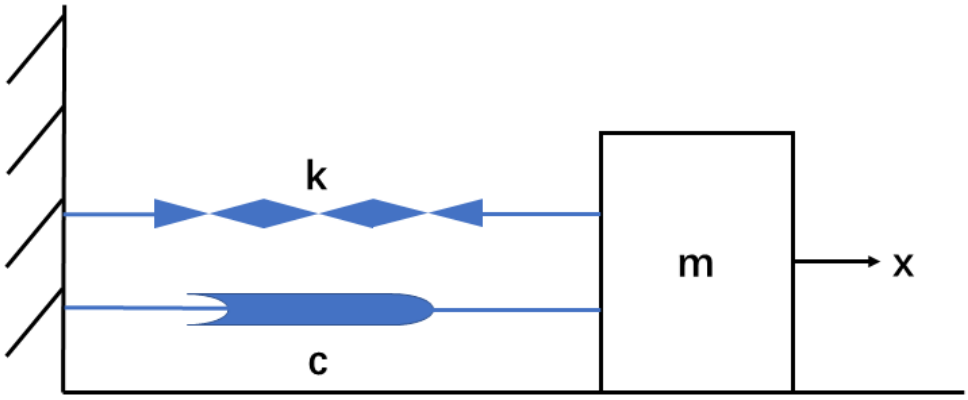

Fig. 17-Schematic of the damped vibration of spring–mass system with single degree of freedom.

In the *n–th* time step, we calculate the total force $\boldsymbol{F_c^{(n)}}$ and relative displacement $\boldsymbol{u^{(n)}}$ of the neighboring matrix elements using the displacements in normal and shear modes for fracture interfaces. Denoting the normal unit vector by $\overrightarrow{\boldsymbol{n_J}}$ and the tangential unit vector by $\overrightarrow{\boldsymbol{t_J}}$, the relationships take the form

$$F_c^{(n)} = F_n^{(n)}\overrightarrow{n_J} + F_s^{(n)}\overrightarrow{t_J} \quad (2.22)$$

$$u^{(n)} = u_n^{(n)}\overrightarrow{n_J} + u_s^{(n)}\overrightarrow{t_J} \quad (2.23)$$

Here $\boldsymbol{F_n^{(n)}}$ is the normal force acting perpendicularly on the matrix element interface and $\boldsymbol{F_s^{(n)}}$ is the shear force acting parallel to the matrix interface plane at the *n–th* time step.

For different spring–mass systems, different models for calculating spring stiffness are chosen based on elastic constants and the geometry of a spring. Based on beam theory, values of $\boldsymbol{k_n}$ and $\boldsymbol{k_s}$ are expressed by $\boldsymbol{E}$ and $\boldsymbol{G}$. The corresponding equations are:

$$k_n = \frac{EA}{L} \quad (2.24)$$

$$k_s = \frac{GA}{L} \quad (2.25)$$

where $\boldsymbol{A}$ is the contact area, and $\boldsymbol{L}$ is the characteristic length of a contact plane, given by $L = \sqrt{A}$. When the block size of the structure which is represented by a spring is extremely small, values of $\boldsymbol{k_n}$ and $\boldsymbol{k_s}$ are expressed by:

$$k_n = \frac{EA}{2B_0} \quad (2.26)$$

$$k_s = \frac{GA}{2B_0} \quad (2.27)$$

Here $\boldsymbol{B_0}$ is "pseudo" block size, typically is assumed to be 1% of the block element size.

For a matrix element interface, the thresholds of the normal force and the shear force are calculated as:

$$F_n^{max} = AT_0 \quad (2.28)$$

$$F_s^{max} = AS_0 + tan\vartheta F_n^{(n)} \quad (2.29)$$

Here $\boldsymbol{S_0}$ is the cohesion, $\boldsymbol{T_0}$ is the tensile strength, and $\boldsymbol{\vartheta}$ is the internal friction angle. If both $\boldsymbol{F_n^{(n)}}$ and $\boldsymbol{F_s^{(n)}}$ are smaller than the threshold, no rock failure will occur, and the normal force and the shear force are updated according to:

$$F_n^{(n)} = F_n^{(n-1)} - k_n \Delta u_n^{(n)} \quad (2.30)$$

$$F_s^{(n)} = F_s^{(n-1)} - k_s \Delta u_s^{(n)} \quad (2.31)$$

If $|F_s^{(n)}| > F_s^{max}$, rock failure occurs by the shear mode and the $\boldsymbol{F_n^{(n)}}$ and $\boldsymbol{F_s^{(n)}}$ are updated as:

$$F_n^{(n)} = F_n^{(n-1)} - k_n \Delta u_n^{(n)} \quad (2.32)$$

$$F_s^{(n)} = tan\vartheta F_n^{(n)} \quad (2.33)$$

Tensile failure will be triggered if $|F_n^{(n)}| > F_n^{max}$. Then $\boldsymbol{F_n^{(n)}}$ and $\boldsymbol{F_s^{(n)}}$ will be updated as:

$$F_n^{(n)} = 0 \quad (2.34)$$

$$F_s^{(n)} = 0 \quad (2.35)$$

2.4 Weak form formulation

2.4.1 Fluid flow within fractures

In continuous fluid flow network, the fluid net pressure can be approximated by utilizing the Galerkin finite element method:

$$p(s) = \sum_{j=1}^{N} p_j^e \, \varphi_j^e(s) \quad (2.36)$$

Here $\boldsymbol{\varphi_j^e(s)}$ is the approximation function at node $\boldsymbol{j}$, $\boldsymbol{p_j^e}$ is the unknown value of net pressure at node $\boldsymbol{j}$.

For Galerkin method, weight function $\boldsymbol{w_i}$ is equal to $\boldsymbol{\varphi_i}$. The weak form of the fluid flow governing equation is developed by multiply the equation with a weight function $\boldsymbol{w_i(s)}$, and integrate it over the whole domain $\boldsymbol{\Omega}$:

$$\int_\Omega \frac{\Delta w}{\Delta t} w_i(s)\, ds = \frac{1}{12\mu} w_i(s) \int_\Omega \frac{\partial}{\partial s} w^3 \frac{\partial p(s)}{\partial s} ds \quad (2.37)$$

We introduce the leak off mechanisms into the equation, and integrate the term on the right ride of the expression:

$$\int_{\Omega} \frac{\Delta w}{\Delta t} w_i(s)\, ds + \int_{L} q_{LT}(s,t) w_i(s)\, ds$$

$$= -\frac{1}{12\mu} \int_{\Omega} w^3 \frac{\partial w_i(s)}{\partial s} \frac{\partial p(s)}{\partial s} ds + w_i(0)\, Q_1 + w_i(s) Q_2 \ldots\ldots\ldots\ldots (2.38)$$

Here $\boldsymbol{q_{LT}(s,t)}$ is the total fluid leak–off rate at time $\boldsymbol{t}$, and $\boldsymbol{Q}$ are the secondary variables specified on the boundaries, which represent fluid injection rate specified at the wellbore ($\boldsymbol{Q_1}$) and flux rate specified at fracture tip ($\boldsymbol{Q_2}$):

$$Q_1 = \left[\frac{1}{12\mu} w^3 \frac{\partial p(s)}{\partial s}\right]_{s=0} = q_{inj} \ldots\ldots\ldots\ldots\ldots\ldots\ldots\ldots\ldots\ldots\ldots\ldots\ldots\ldots\ldots\ldots\ldots\ldots (2.39)$$

$$Q_2 = \left[\frac{1}{12\mu} w^3 \frac{\partial p(s)}{\partial s}\right]_{s=0} = 0 \ldots\ldots\ldots\ldots\ldots\ldots\ldots\ldots\ldots\ldots\ldots\ldots\ldots\ldots\ldots\ldots\ldots\ldots\ldots\ldots (2.40)$$

Here $\boldsymbol{q_{inj}}$ is the fluid injection rate specified at the wellbore. Specification of $\boldsymbol{Q_1}$ and $\boldsymbol{Q_2}$ on the boundary gives the natural boundary condition of the weak form expression. Since we assume that the fluid lag at the near fracture tip region is negligible, the net pressure at fracture tip is 0, which implies that $Q_2 = 0$ at the fracture tip. Finite element model can be developed based on the weak form of the expression, and the *ith* algebraic equation of the system of n equations is:

$$\sum_{j=1}^{N} K_{ij}^e p_j^e = f_i^e + Q_i^e \ (i = 1,2 \ldots\ldots, n) \ldots\ldots\ldots\ldots\ldots\ldots\ldots\ldots\ldots\ldots\ldots\ldots\ldots\ldots\ldots\ldots (2.41)$$

Where

$$K_{ij}^e = \frac{1}{12\mu} \int_{s_a}^{S_b} w^3 \frac{\partial \varphi_i^e(s)}{\partial s} \frac{\partial \varphi_j^e(s)}{\partial s} ds \ldots\ldots\ldots\ldots\ldots\ldots\ldots\ldots\ldots\ldots\ldots\ldots\ldots\ldots\ldots\ldots\ldots (2.42)$$

$$f_i^e = \int_{S_a}^{S_b} \frac{\Delta w}{\Delta t} \varphi_i^e(s) ds + \int_{S_a}^{S_b} q_{LT}(s,t) \varphi_i^e(s)\, ds \ldots\ldots\ldots\ldots\ldots\ldots\ldots\ldots\ldots\ldots\ldots\ldots\ldots\ldots\ldots (2.43)$$

The matrix notation of the linear equations is:

$$[K^e]\{P^e\} = \{f^e\} + \{Q^e\} \quad (2.44)$$

For a finite element mesh with linear Lagrange elements, the coefficient matrix $[\boldsymbol{K^e}]$ and column vector $\{\boldsymbol{f^e}\}$ are:

$$[K^e] = \frac{w^3}{12\mu h_e}\begin{bmatrix} 1 & -1 \\ -1 & 1 \end{bmatrix} \quad (2.45)$$

$$\{f^e\} = \frac{(\frac{\Delta w}{\Delta t} + q_{LT}(s,t))h_e}{2}\begin{Bmatrix} 1 \\ 1 \end{Bmatrix} \quad (2.46)$$

For a finite element mesh with quadratic Lagrange elements, the coefficient matrix $[\boldsymbol{K^e}]$ and column vector $\{\boldsymbol{f^e}\}$ are:

$$[K^e] = \frac{w^3}{36\mu h_e}\begin{bmatrix} 7 & -8 & 1 \\ -8 & 16 & -8 \\ 1 & -8 & 7 \end{bmatrix} \quad (2.47)$$

$$\{f^e\} = \frac{(\frac{\Delta w}{\Delta t} + q_{LT}(s,t))h_e}{6}\begin{Bmatrix} 1 \\ 4 \\ 1 \end{Bmatrix} \quad (2.48)$$

Here $\boldsymbol{h_e}$ is the element size.

2.4.2 Rock deformation

The matrix form of shape functions for 2D linear triangular elements is:

$$[N] = \begin{bmatrix} N_i & 0 & N_j & 0 & N_m & 0 \\ 0 & N_i & 0 & N_j & 0 & N_m \end{bmatrix} \quad (2.49)$$

Here, $\boldsymbol{N_i}$, $\boldsymbol{N_j}$ and $\boldsymbol{N_m}$ are shape functions of three nodes in the same element. They have the form:

$$N_i = \frac{1}{2A}(a_i + b_i x + c_i y) \quad (i,j,m) \quad (2.50)$$

Here $\boldsymbol{a_i}$, $\boldsymbol{b_i}$, and $\boldsymbol{c_i}$ are constants and they can be determined only by x and y coordinates of the node, and $\boldsymbol{A}$ is the area of the triangular element. Once the displacements of an element are determined, strain of the element can be calculated by:

$$\{\varepsilon^e\} = [B]\{u^e\} \quad (2.51)$$

Vector form of displacements $\{\boldsymbol{u^e}\}$ and vector form of strains $\{\boldsymbol{\varepsilon^e}\}$ are:

$$\{u^e\} = \begin{Bmatrix} u_1 \\ v_1 \\ u_2 \\ v_2 \\ u_3 \\ v_3 \end{Bmatrix} \quad (2.52)$$

$$\{\varepsilon^e\} = \begin{Bmatrix} \varepsilon_x \\ \varepsilon_y \\ \tau_{xy} \end{Bmatrix} \quad (2.53)$$

Here $\boldsymbol{u_i}$ and $\boldsymbol{v_i}$ are displacements in x direction and y direction for node $\boldsymbol{i}$ respectively. Strain matrix $[\boldsymbol{B}]$ has the form:

$$[B] = \frac{1}{2A}\begin{bmatrix} \frac{\partial N_i}{\partial x} & 0 & \frac{\partial N_j}{\partial x} & 0 & \frac{\partial N_k}{\partial x} & 0 \\ 0 & \frac{\partial N_i}{\partial y} & 0 & \frac{\partial N_j}{\partial y} & 0 & \frac{\partial N_k}{\partial y} \\ \frac{\partial N_i}{\partial y} & \frac{\partial N_i}{\partial x} & \frac{\partial N_j}{\partial y} & \frac{\partial N_j}{\partial x} & \frac{\partial N_k}{\partial y} & \frac{\partial N_k}{\partial x} \end{bmatrix} \quad (2.54)$$

Since $[\boldsymbol{B}]$ is a constant matrix, all three nodes in an element have the same calculated strain vector. Typically, we call a three–node triangular element as a constant strain element.

The stiffness matrix has the form:

$$[K^e] = \int_{\Omega^e} [B]^T [D][B] dxdy \quad (2.55)$$

Here, $[\boldsymbol{D}]$ is elastic matrix which has different forms for different materials, as shown in equations 2.15–2.17. Since we utilize linear triangular elements which have three nodes and two directions, $[\boldsymbol{K^e}]$ is a 6×6 matrix.

For the rock deformation, we consider the dynamic equations (Jaeger et al. 2007):

$$\sigma_{ij,j} + b_i - \rho u_{i,tt} - c u_{i,t} = 0 \quad (2.56)$$

The matrix form of the expression is:

$$[M^e]\{\ddot{u}(t)\} + [C^e]\{\dot{u}(t)\} + [K^e]\{u(t)\} = \{Q(t)\} \quad (2.57)$$

Here, the mass matrix $[M^e]$ and damping matrix $[C^e]$ have the form:

$$[M^e] = \int_{\Omega^e} \rho [N]^T [N] dxdy \quad (2.58)$$

$$[C^e] = \int_{\Omega^e} c_0 [N]^T [N] dxdy \quad (2.59)$$

Here, $\boldsymbol{\rho}$ is the density of an element, $\boldsymbol{c_0}$ is the damping coefficient, and $\{\boldsymbol{Q(t)}\}$ is the loading vector.

The dynamic equation is solved by dynamic relaxation method. The dynamic relaxation method is an explicit numerical technique for solving a static problem by transforming it into a dynamic problem. It is a computationally efficient technique that avoids solving large scale matrix equations. Several steps are involved for solving rock deformation based on dynamic relaxation method:

1. Set the initial velocity and displacement of each node.
2. Calculated internal force of each node, which is expressed as:

$$\{F_{int}\} = [C^e]\{\dot{u}\} + [K^e]\{u\} \quad (2.60)$$

3. Calculated external force $\{\boldsymbol{F_{ext}}\}$ for each node based on boundary conditions and strength criteria.
4. Calculate acceleration of each node based on the expression:

$$\{a\} = [M]^{-1}(\{F_{ext}\} - \{F_{int}\}) \quad (2.61)$$

5. Based on the calculated $\{\boldsymbol{a}\}$ and time step $\boldsymbol{\Delta t}$, update the velocity and displacement of each node.
6. Repeat step 2–5, until the system total kinetic energy becomes 0.

2.5 Coupling mechanisms

The coupled fluid flow and rock deformation system is one of the key feature in a complex hydraulic fracture propagation model. For simulations which are developed for unconventional reservoirs, several basic physical processes should be incorporated into models:

1. Fluid flow within fracture networks;
2. Fracture propagation criteria;
3. Rock deformation; and
4. Mechanical interaction and stress shadow effect during complex fracture propagation.

For hydraulic fracture propagation in reservoirs with comparatively high matrix permeability, the feature controlling fluid leak–off should also be incorporated into the simulation. In this 2D model, the simulation domain is discretized to 2D matrix elements and 1D fluid flow (potential fracture) elements. The matrix blocks are treated as homogeneous media. Fractures can only propagate along the matrix interfaces.

An iterative algorithm is used to solve the coupled fluid flow and rock deformation model. Standard Galerkin FEM was utilized to discretize the fluid flow equation (details are shown in the previous section). The discretized flow equation was nonlinear due to the direct correlation between pressure and fracture width. Therefore, The Picard iteration scheme was utilized to solve the non–linear coupling system (Adachi et al. 2007). At *n–th* time step, the $\boldsymbol{p_m^{(n+1)}}$ is solved by a fixed–point scheme using the given trial solution $(\boldsymbol{p_m^{(n)}}, \boldsymbol{w_m^{(n)}})$, and the $\boldsymbol{w_m^{(n+1)}}$ is calculated from $\boldsymbol{p_m^{(n+1)}}$ through the rock deformation solver. The solution of $\boldsymbol{p_m^{(n+1)}}$ and $\boldsymbol{w_m^{(n+1)}}$ are updated at each iteration step by the following equation:

$$p_m^{(n+1)} = (1-\varepsilon)p_m^{(n)} + \varepsilon p_m^{(n+1)} \quad (2.62)$$

$$w_m^{(n+1)} = (1-\varepsilon)w_m^{(n)} + \varepsilon w_m^{(n+1)} \quad (2.63)$$

The value of $\boldsymbol{\varepsilon}$ ranges from 0 to 0.5 for convergence purpose. When fracture is initiated, the initial fracture width is calculated via the correlation in below:

$$w_{ini} = \sqrt{12k} \quad (2.64)$$

Here, $\boldsymbol{w_{ini}}$ is the initial fracture width of the new fracture element, $\boldsymbol{k}$ is the permeability which has different value due to the material properties (NF, BP or matrix). **Fig. 18** illustrates the work flow of the simulation.

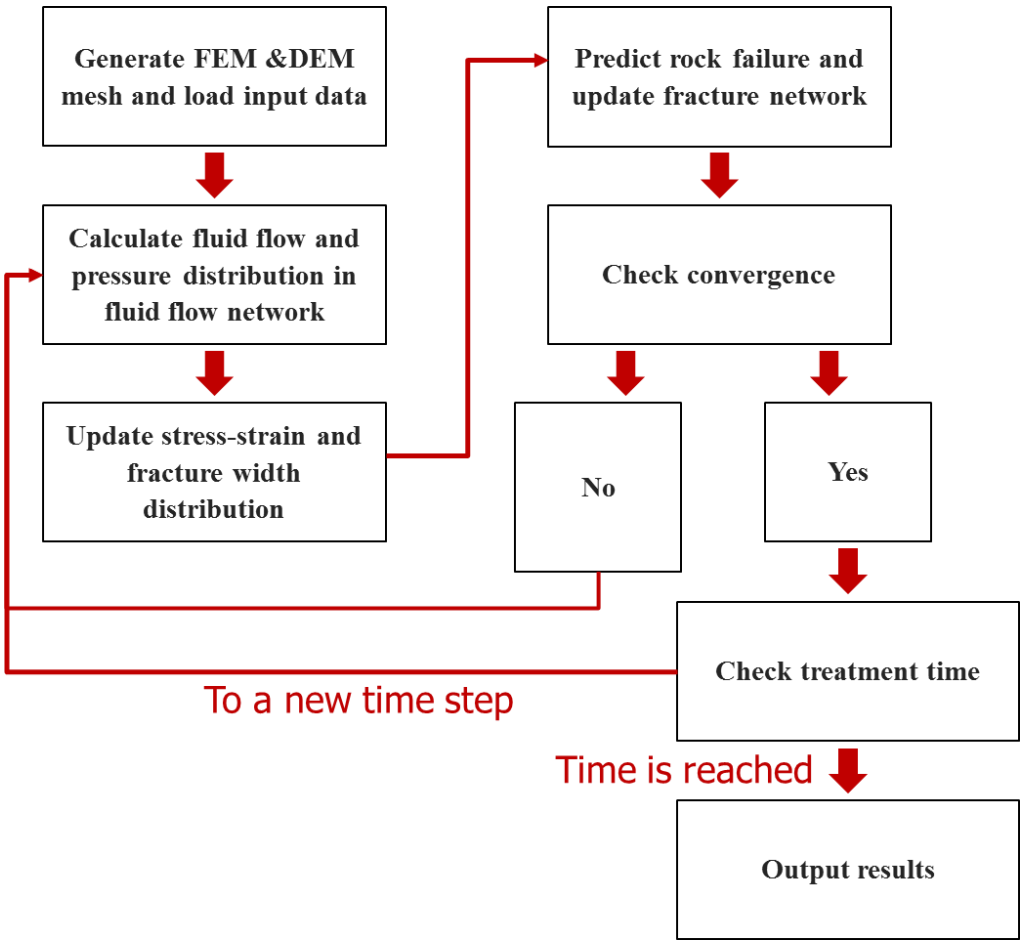

Fig. 18-Flowchart of the FDEM numerical simulation.

2.6 Conclusions

A novel two–dimensional (2D) FDEM model was developed to describe complex fracture propagation in unconventional formations. Key physical processes for modeling complex hydraulic fracture propagation in unconventional reservoirs, including HF–NF interaction, stress shadow effects, HF–BP interaction, fluid flow in fracture network, mechanical interaction between neighboring elements and mechanical anisotropy of

formations etc., were successfully incorporated into the model. This coupled fluid flow and geomechanics model can be applied for multi–fracture, multi–well scenarios.

3. MODEL VALIDATION

3.1 Introduction

Model validation is highly necessary for simulation development. In recent years, microseismic event interpretation techniques have been used to characterize the opening fracture properties. However, there are still many challenges for accurately characterizing hydraulic fracture geometry through microseismic monitoring and interpretation (Eisner et al. 2011). Pressure fall–off diagnostic testing is also widely used in the petroleum industry to evaluate hydraulic fracture treatments and fracture characterization. However, quantitatively characterization of fracture properties is still problematic.

Following the tradition in the field of hydraulic fracturing propagation simulator development, we used a classical lumped 2D model to validate the simulation model. In this case we used the PKN model as the basis for comparison. Indeed, for the overwhelming part of the process, the x_f is much larger than the h_f.

In the second part of model validation, we reproduced several published experimental results related to a bi–wing HF intersecting two NFs.

3.2 Comparison with analytical solutions

Table 2 shows the input parameters for model validation. Since we developed a 2D model, fracture height was set to be a constant value. The description of the PKN analytical model is in the Section 1.

Input parameter	Value	Unit
Matrix		
E	2×10^{10}	Pa
ν	0.2	–
h_f	6	m
μ	0.3	Pa.s
q_i	0.1	m^3/s
σ_h	40.9×10^6	Pa
Natural fractures		
k_{nf}	50	μD
T_{nf}	1.24	MPa
S_{nf}	3.75	MPa
ϑ_{nf}	Degree	25

Table 2-Input parameters for model validation.

The analytical solutions of PKN model with constant injection rate and no leak–off are given in below (Valko and Economides 1995):

$$x_f = 0.524\left(\frac{i^3E'}{\mu h_f^4}\right)^{0.2} t^{0.8} \quad \ldots\ldots(3.1)$$

$$w_{w,0} = 3.04\left(\frac{i^2\mu}{E'h_f}\right)^{0.2} t^{0.2} \quad \ldots\ldots(3.2)$$

$$P_{n,w} = \sigma_h + 1.52\left(\frac{E'^4 \mu i^2}{h_f^6}\right)^{0.2} t^{0.2} \dots\dots\dots\dots\dots\dots\dots\dots\dots\dots\dots\dots\dots\dots\dots\dots\dots\dots\dots\dots\dots \quad (3.3)$$

where $\boldsymbol{i}$ is injection rate into one fracture wing and $E' = E/(1-\nu)^2$ based on the plane strain theory.

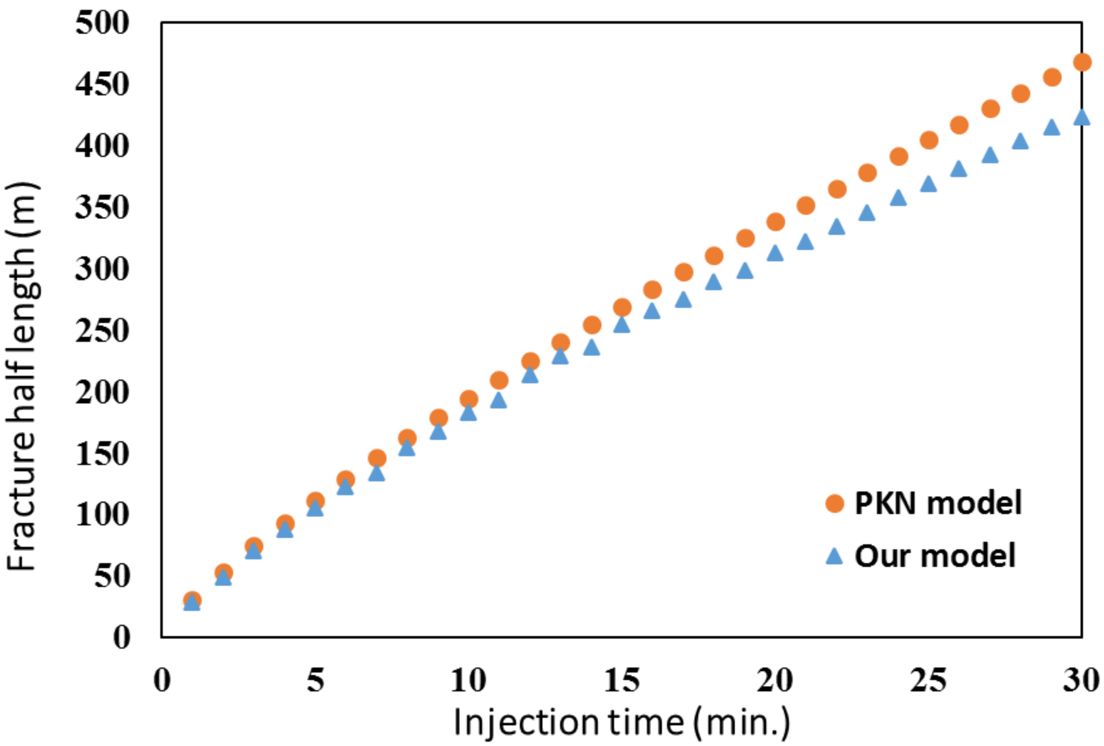

Fig. 19-Comparison of the evolution of fracture half–length between the PKN and numerical models.

The comparison results of fracture half length (**Fig. 19**), maximum fracture width at the wellbore (**Fig. 20**) and net injection pressure (**Fig. 21**) are shown in below. Since our

model is based on finite–discrete element method, injection pressure fluctuations occur when rock failure is triggered. Our results (**Figs 19** through **21**) are in fair agreement with the PKN model, showing similar evolution trend. Small deviation is anticipated, because the classical PKN model does not include rock failure criterion and hence our model should calculate less fracture length and more width/pressure under similar conditions.

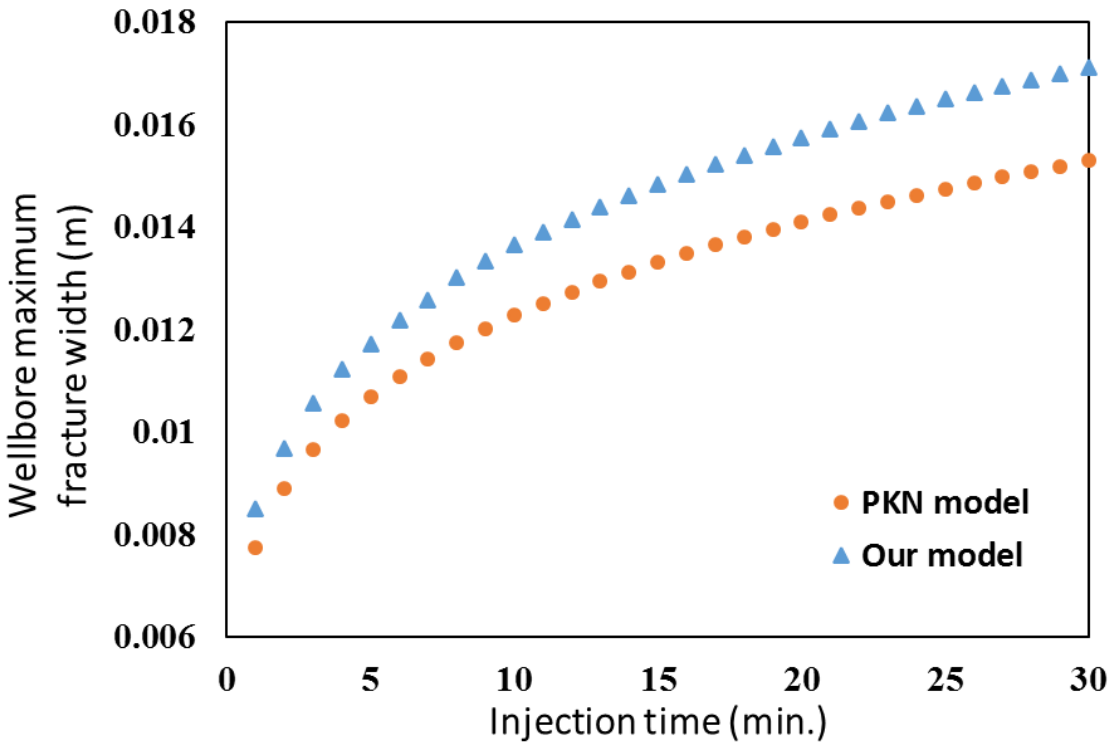

Fig. 20-Comparison of the evolution of wellbore maximum fracture width between the PKN and numerical models.

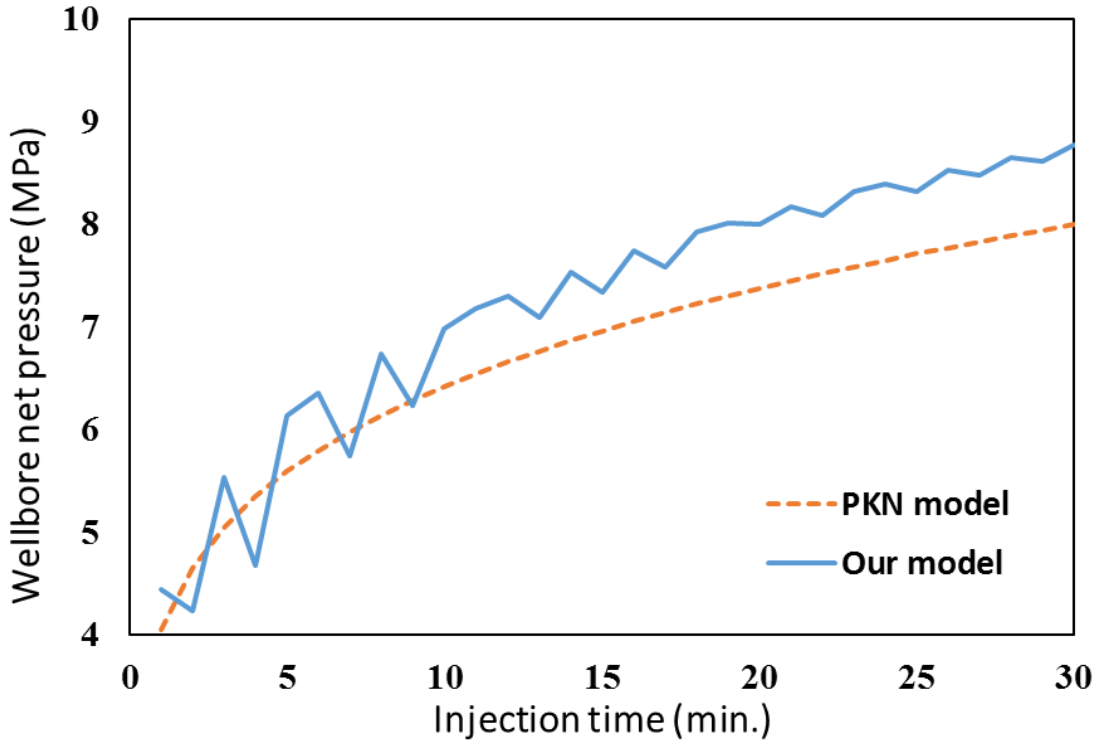

Fig. 21-Comparison of the evolution of wellbore net pressure between the PKN and numerical models.

3.3 Comparison with laboratory tests of HF−NF Interaction

Several researchers have conducted experiments investigating whether a fracture will propagate across a frictional interface under various scenarios (various horizontal stress differences and HF–NF intersection angles (e.g., Blanton 1986; Warpinski et al. 1987; Gu et al. 2011). For validation purposes, we conducted several simulations for studying HF–NF interaction behavior and compared the results with published experimental data (**Fig. 22)**. The input parameters of our numerical simulation are set as similar as possible to those used in the experiments. **Fig. 22** demonstrates that the HF tends

to cross the NFs under relatively high horizontal stress difference and large intersection angle (right top side of the red separating line), and tends to open NFs under relatively low horizontal stress difference and small intersection angle (left down side of the red separating line). Our simulation results show good agreement with the experimental data. We conclude that our model can reliably predict the nature of the HF–NF interaction mode.

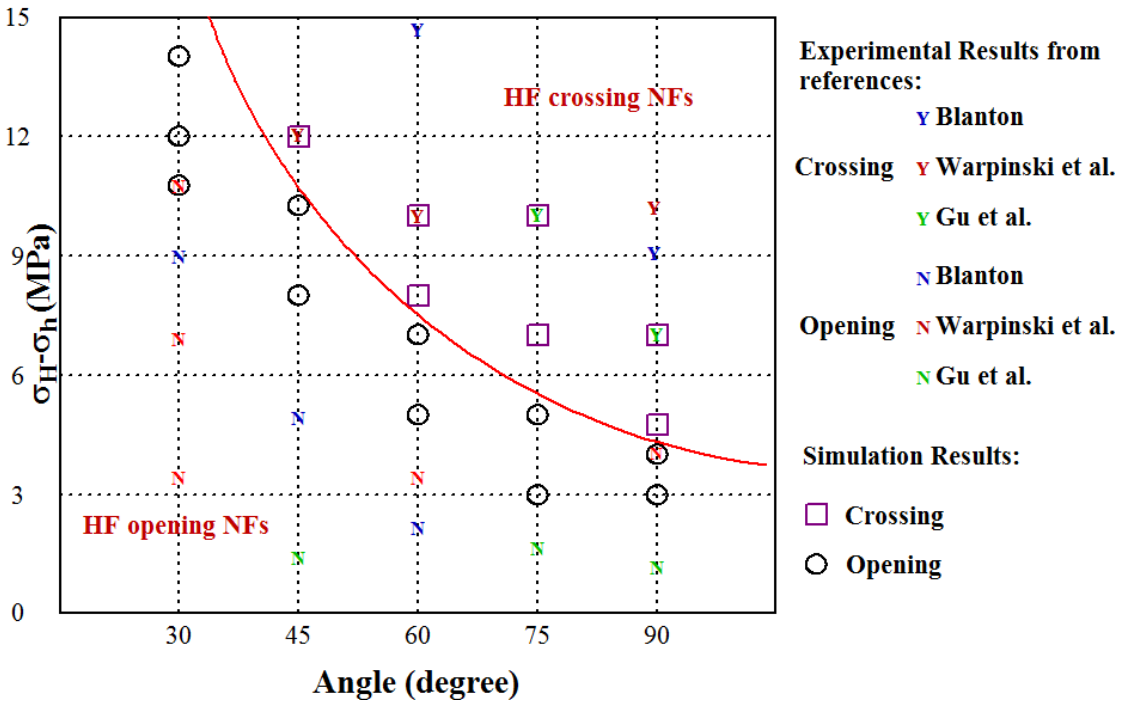

Fig. 22-Comparisons of HF–NF interaction mode between the numerical model and experimental results from literature.

4. PROPAGATION OF NON–PLANAR MULTIPLE FRACTURES IN HOMOGENEOUS RESERVOIRS

4.1 Introduction

For modern multi–stage hydraulic fracturing operations, stress shadow effects and hydraulic fracturing operation parameters strongly affect fracture geometries, and further determine hydrocarbon production. Formations can be compressed by net pressure within hydraulic fractures, and the local minimum stress direction can be altered due to the stress shadowing effect. Daneshy (2014) defined the stress shadowing effect as the influence of residual stresses created by existed fractures on the stress orientation and magnitude of in–situ stresses, which highly affect the creation of new fractures. For the case with propagation of multiple fractures, since the induced stress has different magnitude in different directions, the direction of minimum horizontal stress and maximum horizontal stress may change as the fracture propagates. Furthermore, a non–planar fracture can result in different stress shadowing effects compared with a planar fracture, and this can cause the induced stress distribution to become complex. Recently, field observation indicated that generally more than 25% of the induced fractures have negligible contribution on hydrocarbon production (Wong et al. 2013). This indicates that understanding of mechanical interaction between fractures and well–designed hydraulic fracturing operation are key factors in unconventional reservoir development.

To investigate the fracture pattern evolution and induced stress distribution for the case with multi–fracture propagation, a well–developed coupled fluid flow and rock

deformation hydraulic fracture propagation model is required. Dohmen et al. (2014) found that stress shadow effect results in the increase of minimum horizontal stress in the fracturing zone. Nagel et al. (2011) investigated the effect of multiple hydraulic fractures on stress shadowing based on a continuum model and UDEC DEM simulations. They found that different hydraulic fracturing timing (simultaneous versus sequential) strongly influences local induced stress and change fracture complexity. Singh and Miskimins (2010) conducted a numerical study to investigate the effect of stress shadowing on fracture initiation and stimulation of horizontal wells. They concluded that fracture spacing strongly affects stress interference.

4.2 Simulation setup

Table 3 summarizes the input parameters for simulations of propagation of multiple fractures. The values of parameters were determined from the characterization of shale samples from Barnett formations (Zhi and Ahmad 2016; Roussel and Sharma 2010). Simulation results which are shown in this section were obtained based on these input parameters, possibly changing only one of treatment parameters at a time. The size of the 2D domain is 100 m by 80 m, and the horizontal well starts from (0,40) m and ends at (100,40) m (**Fig. 23**). There are three perforation cluster in the simulation domain. The middle perforation cluster is located at the center of the simulation domain. We assumed that one cluster can initiate only one fracture.

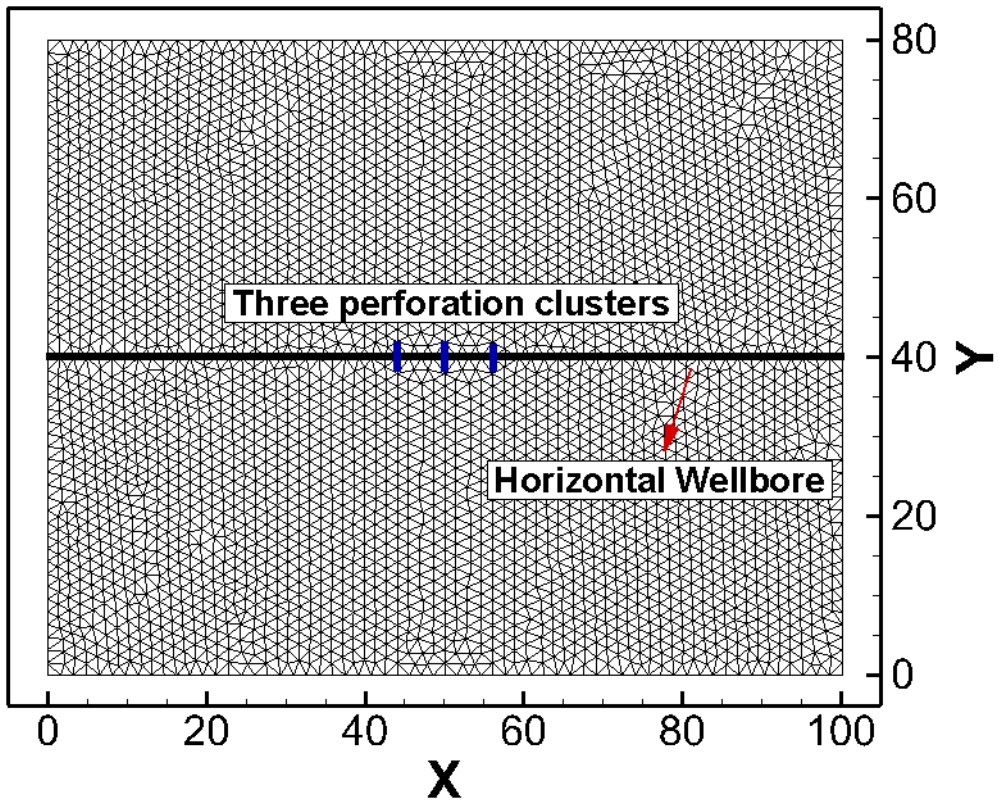

Fig. 23-Schematic of 2D simulation domain with three perforation clusters.

Formation Properties	**Value**
σ_v	48.26 MPa
σ_h	43.44 MPa
σ_H	44.13 MPa
Poisson's ratio	0.2
Young's modulus	50.33 GPa
Cohesion	0.273 MPa
Permeability	10^{-6} μm^2
Friction angle	20.44 degree
Treatment parameters	**Value**
Injection rate	0.24 m^3/s
Fluid viscosity	0.003 Pa•s
Perforation cluster spacing	6 m
Number of perforation cluster	3

Table 3-Input parameters for simulations of propagation of multiple fractures.

4.3 Sensitivity studies for simultaneous propagation of multiple fractures

The first numerical case concerns the effect of perforation cluster spacing on multiple fractures propagation. Only the cluster spacing was changed, and all other parameters were unchanged. With the decrease of cluster spacing, a non–planar fracture pattern is formed due to the strong stress shadowing effect among fractures **(Fig. 24)**.

Moreover, with increased spacing, the length of the middle fracture is increased, since the magnitude of stress shadowing induced by two exterior fractures in the direction of minimum horizontal stress becomes much smaller when the spacing is large. When the stress shadowing effect is strong, the local minimum stress direction is changed, which may result in non–planer fracture propagation, and the two exterior fractures have the most freedom to propagate curving outward (Olson 2008).

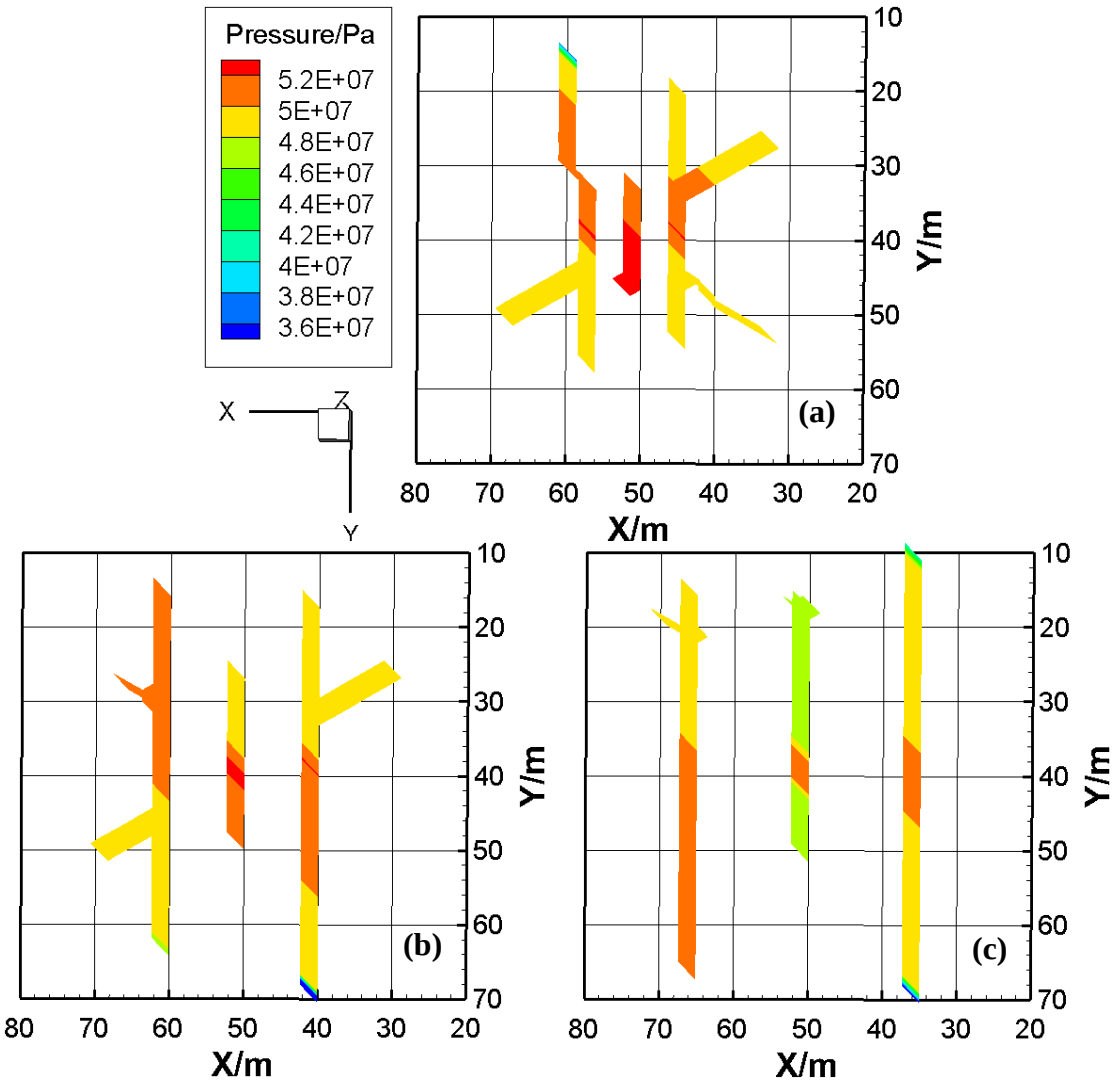

Fig. 24-Multiple fractures propagation with different perforation cluster spacing. (a). Spacing=6m; (b). Spacing=10m; (c). Spacing=15m.

Fracture width distribution for the three–fracture array can be seen in **Fig. 25**. With the increase of perforation cluster spacing, fracture width of the middle fracture is decreased, even though the fluid pressure within middle fracture is increasing. This is caused by the strong induced stress from two exterior fractures. Moreover, the change of

fracture spacing has little effect on width of two exterior fractures, since these fractures are affected by much lower magnitude of induced stress compared with the middle fracture.

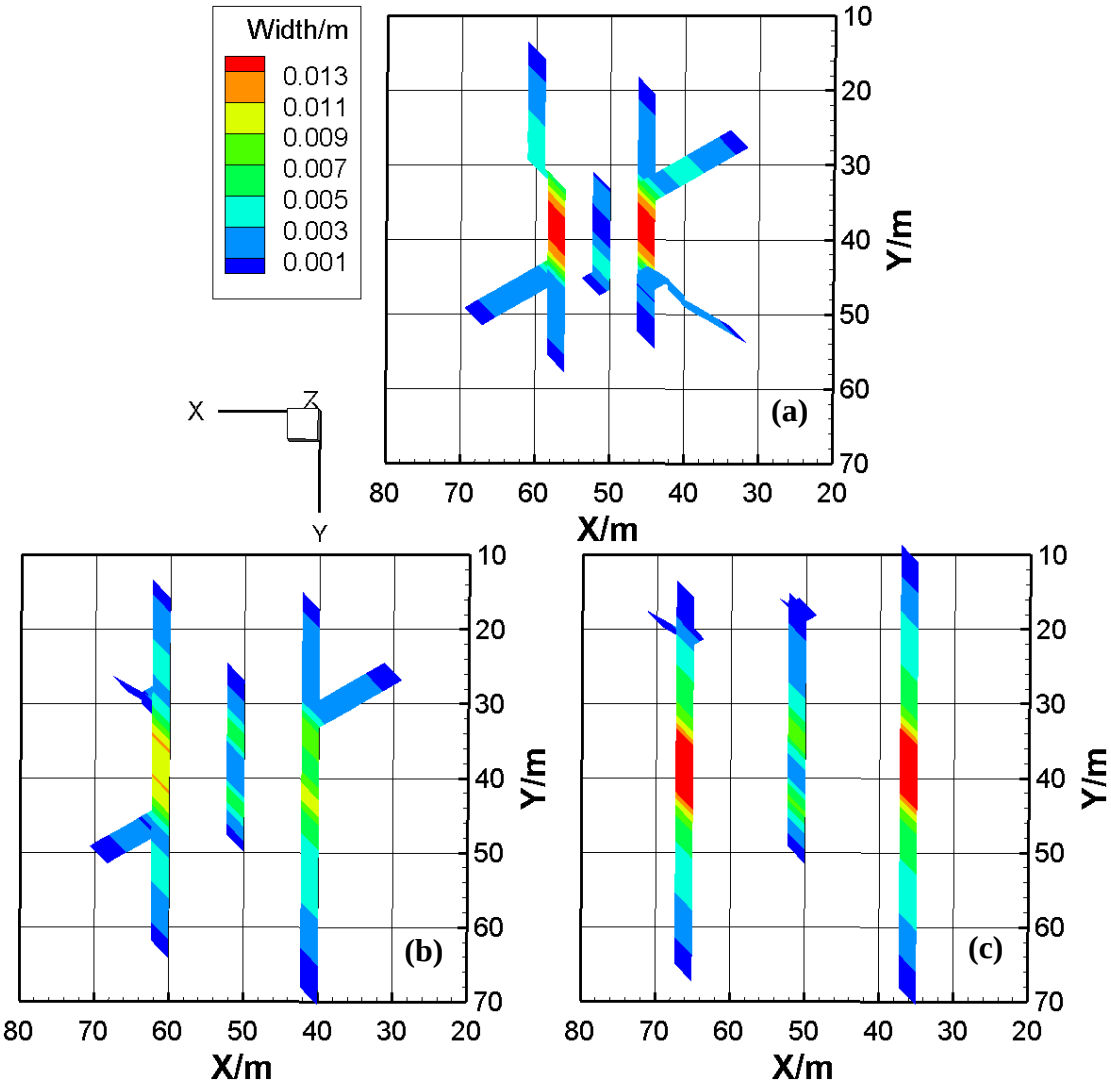

Fig. 25-Multiple fractures width distribution with different perforation cluster spacing. (a). Spacing=6m; (b). Spacing=10m; (c). Spacing=15m.

Fluid leak off through fractures may also affect pore pressure distribution and the magnitude of induced stresses. **Fig. 26** shows fracture propagation patterns for cases with different matrix permeability. With increased matrix permeability, fractures will have fewer branches. For the case with high matrix permeability, fluid leak–off rate is higher, and more time is needed for pressure accumulation. This suggests that for formations with high permeability, poro–elastic effect is an important factor controlling fracture geometries. To increase the fracture complexity of high–permeability reservoirs, large pumping rate associated with high injection pressure is recommended.

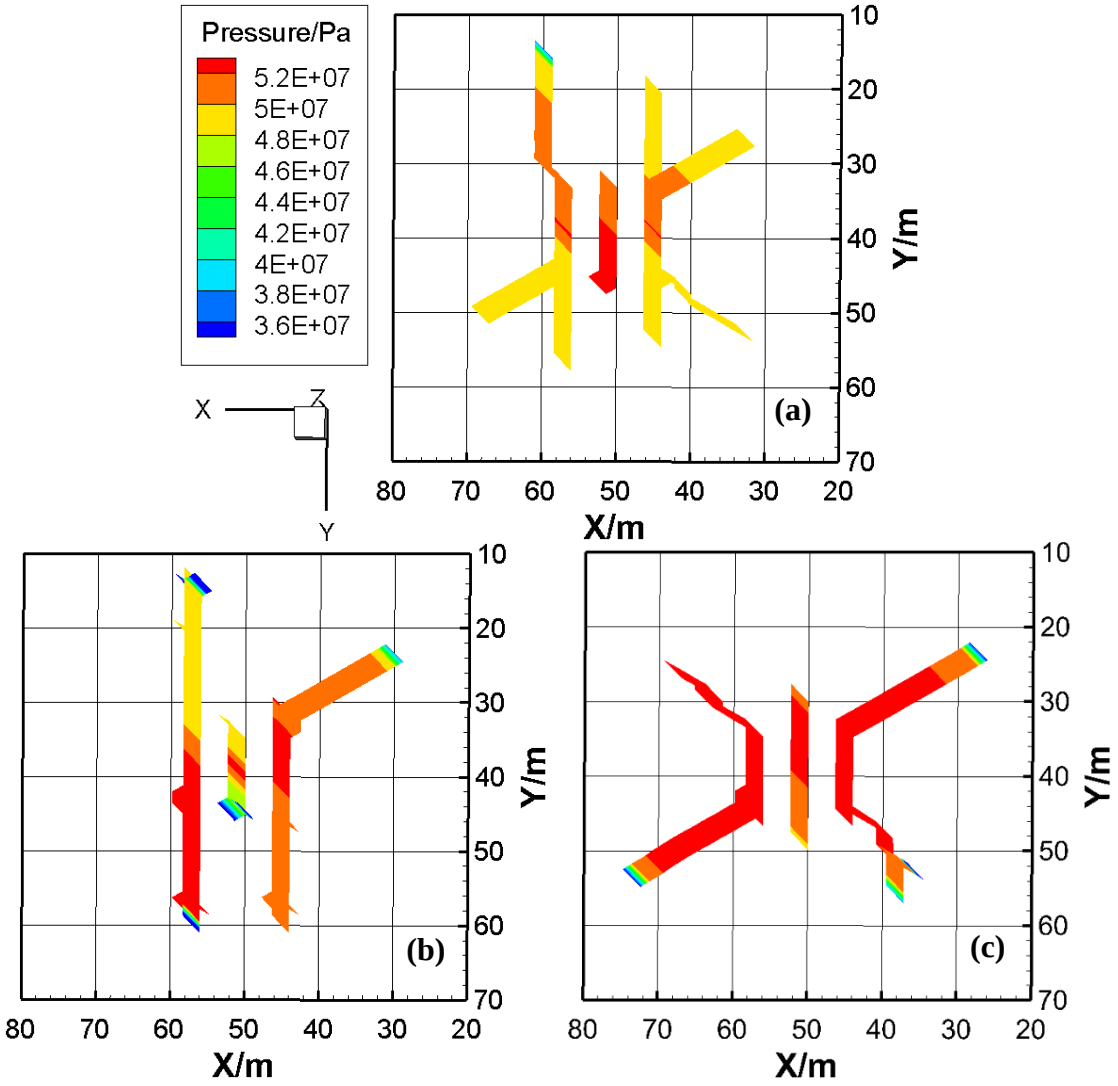

Fig. 26-Propagation of multiple fractures with different matrix permeability. (a). permeability=10^{-6} μm^2; (b). permeability=10^{-5} μm^2; (c). permeability=10^{-4} μm^2.

The effect of injection fluid viscosity on multiple fracture propagation was also investigated. With the increased injection fluid viscosity, fracture length becomes shorter, but fluid pressures within all three fractures are dramatically increased, especially in the

center part of each fracture (**Fig. 27**). High viscosity of injection fluid leads to the large pressure drop rate when fluid flow along fractures. For the case with high injection fluid viscosity, when the fracture length is comparatively long, fluid pressure at the near–wellbore region is required to be extremely high to drive the propagation of fractures. Once the fluid pressure at the near–wellbore region is larger than the stress in maximum horizontal stress direction, a longitudinal fracture can be initiated (**Fig. 27(c)**). This can result in the near–wellbore fracture tortuosity, and proppants has difficulty moving through the tortuous fractures in the near–wellbore damaged region. This indicates that the fracture pumping schedule should be well designed, i.e., the time length for injecting high viscosity fluid cannot be too long, to avoid the generation of near–wellbore fracture tortuosity.

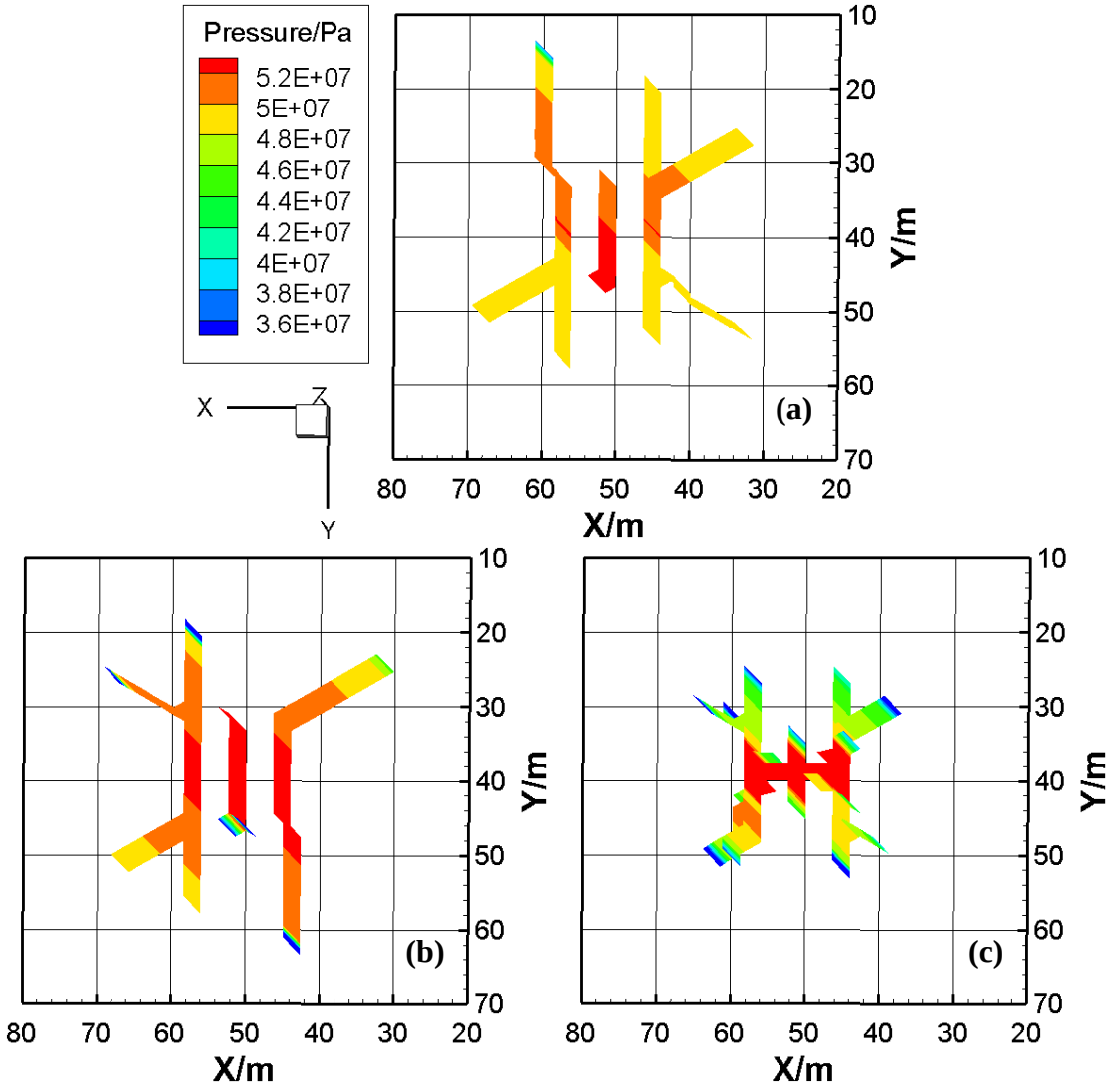

Fig. 27-Propagation of multiple fractures with different viscosity of injection fluid. (a). viscosity=0.003 Pa. s; (b). viscosity=0.03 Pa. s; (c). viscosity=0.3 Pa. s.

4.4 Sequential and alternating hydraulic fracturing

Recently, different fracturing techniques have been proposed to improve effective hydraulic fracture area for unconventional reservoirs development. Two well–known fracturing techniques have been proposed in recent years: Sequential fracturing and

Alternating fracturing. For Alternating fracturing, the third stage is placed between the first stage and the second stage (Rafiee et al. 2012). We ran simulations for both cases with Alternating fracturing sequence and Sequential fracturing sequence. Except for the value of minimum horizontal stress, the input parameters were the same as parameters used in the previous section, and there are three perforation clusters which were fractured according to various schedules. Since it is important to investigate the optimal strategy for fracturing under different geological circumstances, different simulation cases were conducted based on different horizontal stress differences. **Table 4** shows the horizontal stress differences for the three cases.

Case number	σ_h (MPa)	σ_H (MPa)	$\frac{\sigma_h}{\sigma_H}$
1	37.51	44.13	0.85
2	39.72	44.13	0.9
3	43.44	44.13	0.984

Table 4-Details of minimum and maximum horizontal stresses for the three cases.

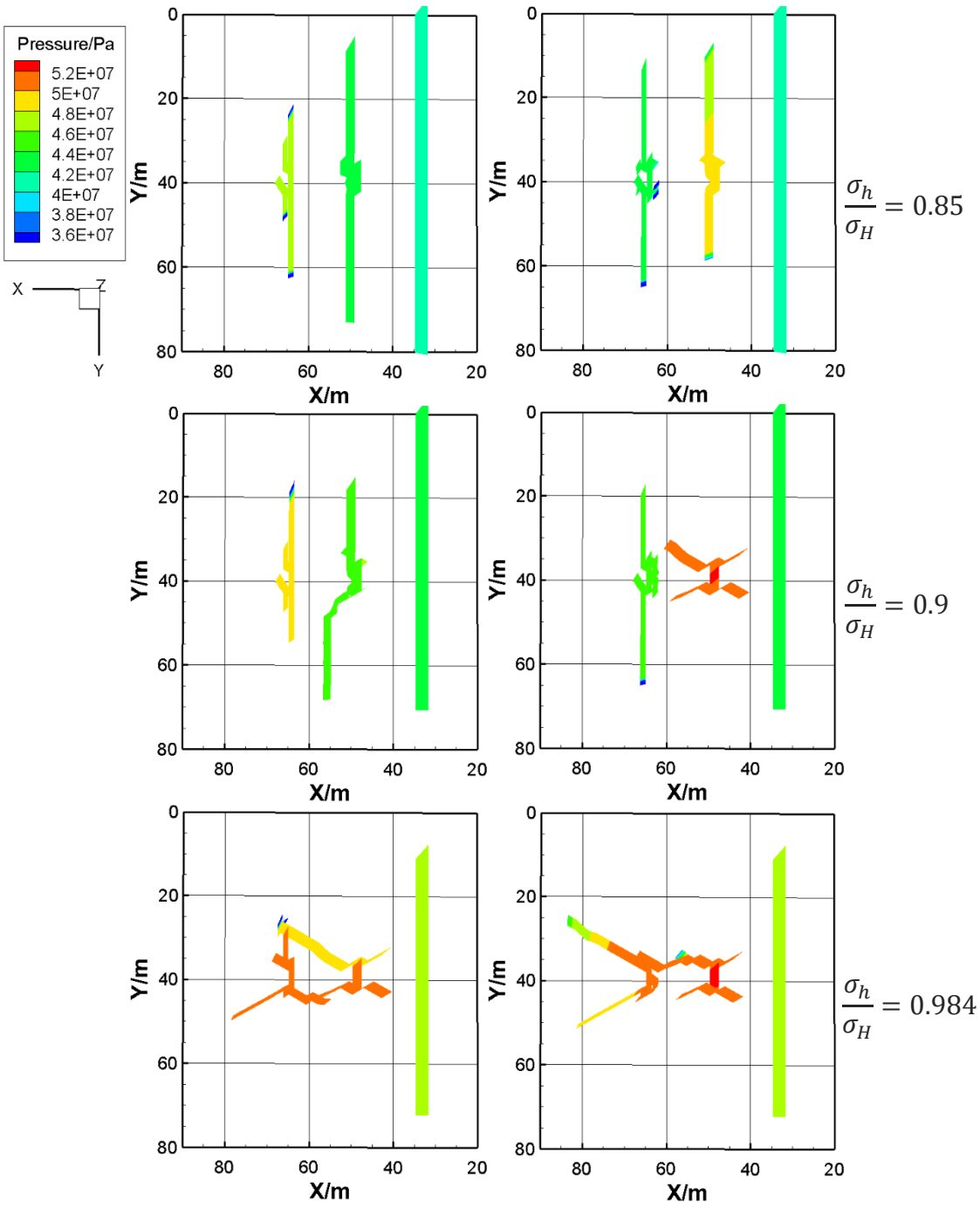

Fig. 28-Fracture propagation simulation with sequential fracturing sequence (left) and alternating fracturing sequence (right).

For case 1, when the horizontal stress difference is large, fractures tend to propagate along the maximum horizontal stress direction (**Fig. 28**). The fractures generated in later stages are always shorter than the fractures generated in earlier stages, since the fractures generated in later stages must overcome larger stress for propagation compared with fractures generated in earlier stages due to the stress shadowing effect. This can also be seen from the higher fluid pressure within the fracture generated in later stages.

For case 2, when $\frac{\sigma_h}{\sigma_H}$ becomes 0.9, fracture pattern of sequential fracturing has similar pattern as case 1. There is a small difference: fracture propagation direction is little deviated from the maximum horizontal stress direction due to the strong induced stress in minimum horizontal stress direction and comparatively small horizontal stress difference. However, for the results of alternating fracturing, longitudinal fracture pattern is generated at stage 3, indicating that the local in–situ minimum horizontal stress direction has a 90–degree rotation. The stress change can also be observed from **Fig. 29**. Fluid pressure within the fracture generated in stage 3 is extremely large, and fracture length is very small. This shows that for the formation with small $\frac{\sigma_h}{\sigma_H}$, alternating fracturing technique may not be a good choice, since the strong induced stress from two exterior fractures can cause a high compressive stress region between them, and short longitudinal fracture can be generated at stage 3, which has very small effective fractured area.

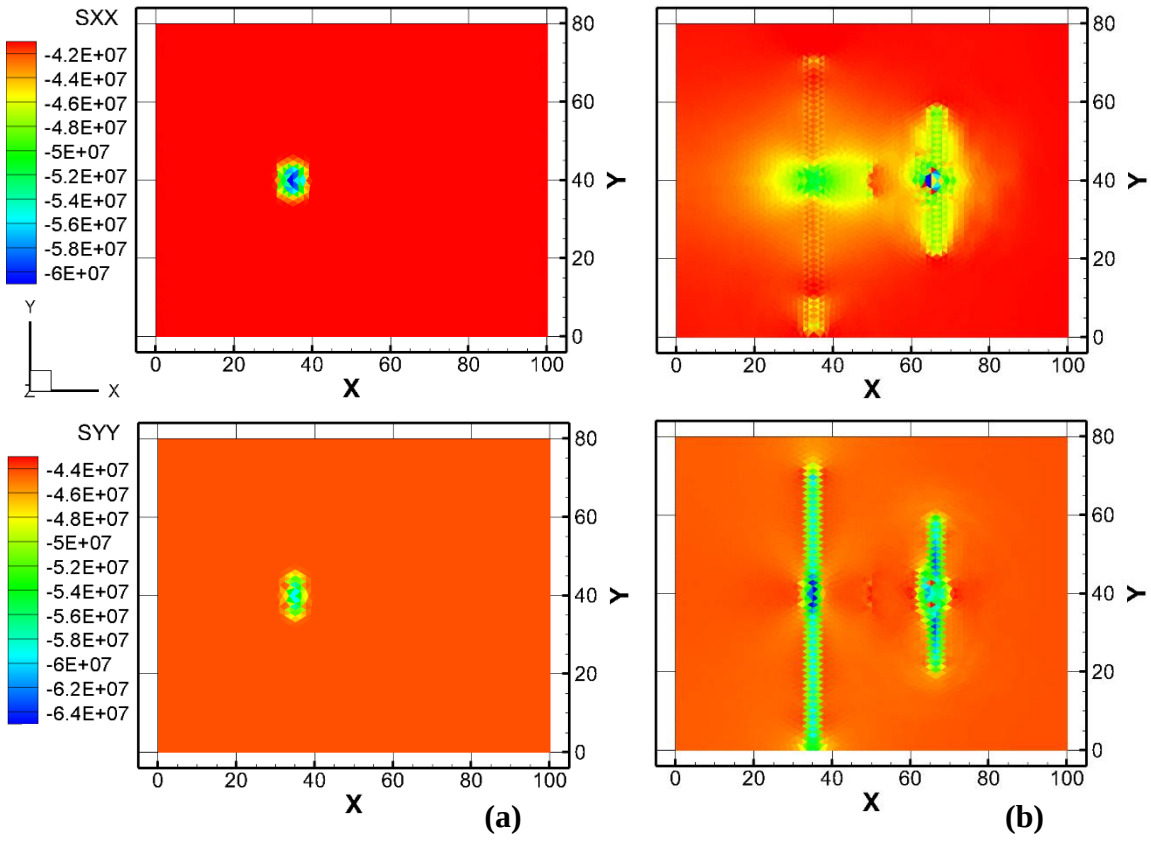

Fig. 29-Stress distribution for case 2 with alternating fracturing. (a). Beginning at stage 1; (b). End of stage 2.

For case 3, since the initial horizontal stress difference is very small (0.69 MPa), the propagation direction of fractures at stage 2 and stage 3 are highly affected by stress shadowing effect from the fracture at stage 1 (**Fig. 30**). Compared with the hydraulic fracture pattern by simultaneous fracturing shown in the previous section, fracture patterns from cases with sequential fracturing and alternating fractures show severe near–wellbore tortuosity, which might result in bad fracturing quality and small effective fracture area. This indicates that for the reservoirs with small horizontal stress difference, simultaneous

fracturing technique can lead to large effective fractured area compared with sequential fracturing and alternative fracturing.

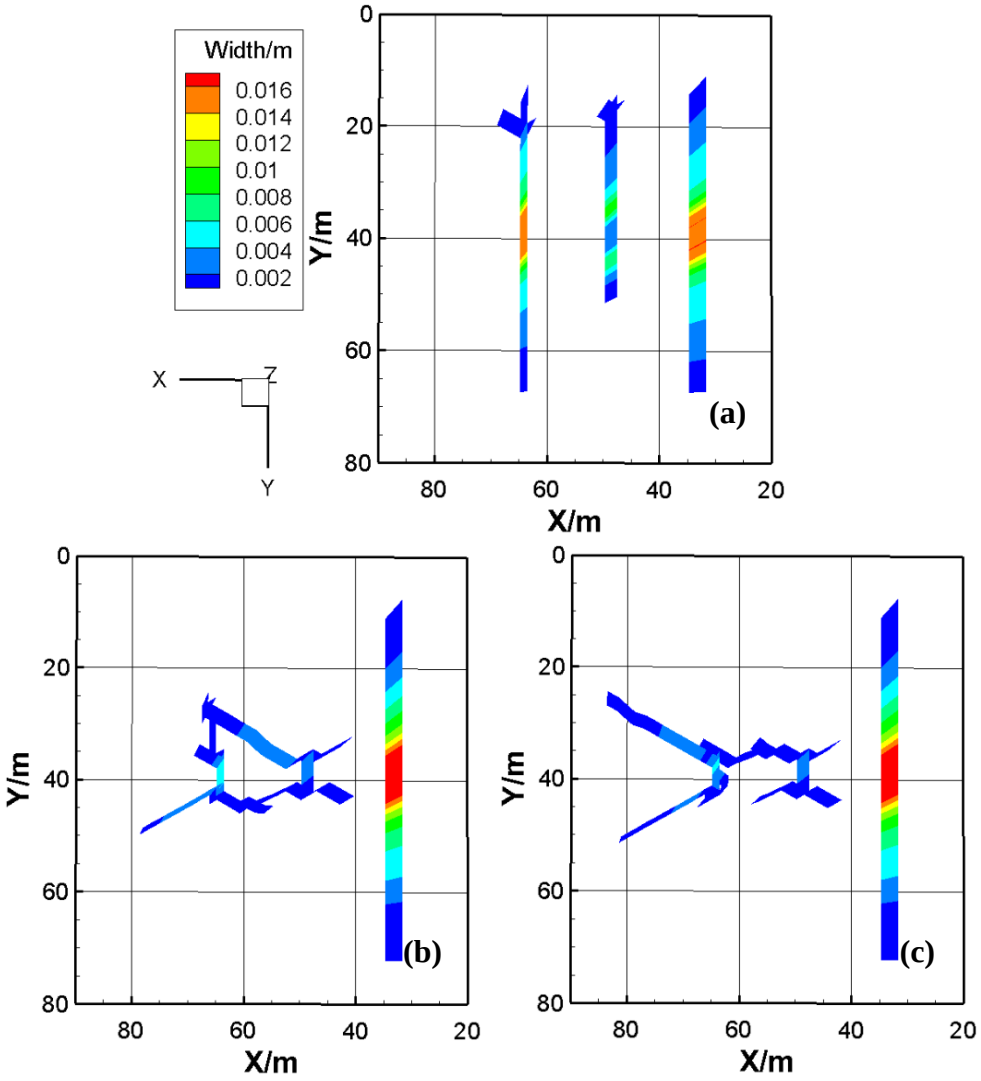

Fig. 30-Fracture width distribution for case 3. (a). Simultaneous fracturing; (b). Sequential fracturing; (c). Alternating fracturing.

Moreover, the summary of the effective fracture area for six cases can be seen in **Table 5**. The threshold of effective fracture width set to be 318 μm (three times 140 mesh size). It shows that for the cases with large horizontal stress difference, results from sequential fracturing and alternating fracturing tend to give larger effective fractured area compared with the case by simultaneous fracturing. One major reason is that for cases with sequential fracturing and alternating fracturing, the fracture at the first stage has longer fracture length since it is not affected by any induced stress during propagation. For the case with very small horizontal stress difference, fracture pattern from the case with simultaneous fracturing shows the largest effective fracture area. Moreover, since the fracture at the last stage is subjected to strong stress shadowing effect, near–wellbore fracture tortuosity and longitudinal fractures can be observed from both cases with sequential fracturing and alternating fracturing. This type of fractures can cause a large positive skin factor in hydrocarbon productivity, which means that it has a negative effect on hydrocarbon production.

Horizontal stress ratio	Fracturing technique	A_{eff} Stage 1 (m^2)	A_{eff} Stage 2 (m^2)	A_{eff} Stage 3 (m^2)	Total A_{eff} (m^2)
$\frac{\sigma_h}{\sigma_H} = 0.85$	Simultaneous	63.2	34.1	63.2	160.5
	Sequential	73.8	62.1	36.3	172.2
	Alternating	73.8	60.7	44.3	178.8
$\frac{\sigma_h}{\sigma_H} = 0.984$	Simultaneous	54.5	36.6	54.7	143.9
	Sequential	60.3	54.12	21.0	135.42
	Alternating	60.3	36.56	31.25	128.1

Table 5-Summary of effective fracture area for cases with different fracturing techniques and various horizontal stress difference.

4.5 Conclusions

This section presented the investigation of propagation of multiple fractures in unconventional reservoirs. Sensitivity studies were conducted to investigate the fracture propagation behavior under different geological and operational circumstances. Several conclusions have been made based on the studies. For example, hydraulic fracturing treatments with high injection fluid viscosity can generate shorter and wider fractures. However, the pumping schedule should be carefully designed, since long time injection with high viscosity fracturing fluid may result in near–wellbore fracture tortuosity and generation of longitudinal fractures, and proppants transport becomes difficult through the complex fractures in the near–wellbore damaged region.

Moreover, fracture propagation simulations were conducted based on several modern hydraulic fracturing strategies, including simultaneous fracturing, sequential fracturing and alternating fracturing. With the same number of perforation clusters in the simulation domain, results show that for the case with small initial horizontal stress difference, simultaneous fracturing is a good choice which can give larger effective fracture area. Using sequential fracturing and alternating fracturing techniques will lead to smaller effective fracture area, and it is highly likely that near–wellbore fracture tortuosity will be generated. For cases with large initial horizontal stress difference, sequential fracturing and alternating fracturing techniques are better choice since using these techniques we can get very large fracture area at stage 1, and the total effective fracture area is larger than in the case using simultaneous fracturing technique.

5. PROPAGATION OF SINGLE AND MULTIPLE FRACTURES IN NATURALLY FRACTURED RESERVOIRS

5.1 Natural fractures characterization

NFs are known to play an important role in production from unconventional reservoirs. The classification of NFs is based on the displacement direction relative to the orientation of the discontinuity (Pollard et al. 1988). The common terms joint or vein suggest a natural rock fracture formed predominantly by mode I movement. Veins are the NFs containing mineral cement, and joints are barren, sealed or partly sealed fractures. A fault is a discrete fracture formed predominantly by mode II and/or mode III movements (Gale et al. 2014).

The properties of NFs, including fracture size, aperture width, abundance and mechanical properties etc. have been investigated by many geologists to characterize and understand NFs. Core and outcrop data are commonly used to characterize NFs' mineralization, strike orientation and size patterns (Gale et al. 2014). Other techniques, including tomographic fracture imaging (Geiser et al. 2012), SEM based examination (Gale et al. 2007), and microseismic event interpretation (Williams–Stroud et al. 2010) have been utilized in recent years for NF characterization.

Fracture aperture is defined as the kinematic aperture (distance between fracture walls) which includes both opened and sealed NFs (Gale et al. 2014). Compared with fracture length and height, characterizing the fracture aperture is more practical since sometimes fracture lengths and heights are truncated by limits in core extent. Two typical

fracture aperture distribution correlations are widely applied in geological and reservoir modeling: log–normal distribution and power–law distribution (Gong and Rossen 2014; Dreuzy et al. 2001). Gale et al. (2014) have collected kinematic aperture data from reports of several shale formations, and summarized the kinematic aperture dataset from other published literatures. **Fig. 31** shows the kinematic aperture distribution for all datasets which appears to be in good agreement with power law distribution.

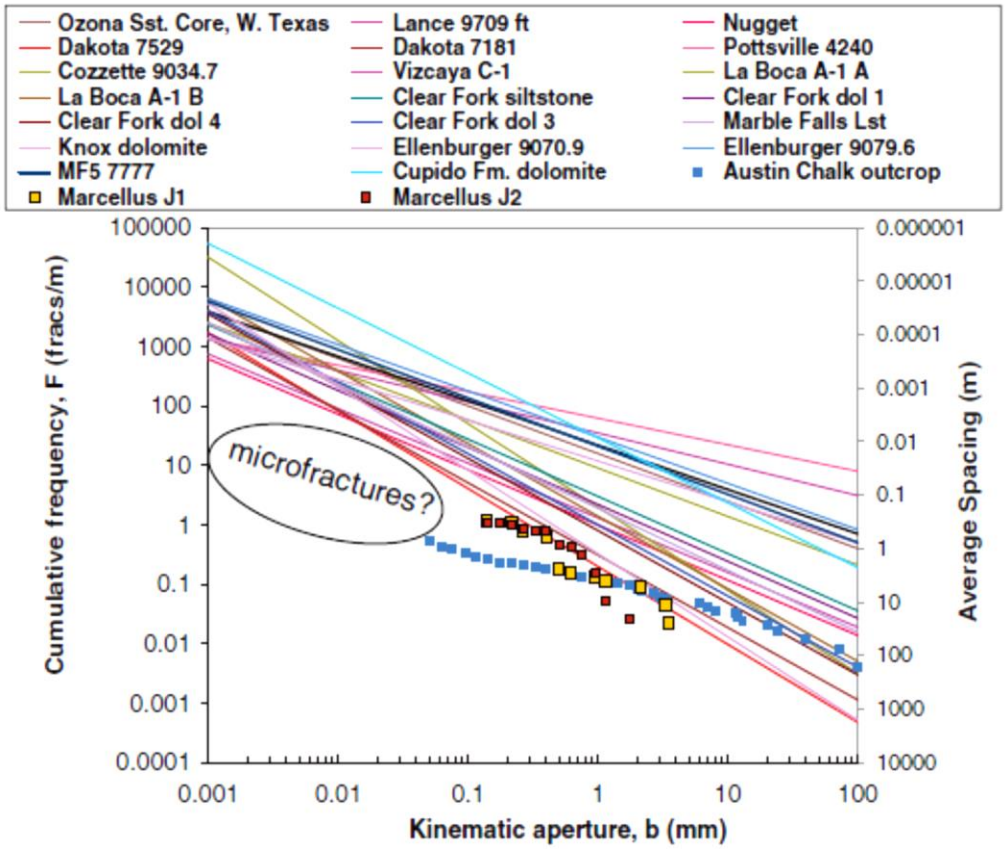

Fig. 31-Overview of fracture kinematic aperture distribution from published literature (Gale et al. 2014).

NFs, especially sub–vertical NFs in unconventional formations are commonly arranged in subparallel sets (Hancock 1985). Typically, more than one consistent set of fractures are observed in the same region (Gale 2014). After one set of fractures was well developed, the forming of the new fracture set is affected by the induced stress from the well–developed set of fractures (Han 2011). Therefore, several sets of fractures may have developed under the same stress regime, and in a specific time frame the fracture orientations are in a narrow range (Hodgson 1961; Hancock 1985). Highly variable fracture patterns may also form due to the following several reasons: weathering effect (Fidler 2011), abrupt stress change from bed to bed (Engelder et al. 2009) and fractures form at different time with stress distribution evolution (Gale et al. 2014). Fractures of different sets sometimes have different spacing in the same layers (Engelder et al. 2009).

Usually fracture length is considered to have a power–law distribution (Nicol 1996; Odling 1997; Gong and Rossen 2014). Gong and Rossen (2014) utilized a scaled power–law distribution function to build the fracture network model:

$$f(x) = \frac{\gamma - 1}{x_{min}}\left(\frac{x_{min}}{x}\right)^{\gamma} \quad (5.1a)$$

$$F(x) = 1 - \left(\frac{x_{min}}{x}\right)^{\gamma-1} \quad (5.1b)$$

Here, $\boldsymbol{\gamma > 1}$ is the power law exponent, $\boldsymbol{x}$ is fracture length and $\boldsymbol{x_{min}}$ is the lower threshold on $\boldsymbol{x}$, $\boldsymbol{f(x)}$ is the probability density in units of (1/m), and $\boldsymbol{F(x)}$ is the cumulative probability density, dimensionless.

As an example, let us consider the total number of NFs is 1000. Then the number of fractures with length less than *x* meters is:

$$N(x) = 1000\,F(x) = 1000\left[1 - \left(\frac{x_{min}}{x}\right)^{\gamma-1}\right] \ldots\ldots\ldots\ldots\ldots\ldots\ldots\ldots\ldots\ldots\ldots\ldots\ldots\ldots\ldots (5.2a)$$

and the frequency of fractures is:

$$n(x) = 1000\,f(x) = 1000\frac{\gamma - 1}{x_{min}}\left(\frac{x_{min}}{x}\right)^{\gamma} \ldots\ldots\ldots\ldots\ldots\ldots\ldots\ldots\ldots\ldots\ldots\ldots\ldots\ldots\ldots (5.2b)$$

Here ***N(x)*** is unitless and ***n(x)*** has unit of m^{-1}.

Stochastic realization method was applied by several researchers for fracture network modelling (Wu and Olson 2015b):

$$n(l)\Delta l = Cl^{-a} \ldots\ldots\ldots\ldots\ldots\ldots\ldots\ldots\ldots\ldots\ldots\ldots\ldots\ldots\ldots\ldots\ldots\ldots\ldots\ldots\ldots\ldots (5.3)$$

Here $\boldsymbol{n(l)\Delta l}$ is the number of NFs with a length in the range $\boldsymbol{(l, l+\Delta l)}$, $\boldsymbol{C}$ is a coefficient of proportionality whose unit is m^{-1}, and $\boldsymbol{a}$ is an exponent (Wu and Olson 2015b). $\boldsymbol{n(l)}$ has the unit of m^{-1}. **Fig. 32** shows the plot for fracture length distributions with different value of $\boldsymbol{a}$ (Wu and Olson 2015b). The figure was prepared fixing Δl=1 m.

Researchers have set various minimum cut–off fracture length in their models. Gong and Rossen (2014) set the minimum cut–off fracture length $\boldsymbol{x_{min}}$= 0.6 m. McClure et al. (2015) set the fracture length range to be 30–70 m. Researchers gave little explanation on the mechanisms of how to determine the minimum and maximum cut–off length of NFs. Summarizing several cases of fracture network model setup (Gong and Rossen 2014; McClure et al. 2015; Wu and Olson 2015b), indicates that models with large simulation domain size correspond to large minimum fracture cut–off length and vice versa.

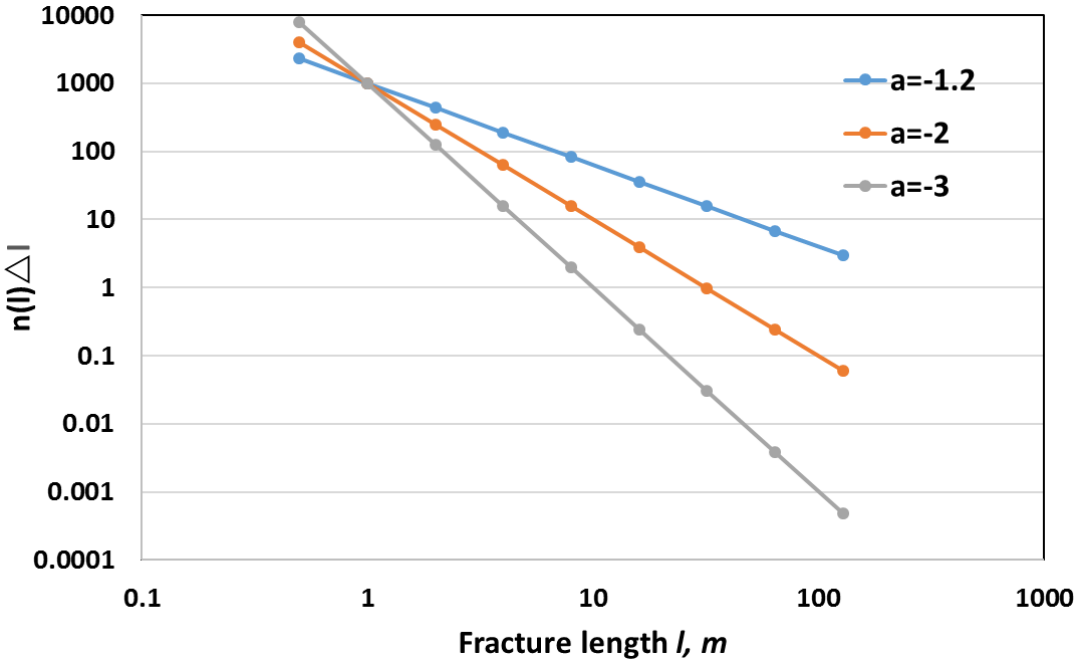

Fig. 32-Illustration of the fracture length distribution following "power law distribution" with various values of exponent *a* (after Wu and Olson. 2015b).

5.2 Single hydraulic fracture interacting with natural fractures

Several simulations were performed to investigate three situations: (1) a single HF interacting with two NFs; (2) multiple fractures propagating simultaneously interacting with NFs; and (3) complex fracture network evolution in naturally fractured reservoirs at field scale. Simulations were conducted based on the input parameters given in **Table 6**. If any value of input parameters is different from the value shown in **Table 6**, it is emphasized. For studies of a single HF interacting with NFs, we choose the domain size to be 100m×100m. The perforation is located at the center of the domain, and the horizontal wellbore is from (0m, 50m) to (100m, 50m).

Matrix parameters		**NFs parameters**	
Permeability ($\times 10^{-3}$ μm^2)	0.001	Permeability ($\times 10^{-3}$ μm^2)	0.01
Minimum horizontal stress (MPa)	40.9	Cohesion (MPa)	1.0
Young's modulus (GPa)	40.0	Friction angle (°)	30.0
Poisson's ratio	0.21	Tensile Strength (MPa)	1.0
Tensile Strength (MPa)	4.0	**Treatment parameters**	
Cohesion (MPa)	4.0	Injection rate (m^3/s)	0.1
Friction angle (°)	30.0	Fluid viscosity (Pa·s)	0.003
Pore Pressure (MPa)	28	Number of perforation cluster	1

Table 6-Input parameters for simulations of one HF interacting with NFs.

Fig. 33 shows the fracture patterns for cases with a single HF interacting with two NFs. In each case, the two NFs have the same properties, including fracture length, orientation, mechanical properties and initial permeability. Simulations were conducted under different initial horizontal stress difference and NFs strike orientation. With the increase of initial horizontal stress difference and the angle of NFs, the fracture tends to

cross the NFs instead of opening them (**Fig. 33**). We compared simulation results with the published experimental and modelling results (**Fig. 22**). Our results exhibit the same trend regarding the HF–NF interaction compared with published experimental and modelling results. For cases with a HF crossing the NFs, an apparent pressure drop was observed at the time of crossing. This is expected because of the relatively high permeability–width product of the NFs.

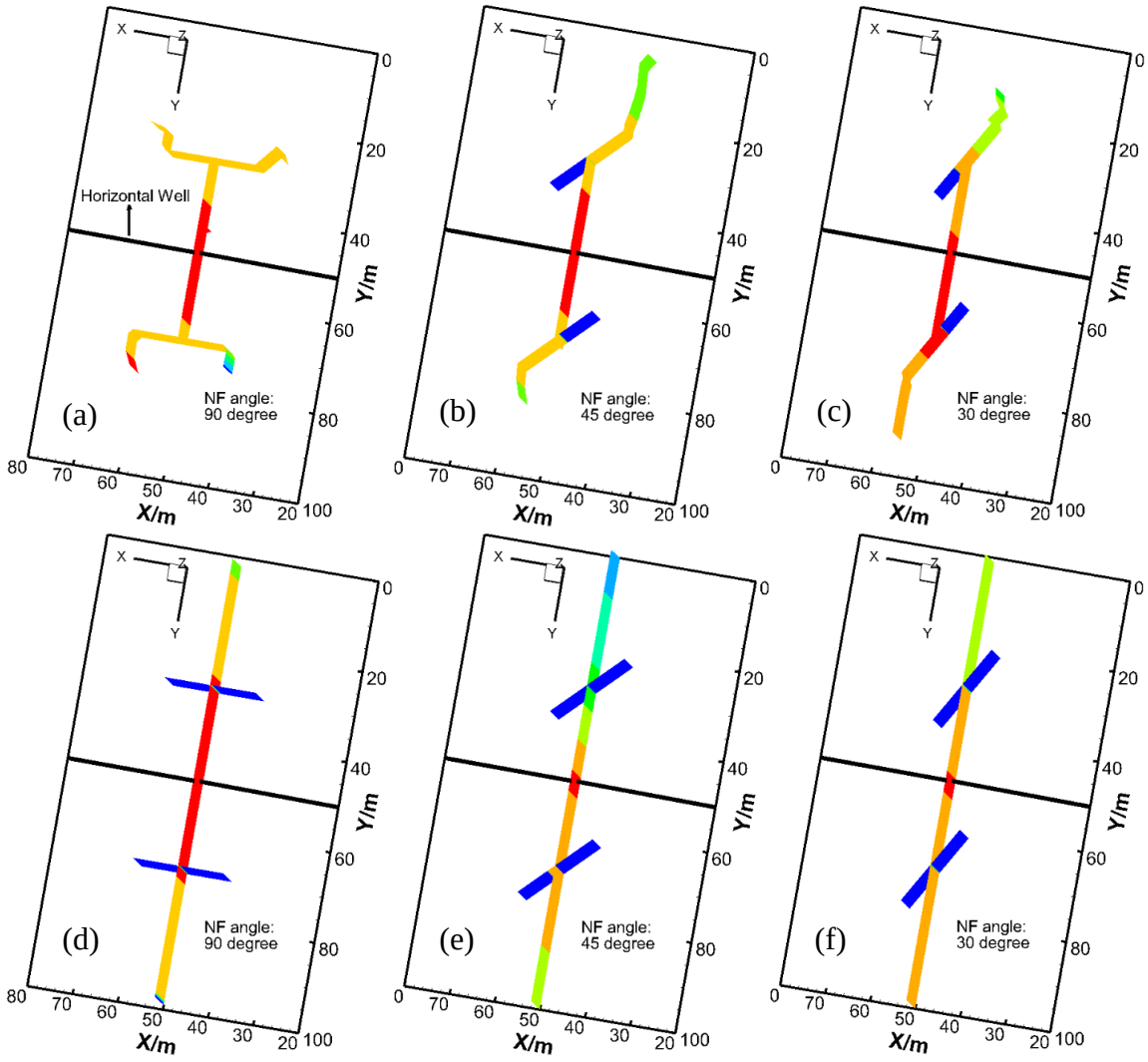

Fig. 33-2D fracture propagation maps with a HF opening NFs (Top) and a HF crossing NFs (Bottom). Initial horizontal stress difference for each case is: (a). 3 MPa; (b). 8 MPa; (c). 12 MPa; (d). 7 MPa; (e). 12 MPa; (f). 20 MPa.

5.3 Multiple−fracture propagation in naturally fractured reservoirs

Simultaneous propagation of multiple fractures has great practical significance. Such a situation arises when several perforation clusters are treated simultaneously in one

fracture stage. For studying simultaneous propagation of multiple fractures interacting with NFs, we investigated the effect of injection fluid viscosity, fracture cluster spacing, and initial permeability of NFs on fracture pattern evolution. **Table 7** shows the supplemental input parameters for these studies, needed in addition to the ones shown in **Table 6**.

Matrix parameters		**Treatment parameters**	
Maximum horizontal stress (MPa)	46.4	Injection rate (m^3/s)	0.24
NFs parameters		Fluid viscosity (Pa·s)	0.009
Permeability ($\times 10^{-3}$ μm^2)	0.1	Perforation cluster spacing (m)	10
Cohesion (MPa)	2	Number of perforation clusters	3

Table 7-Supplemental input parameters for simulations of multi–fracture propagation.

We set three perforation clusters in the domain, and assume each perforation cluster can initiate only one fracture. **Fig. 34** shows the predicted hydraulic fracture network for three cases with different cluster spacing. As can be seen in the figure, with the increase of the fracture cluster spacing, fractures tend to open the NFs instead of crossing them. When the cluster spacing is very small, two exterior fractures propagate away from each other, and the existence of NFs has limited effect on fractures propagation path. When the spacing becomes larger, NFs play a dominant role, and HFs tend to propagate along the NFs.

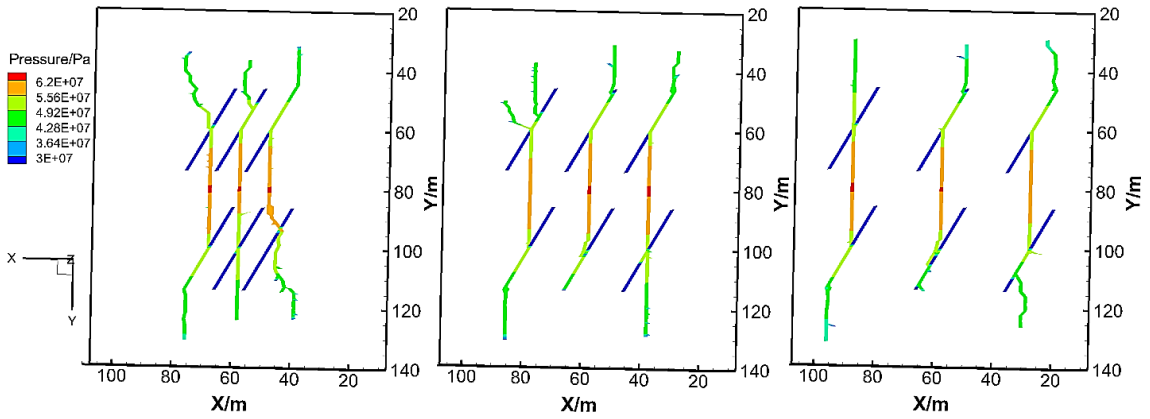

Fig. 34-The effect of fracture cluster spacing on multi–fracture interacting with NFs. Left: cluster spacing=10m; Middle: cluster spacing=20m; Right: cluster spacing=30m.

To study the referenced net pressure distributions along the fractures for different cases with various perforation cluster spacing, we summarized the referenced net pressure

distributions of three fractures for all cases. The notation of referenced net pressure is equal to fluid pressure within the fracture minus the initial minimum horizontal stress. The referenced net pressure in the middle fracture is larger than the pressure in two exterior fractures in all three cases (**Fig. 35**). The difference of the referenced net pressure between middle fracture and exterior fractures is decreased with the increase of cluster spacing. This is resulted from the large decrease of induced stress acting on the middle fracture when cluster spacing is increased.

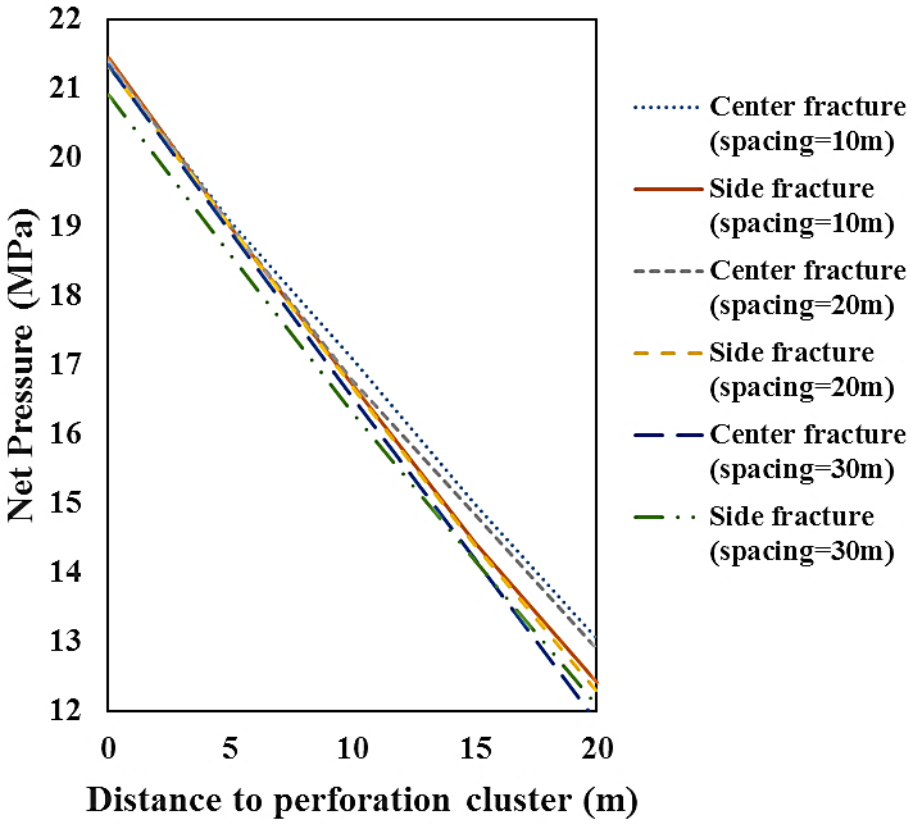

Fig. 35-Net Pressure distribution along middle and exterior fractures for different cases.

The effect of injection fluid viscosity on multi–fracture interacting with NFs was also investigated (**Fig. 36**). With the increase of injection fluid viscosity, the fracture lengths become evenly distributed, and the fractures tend to cross the NFs. Moreover, when the injection fluid viscosity is large enough, the accumulation of pressure at the center part in the middle fracture may ultimately trigger the initiation of a longitudinal fracture along the wellbore, as it is shown in the right image in **Fig. 36**. When the fluid pressure within fractures in the near–wellbore region becomes very large, near–wellbore fracture complexity may emerge. Such a situation can be created if the injection fluid has high viscosity. However, the fracture network length will become smaller compared with cases with smaller injection fluid viscosity.

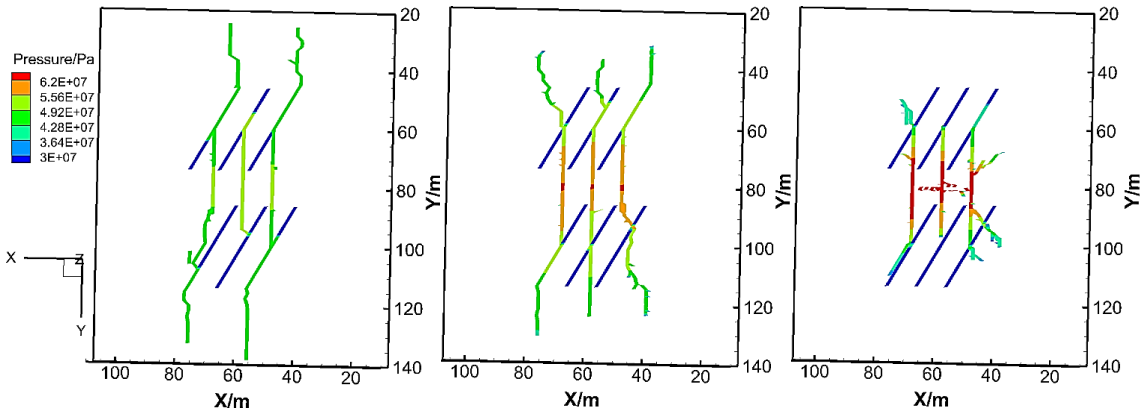

Fig. 36-The effect of injection fluid viscosity on multi–fracture interacting with NFs. Left: viscosity=0.009 Pa.s; Middle: viscosity=0.09 Pa.s; Right: viscosity=0.9 Pa.s.

Next, simulations were conducted with different initial NF permeability. Higher initial NF permeability causes the fracturing fluid preferentially penetrate to the NFs. For the case with large initial NF permeability, most HFs propagate along the NFs for a while and later restart the propagation in the matrix rock with the direction almost parallel to the maximum horizontal stress direction (**Fig. 37**). For the case with small initial NF permeability, fractures tend to cross the NFs.

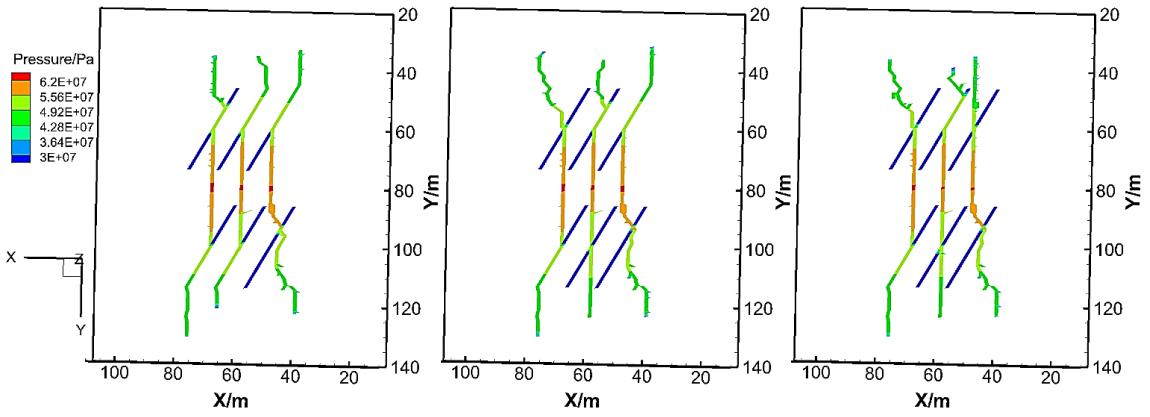

Fig. 37-The effect of NF initial permeability on multi–fracture interacting with NFs. Left: permeability=0.1×10^{-3} μm^2; Middle: permeability=0.01×10^{-3} μm^2; Right: permeability=0.001×10^{-3} μm^2.

5.4 Complex fractures propagation in naturally fractured reservoirs in regional scale

As described in the first sub–section of this section, NF characterization is a popular topic and several observations have been put forward regarding NF properties,

including length distribution, abundance, fracture sets and patterns etc. (Gale et al. 2014; Geiser et al. 2012; Williams–Stroud et al. 2010). In this section, we describe simulations to study the effect of NF properties on complex fracture propagation. Firstly, we investigate the effect of the value of power–law exponent ***a*** on fracture propagation. The exponent ***a***, which is shown in Eq. 5.3 and Eq. 5.4, should be assigned a large value if we try to build a NF distribution network with more number of short NFs and less number of long NFs. If the value of exponent ***a*** is small, the length will be more evenly distributed. **Fig. 38** shows the fracture length distribution with different value of exponent ***a***. Here, ***dl*** is set to 4 m, the minimum fracture length is 8 m, and the maximum fracture length is 36 m. Simulation domains have the size 200 m×300 m, and the minimum and maximum horizontal stress is set to be 40.9 MPa and 42.6 MPa. Some input parameters for simulations are shown in **Table 8**.

NFs parameters		**Treatment parameters**	
Total number of NFs	200	Number of perforation clusters	3
Range of NFs strike orientation	40°–60°	Perforation clusters spacing (m)	30
Range of NFs length (m)	8–36	Injection rate (m^3/s)	0.24

Table 8-Supplemental NFs and treatment parameters.

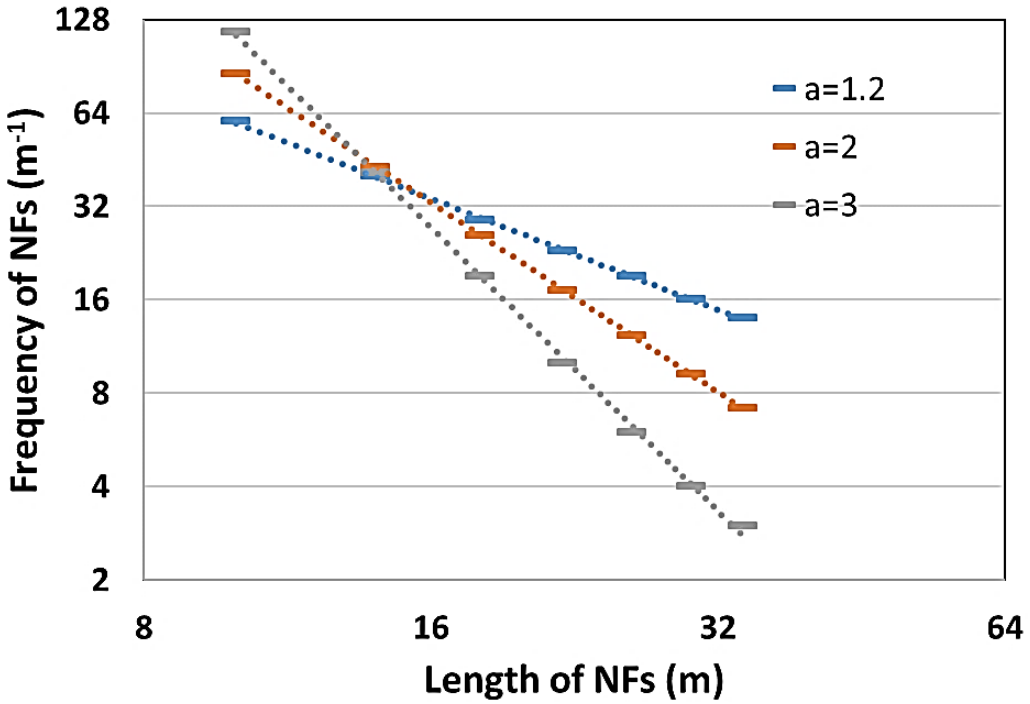

Fig. 38-Fracture length distribution following power law distribution with various values of exponent a.

Fig. 39 shows the predicted hydraulic fracture network for all three cases with different values of exponent ***a***. With the decrease of the value of ***a***, strike orientation of NFs has a dominant effect on fracture propagation direction (**Fig. 39**). To be more specific, for the case with ***a***=1.2, most fractures tend to propagate along the strike orientation of NFs, especially in the region far away from wellbore. When the value of ***a*** is larger, the strike orientation of NFs has less effect on fracture network propagation orientation.

The predicted complex fracture network for all three cases with failure mode indicator can be seen in the bottom three maps in **Fig. 39**. Fractures marked in red were opened by shear failure, and fractures marked in green were opened by tensile failure.

With the increase of the value of ***a***, the length of fractures opened by shear failure increases. The percentage of total length of fractures opened by shear failure for different cases is shown in **Fig. 40**.

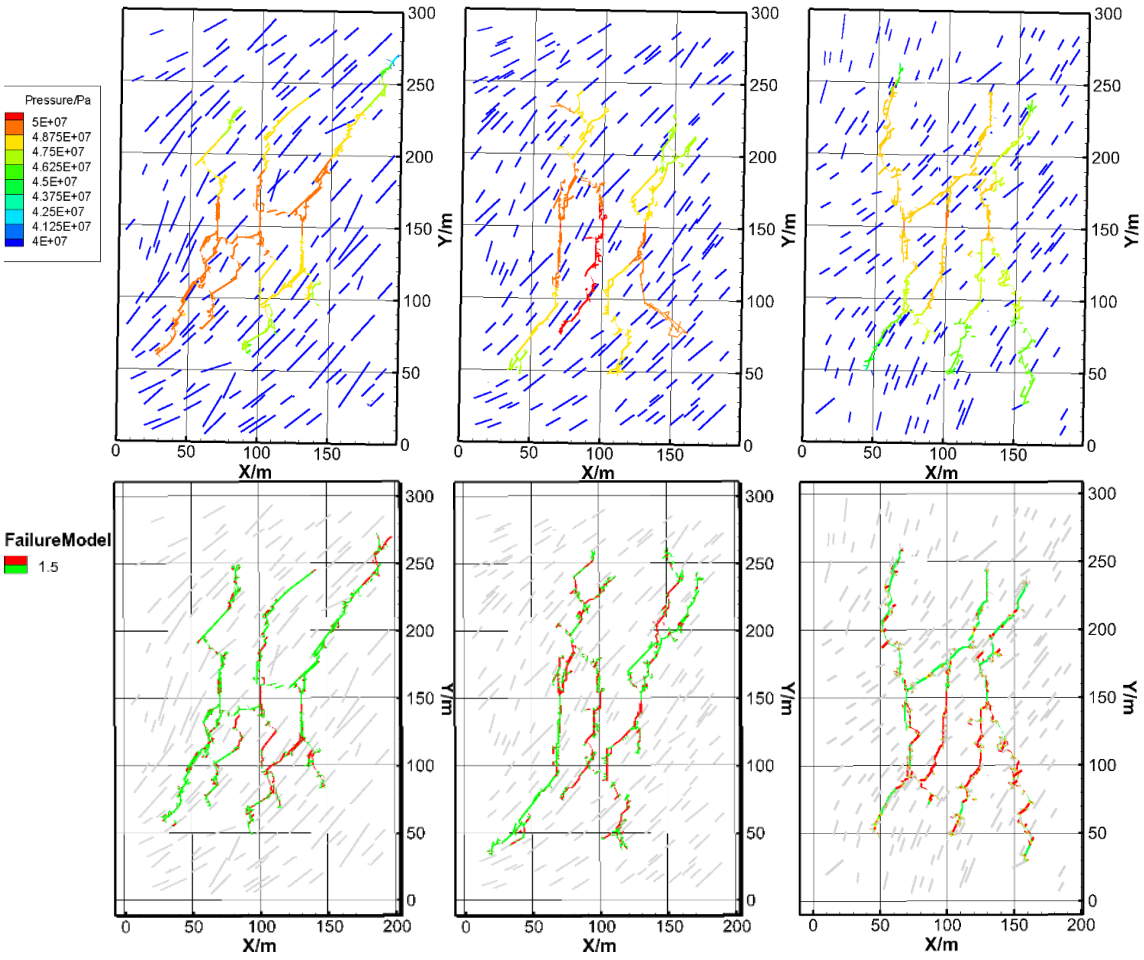

Fig. 39-The effect of exponent a on complex fracture propagation. Left: a=1.2; Middle: a=2; Right: a=3; Top: maps with fluid pressure distribution; Bottom: maps with failure mode indicator.

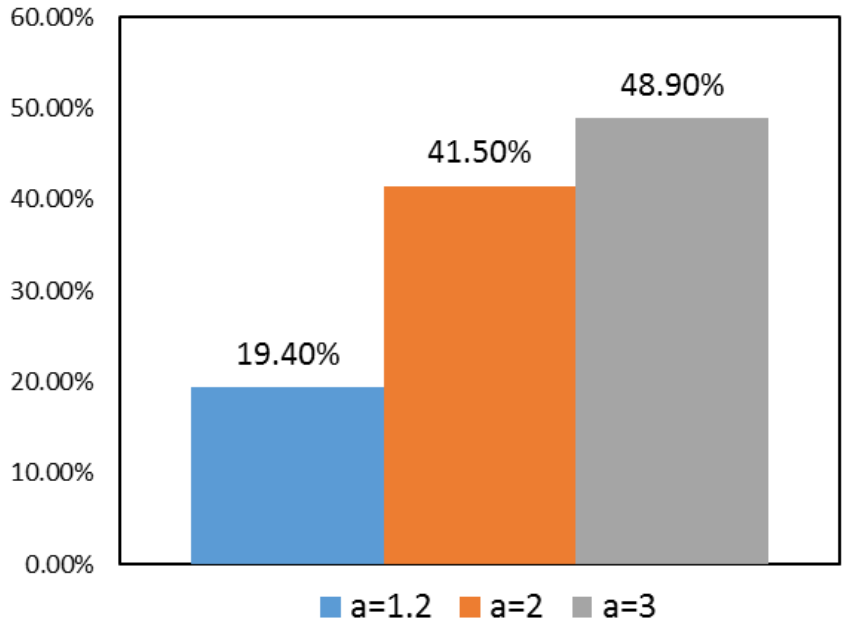

Fig. 40-Percentage of total length of fractures opened by shear failure for three cases.

Since more than one set of NFs is commonly observed in a regional scale, in this scenario, simulations with different number of NFs set have been conducted. It is noted that the number of NFs is fixed whatever the number of NFs sets are. As can be seen in **Fig. 41**, for the case with one NFs set, fractures tend to propagate along the strike orientation of NFs. However, for cases with more than one set of NFs, directions of fracture propagation are diverse.

Maps of fracture width distribution for different cases are shown in the bottom three pictures in **Fig. 41**. Fractures in grey represent the fractures that either are not opened or the width is so small that even very fine mesh of proppants (e.g. 140) cannot pass the fracture. With the increase of the number of NFs sets, the unpropped fracture length

becomes longer. Interestingly, for cases with one set or two sets of NFs, the unpropped fractures occur only at the tips of fracture networks (**Fig. 41** and **Table 9**). However, for the case with three sets of NFs, the narrow throat of fractures occurs in the middle of fracture networks and may block the proppant transport. This will result in a much smaller effective fractured area. Since NFs have relatively high permeability compared with rock matrix, fluid can smoothly penetrate to NFs when propagating fracture network intersecting with them. The high diversity of strike orientation of NFs can result in large increase in the magnitude of the minimum principal stress at a local region due to the stress shadowing effect from neighboring pressurized complex fracture network.

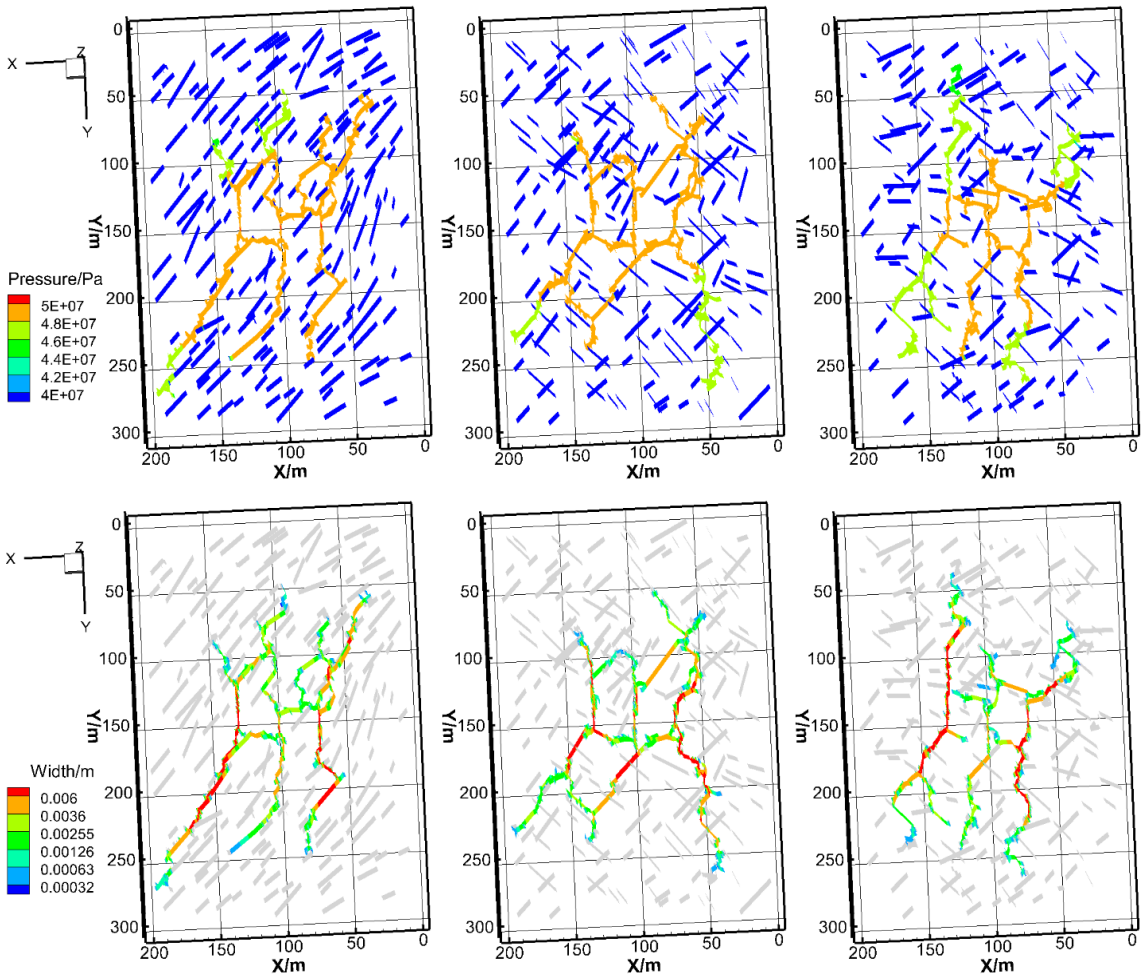

Fig. 41-The effect of numbers of NF sets on complex fracture propagation. Left: 1 set; Middle: 2 sets; Right: 3 sets; Top: maps with fluid pressure distributions; Bottom: maps with fracture width distributions.

The number of NFs set	Percentage of unpropped fractures	Unpropped part in complex fracture network
1	2.5%	Fracture tips
2	3.8%	Fracture tips
3	6.3%	Fracture tips & Middle of fracture network

Table 9-Percentage of unpropped fracture length for different cases.

Fracture clustering has been observed in some unconventional formations (Gale et al. 2014). For this case, we investigated the degree of fracture clustering on complex fracture propagation in naturally fractured reservoirs. In **Fig. 42**, there is a defined area (dark grey) where fracture density may differ from other areas in the simulation domain. **Table 10** shows the details regarding the degree of fracture clustering for different cases.

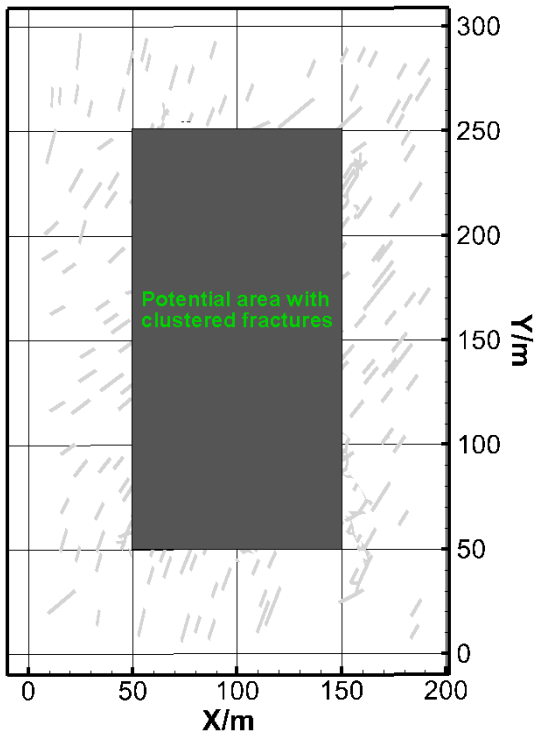

Fig. 42-Illustration of defined potential area with highly clustered fractures in the simulation domain.

	Uniform Distribution	**Clustered Fractures**	**Unit**
NFs density in the defined area	0.06	0.105	NFs length per area (m/m^2)
NFs density in other area	0.06	0.0375	NFs length per area (m/m^2)

Table 10-Parameters of fracture clustering for different cases.

The predicted complex fracture maps can be seen in **Fig. 43**. It is noted that for different cases, the total number of NFs are same. For the case with clustered fractures in

defined area, the degree of fracture network complexity in the defined area is higher than the case with uniformly distributed NFs. Moreover, with the increase of the degree of fracture clustering, length of fractures induced by shear failure is much longer than the fractures induced by tensile failure. For the case with uniformly distributed NFs, most of fractures are induced by tensile failure.

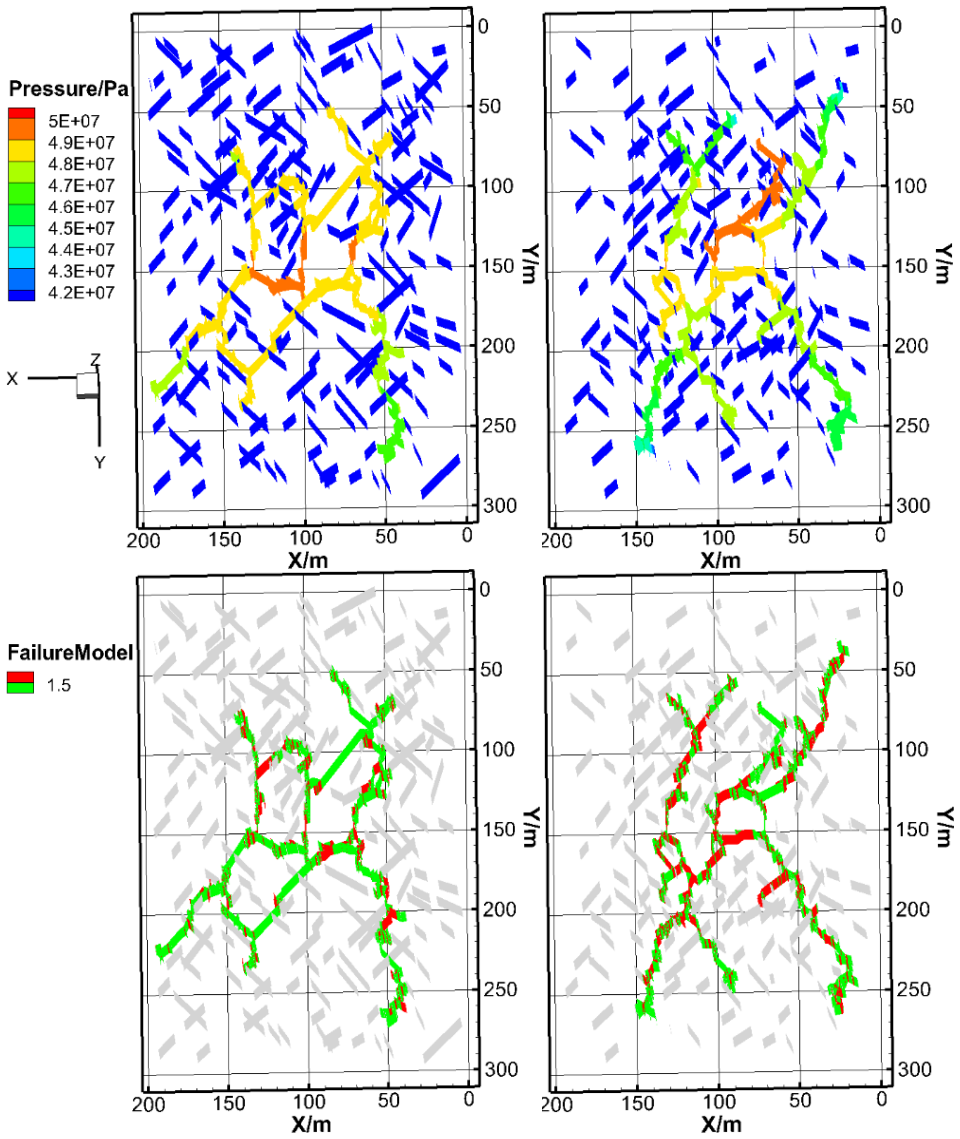

Fig. 43-The effect of fracture clustering on complex fracture propagation. Left: randomly distributed fractures; Right: fractures are clustered; Top: maps with fluid pressure distribution; Bottom: maps with failure mode indicator.

5.5 Discussion and conclusions

This section reports simulations designed to investigate single fracture and complex fracture network propagation in naturally fractured reservoirs. In hydraulic

fracturing treatments, opening of NFs is determined by geological and NFs properties, such as NF strike orientation, NF initial permeability, magnitude of three principal stresses, and NF tensile strength and cohesion etc. For multiple fractures propagation in naturally fractured reservoirs, stress shadowing effect plays a key role in fracture network evolution.

We developed a discretized NF network builder for complex fractures propagation in naturally fractured reservoirs. This builder can export the discretized NF network information which matches the geological observation of NF properties. Geological properties of NFs dramatically influence complex fracture patterns, propped fracture area, fracture propagation direction and fracture failure mode, etc.

For simulation cases with small values of power law exponent $\boldsymbol{a}$, results show that fractures tend to propagate along strike orientation of NFs, and the length of fractures opened by tensile failure increases. For cases with different number of NF sets, when the number of NF sets increases, the fracture network propagation direction becomes diversified. This results in complex local induced stress, which may result in a strong stress shadowing effect in a specific region. The opened NFs in this specific region will have extremely small fracture width, which may block proppant transportation. For cases with clustered NFs in designed area, simulation results show that the opened fracture density is large and opened fracture network is complex. The complexity suggest that the fracture network not only has high fracture density, but also has diversified fracture propagation direction. These studies offer insights for designing pumping schedule and proppant selection for hydraulic fracturing operations in naturally fractured reservoirs.

6. FRACTURE EVOLUTION IN LAMINATED RESERVOIRS [**]

6.1 Introduction

Typically, shale formations are multilayered structures and exhibit mechanical anisotropic properties. The laminated structure can cause fracture propagation along the BP interfaces (Chuprakov et al. 2015; Li et al. 2014). Such geological media exhibit transversely isotropic mechanical behavior, which means that five independent mechanical material constants: $\boldsymbol{E_h, E_v, V_h, V_v}$ and $\boldsymbol{G}$ (Thiercelin et al. 1994) are needed for mechanical characterization. Here, $\boldsymbol{E_h}$ and $\boldsymbol{E_v}$ are Young's moduli in horizontal and vertical direction, respectively, $\boldsymbol{V_h}$ and $\boldsymbol{V_v}$ are Poisson's ratios in horizontal and vertical direction, respectively, and $\boldsymbol{G}$ is shear modulus. Zou (2015) reported the results of tri–axial loading tests for shale samples from the Sichuan basin in China (**Table 11**). For the experimental studies, the confining pressure was set to be 20 MPa. It shows that $\boldsymbol{E_h > E_v}$, and $\boldsymbol{V_h < V_v}$.

The mechanisms of fracture growth in unconventional reservoirs have been studied in past decades using both experimental and modelling techniques (Weng 2015; Olson et

---

[*] Part of this section is reprinted with permission from "Numerical Investigation of Multi–Well, Multi–Stage Hydraulic Fracture Height Growth in Laminated Shale Reservoirs Using Finite–Discrete Element Method" by Li, H., Zou, Y., Liu, S. and Valko, P.P. Paper ARMA 2017-0556 presented at the 51st U.S. Rock Mechanics/Geomechanics Symposium, San Francisco, California, USA. 25-28 June. Copyright 2017 by the American Rock Mechanics Association.

[*] Part of this section is reprinted with permission from "Hydraulic Fracture Height Predictions in Laminated Shale Formations Using Finite Element Discrete Element Method" by Li, H., Zou, Y., Valko, P.P. and Ehlig-Economides, C.A. Paper SPE 179129 presented at the SPE Hydraulic Fracturing Technology Conference, The Woodlands, Texas, USA. 9-11 February. Copyright 2016 by the Society of Petroleum Engineers.

al. 2012; Wu 2014; Guo et al. 2015). Thiercelin et al. (1987) defined four types of modes for HF propagation towards a BP (**Fig. 44**). These four modes are: penetration, diversion, offset and arrest. Some researchers have conducted experimental hydraulic fracturing tests which show the effect of BPs on complex fracture propagation (Suarez–Rivera et al. 2013; Zou et al. 2016). Three factors of the BP play important role when a propagating HF approaches it: the strength of the BPs, the dipping angle of the BP and the principal stress difference (Abbs and Needham 1985). Many authors have stated that without considering the effect of BPs, models may overestimate the fracture height which will lead to less than optimal pumping schedules (Daneshy 2009; Chuprakov et al. 2015). Results in this section provide unique insights on how shale rock properties can alter the evolving fracture patterns during the hydraulic fracturing field treatment.

Sample number	Sampling direction referenced by BP direction	Young's modulus (GPa)	Poisson's ratio	Compression strength (MPa)
Y1	Parallel	15.75	0.147	145.39
Y2	Parallel	22.88	0.163	198.54
Y3	Parallel	15.79	0.167	171.26
Y4	Parallel	16.53	0.219	162.84
Y5	Perpendicular	13.19	0.217	175.06
Y6	Perpendicular	12.65	0.195	142.78

Table 11-Tri–axial loading test results of shale samples from Sichuan basin in China (Zou 2015).

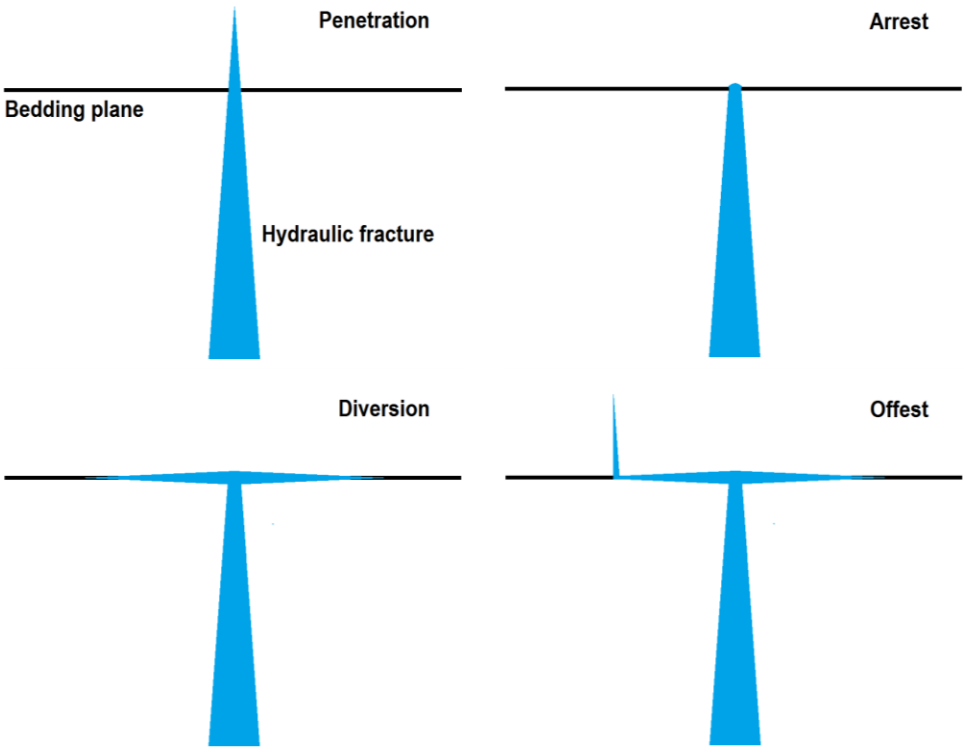

Fig. 44-Four types of HF–BP intersection modes (Thiercelin et al. 1987).

6.2 Single hydraulic fracture propagation in laminated reservoirs

6.2.1 Simulation procedure

Table 12 and **13** give the basic input parameters. The following results were obtained using the shown parameters, possibly changing only one of them at a time. The size of 2D domain is 200 m×200 m, and the horizontal wellbore starts from (0,100) m and ends at (200,100) m. There is one perforation cluster which is located at (100,100) m. We assumed that one cluster can initiate only one hydraulic fracture.

Properties	Value
Injection rate $(\boldsymbol{q})$	0.05 m^3/s
Vertical Stress $(\boldsymbol{\sigma_v})$	45.4 MPa
Minimum horizontal stress$(\boldsymbol{\sigma_h})$	40.9 MPa
Young's modulus $(\boldsymbol{E})$	4.0×10^{10} Pa
Poisson's ratio$(\boldsymbol{v})$	0.21
Fluid viscosity $(\boldsymbol{\mu})$	0.003 Pa.s
Fluid Specific Gravity	1.0
Simulation Domain Size	200 m×200 m

Table 12-Input data for simulations.

Properties	Rock Matrix	BP
BP spacing	20.0 m	
Tensile Strength	3.0×10^6 Pa	3.0×10^5 Pa
Cohesion	5.0×10^6 Pa	1.0×10^6 Pa
Friction Angle	30.0°	
Dilation Angle	20.0°	
Permeability	$10^{-6}\mu m^2$	$10^{-3}\mu m^2$

Table 13-Parameters of rock matrix and BPs.

The mechanical anisotropy factor K_0, introduced by Amadei (1983), is used to characterize the degree of mechanical anisotropy of the formation. For shale formations, we consider the transversely isotropic case, for which the factor is defined as:

$$K_0 = \frac{E_h}{E_v} \times \frac{V_v}{(1 - V_h)} \quad (6.1)$$

When $\boldsymbol{K_0}$ is large, the shale formation exhibits large degree of mechanical anisotropy. For comparison purposes, we studied six different mechanical cases:

1. Mechanical Isotropic Scenario, when the Young's modulus and Poisson's ratio are independent of directions.
2. Mechanical Anisotropic Scenario 1 (Anisotropic $\boldsymbol{E}$). Here, $E_h = 1.25 \times E_v$ and Poisson's ratio is independent of directions.
3. Mechanical Anisotropic Scenario 2 (Anisotropic $\boldsymbol{v}$). Here, $v_h = 1.2 \times Ev_v$ and Young's modulus is independent of directions.
4. Mechanical Anisotropic Scenario 3 (Anisotropic $\boldsymbol{E}$). Here, $E_h = 1.5 \times E_v$ and Poisson's ratio is independent of directions.
5. Mechanical Anisotropic Scenario 4 (Anisotropic $\boldsymbol{v}$). Here, $v_h = 1.4 \times Ev_v$ and Young's modulus is independent of directions.
6. Mechanical Anisotropic Scenario 5 (Anisotropic $\boldsymbol{E}$, $\boldsymbol{v}$). Here, $E_h = 1.5 \times E_v$ and $v_h = 1.4 \times v_v$. For all cases, we set $E_v = E$ and $v_v = v$.

Because of the limitations of the 2D model for fracture height study, we focus on the various mechanisms of fracture height evolution, affected by interaction between HFs

and BPs. In other words, we investigate how BP properties influence the evolution of the fracture height.

6.2.2 Simulation results and discussion

We changed only the mechanical properties of the domain and kept all other parameters unchanged. **Fig. 45** shows the fracture height evolution maps at a given injection time for the three cases. In the mechanical isotropic case, fractures tend to propagate crossing the BPs, and BPs are rarely opened. Even if a BP is opened, the corresponding open part is short. Locally, at the HF–BP intersection point, fluid pressure can relatively easily overcome the tensile strength of the rock matrix. Typically, the normal stress exerted on the BP is larger than the normal stress on the main hydraulic fracture (without considering stress shadow effect). For the cases of mechanical anisotropy with $E_h > E_v$, fluid can easily infiltrate the BP interfaces (due to the low Young's modulus in the vertical direction). After the initiation of the fracture along the BP interfaces, larger fracture width is created for formations with smaller E_v which leads to the fluid penetrating into the BP interfaces smoothly. Since more fluid flows into the broken BP interfaces, fracture height is confined, and the opened BP length becomes longer with the increase of mechanical anisotropy. The fracture tip induces a tensile stress that overcomes the rock strength of the intact rock (Zhang et al. 2007). Higher far–field stress (σ_H) and medium tensile and shear strength of BP interfaces result in the need for high fluid pressure to cause fluid leak–off into the BP interfaces. Similarly, with the increase of the anisotropy of Poisson's ratio, fractures tend to propagate along BPs instead of passing them.

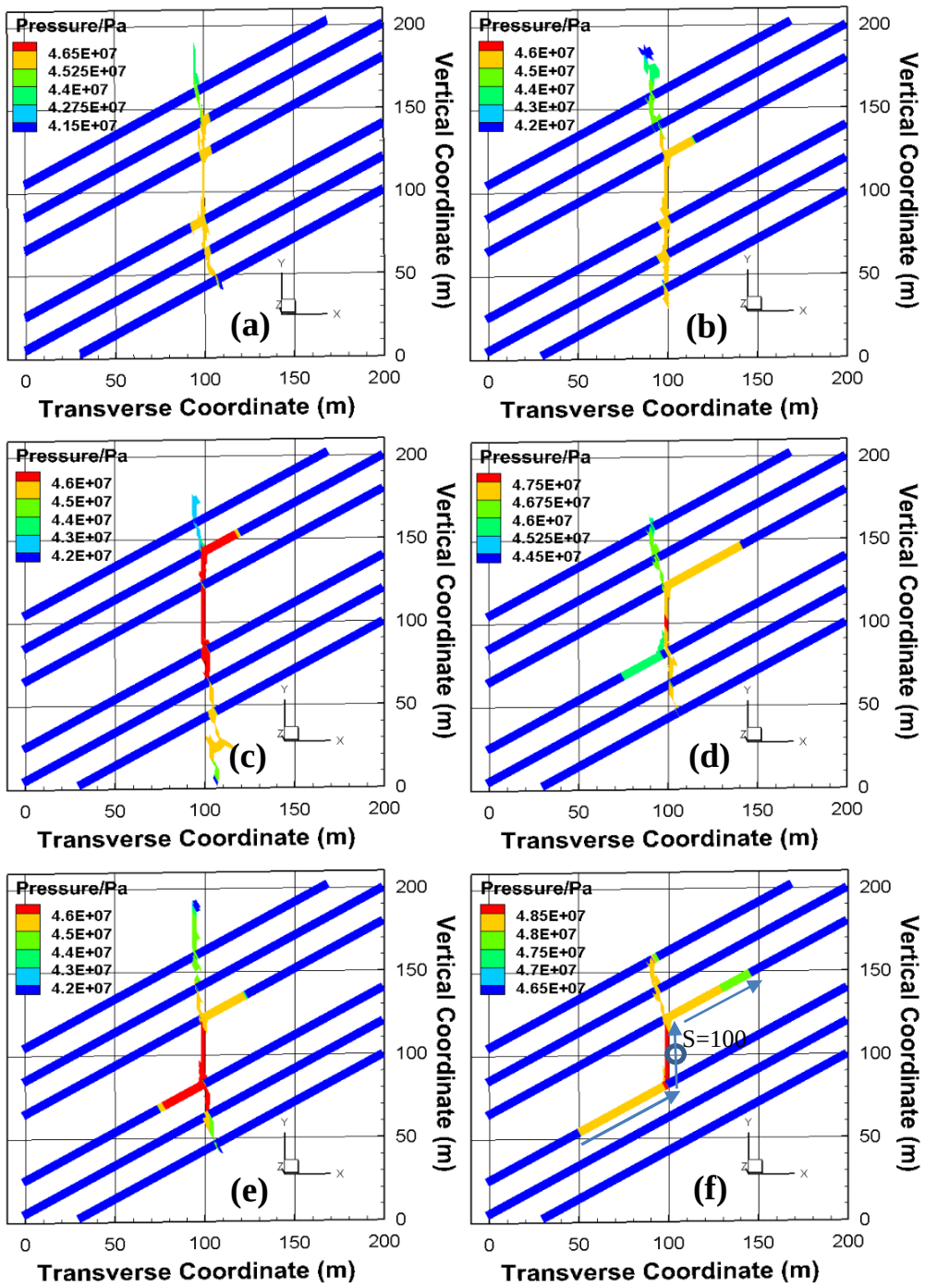

Fig. 45-2D simulation results for fracture height patterns for six different cases with 30° BP dip. (a). Mechanical isotropic scenario; (b). Mechanical anisotropic scenario 1; (c) Mechanical anisotropic scenario 2; (d). Mechanical anisotropic scenario 3; (e). Mechanical anisotropic scenario 4; (f). Mechanical anisotropic scenario 5.

Despite the deflection of the fracture into BP interfaces, fracture bifurcation was induced subsequently on the other side of BP interfaces, in the intact rock matrix (**Fig. 45**). The direction of fracture bifurcations happening at the intact side of the BP interface is nearly vertical. The small deviation from vertical is caused by the stress shadow effect originating from the fluid pressure within the opened BP interfaces. The deviation from the vertical is larger for the case with a longer opened BP interface. This observation is supported by **Figs. 45(b)** and **45(c)**.

We also plotted the fluid pressure distributions (P) and fracture width distributions (w) versus the position along the main fracture (S). In **Fig. 45(f)** the arrow denotes the trace of the main fracture which is in the direction of the x axis of the plot in **Fig. 46**. For all cases the pressure and width distributions are shown at the same injection time. The S value of the center of perforation is set to be 100 m for all cases. **Fig. 46** shows pressure distributions of isotropic scenario, mechanical anisotropy scenario 3 and mechanical anisotropy scenario 5 which can represent the trend of pressure of all scenarios based on our research. As clearly shown in **Fig. 46**, with increase of mechanical anisotropy factor, the fluid pressure within the fracture is increasing. Larger Young's modulus leads to smaller fracture width under the same circumstances. As a result, fluid can penetrate to the fracture slowly, and more time is needed for pressure accumulation before triggering rock failure. This fact also can be observed in the pressure and width distribution plots. In mechanical anisotropic formations, the pressure distribution within the fracture is apparently higher than in the mechanical isotropic formation, but the fracture width does not vary so much for different cases. For mechanical isotropic cases, there is a significant

pressure drop in the S value range from 135 m to 145 m. This is caused by several reasons. The fracture crosses the BP interfaces at around 138 m which results in a large pressure drop before and after crossing. The intact BP interfaces can behave as a fluid leak–off channel (in the case of large permeability–thickness product). Moreover, because of the complexity of stress distribution around the crossing point, sometimes multi–stranded fractures are generated in this zone. This is also one of the reasons resulting in the large pressure drop.

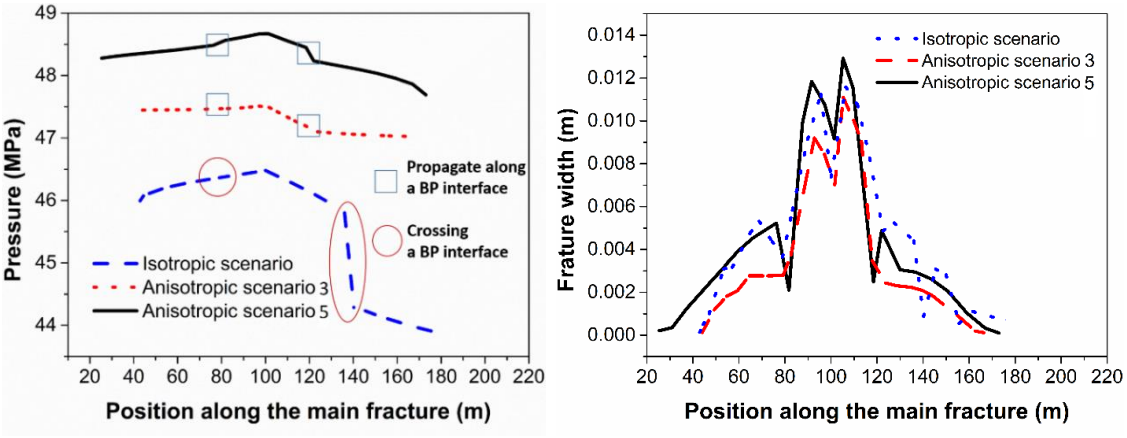

Fig. 46-Fluid pressure within the main fracture and fracture width distributions for different mechanical cases.

We also studied the effect of BP dip angles on fracture height evolution. We conducted simulations for four cases with different BP dip and mechanical isotropy formations. Considering only far–field stresses, with the increase of the BP dip, the normal stress for BP interfaces becomes smaller because of the common supposition that

minimum horizontal stress is smaller than vertical stress. With the increasing BP dip, shear sliding and tensile failure occur more frequently, due to the decrease of normal stress exerted on the BP interface **(Fig. 47)**.

For the case of 30° BP dip, step–over fractures developed during the fluid injection (offset occurred at several BPs). This fracture pattern resulted from the interaction between local stress shadow effect, far–field stress difference, BP dip angles and tensile and shear strength difference (Cooke et al. 2001). In fact, step–over fractures occur if the values of all these factors are in a specific range. For instance, Cooke et al. (2001) found that if the tensile strength of BP interfaces is too small compared with intact matrix rock, the fracture tends to propagate along the BP interface instead of reinitiating new fracture branches. On the other hand, when the tensile stress of BP interface is large, fractures tend to cross the BP interface instead of opening it. Likewise, BP dipping angles should fall into a specific range to cause step–over fractures. Since the fracture propagating along the vertical direction is subjected to minimum horizontal stress, and the fracture propagating along BP is subjected to the stress between minimum horizontal stress and vertical stress (without considering stress shadow effect here), offset situation can happen in such a way that the width of the fracture diverting into the matrix rocks may be larger than the fracture width inside the BP interface.

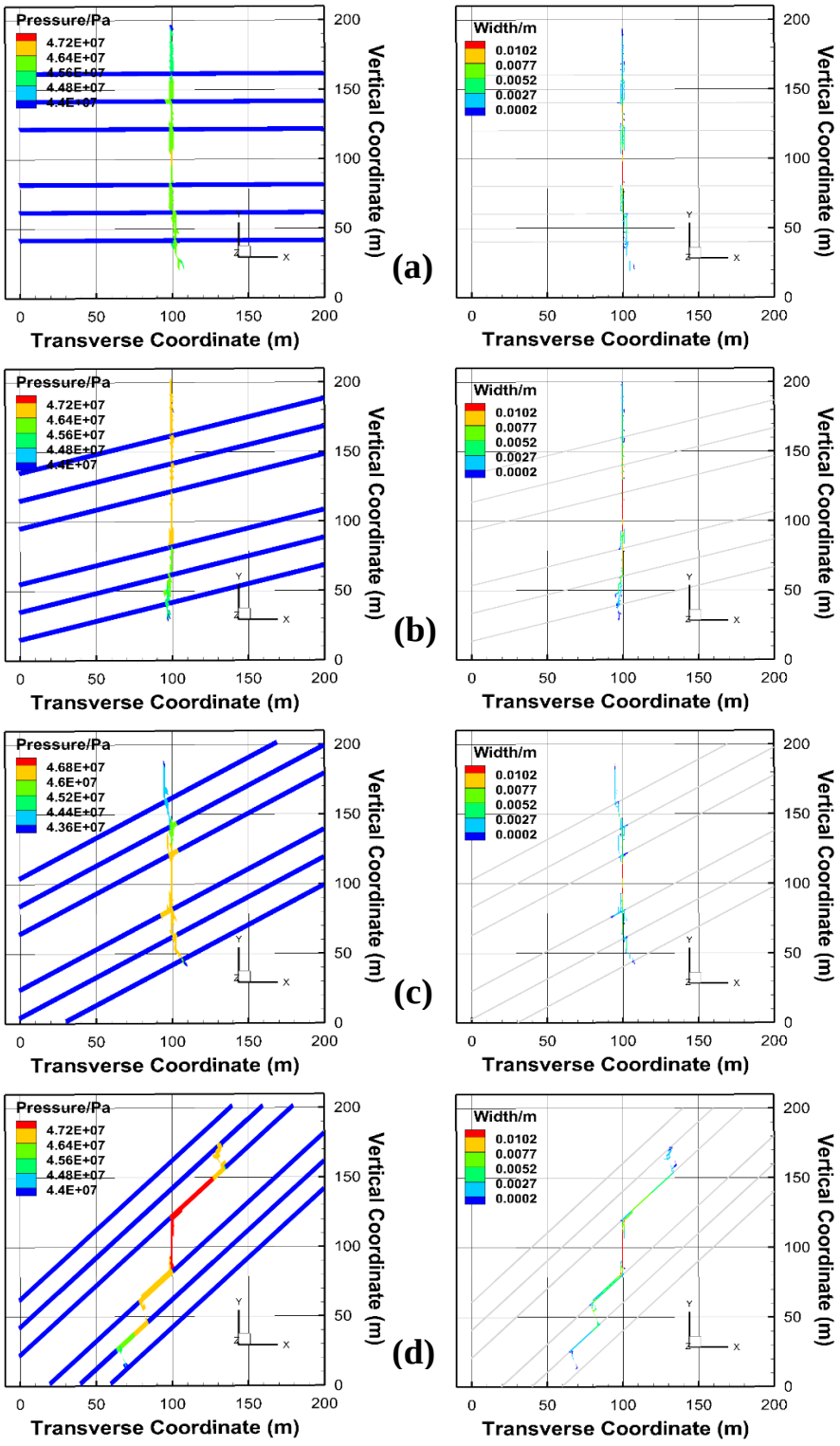

Fig. 47-2D simulation results for fracture height patterns for four cases. They are: (a). BP dip is 0°; (b). BP dip is 15°; (c). BP dip is 30°; (d). BP dip is 45°.

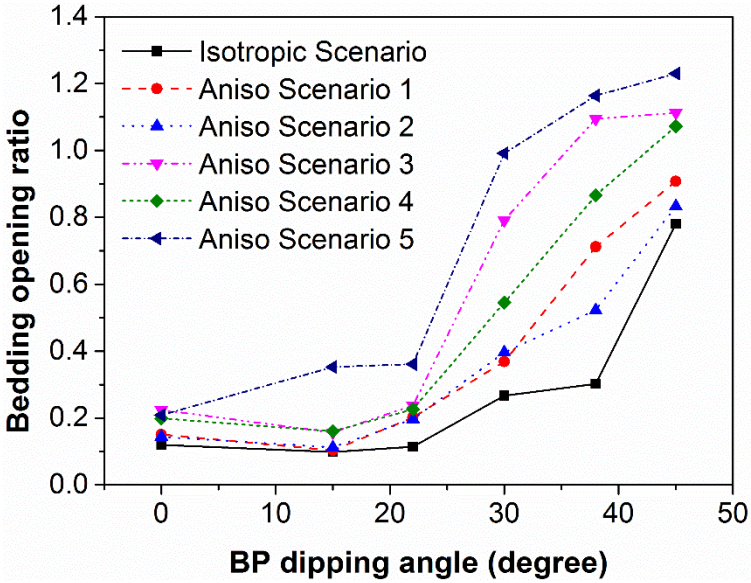

Fig. 48-Plot for BP opening ratio for different formation mechanical properties and BP dips.

Fig. 48 illustrates the fracture height confinement for various mechanical cases. Here, the BP opening ratio is defined as:

$$BP\ opening\ ratio = \frac{\text{BP opening length}}{\text{fracture height}} \quad (6.2)$$

The plot clearly shows that, with increasing BP dip and mechanical anisotropy factor, hydraulic fractures tend to propagate along BP interfaces, and fracture height is more confined. However, when the BP dip is small (< 22°), it has little effect on fracture height.

We assessed the stimulated reservoir area (SRA) for all cases. We investigated fracture height evolution in 2D scenarios. We chose to define Stimulated Reservoir Area (SRA) by outlining the fractured area based on our simulation results. The fracture pattern

with longer fracture length and fewer highly clustered fractures can result in large SRA. **Fig. 49** summarizes SRA for all cases.

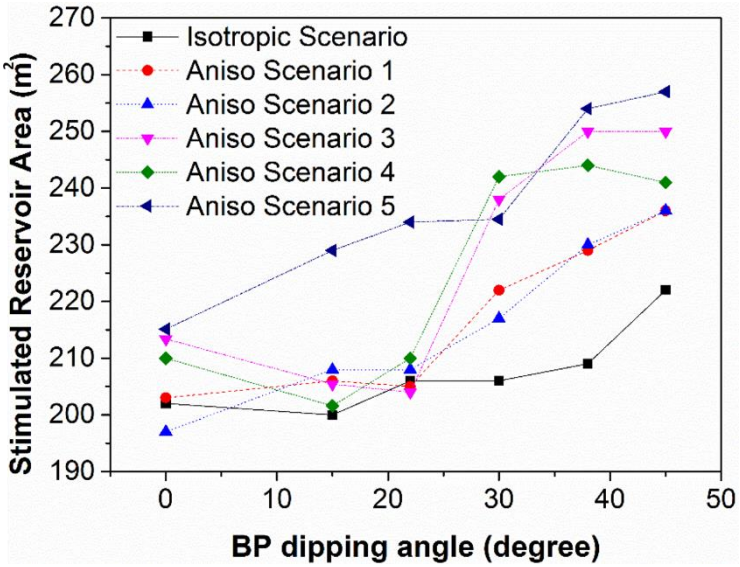

Fig. 49-Plot for reservoir stimulated area for different formation mechanical properties and BP dips.

With the increase of mechanical anisotropy factor, the SRA increases. This observation is obvious for cases with bedding plane dipping angle >22°. To be more specific, the SRA related to opening bedding planes becomes larger when the degree of mechanical anisotropy increases. Since the normal stress for BP interfaces is larger than the normal stress for main fractures, fracture width of opening BPs decreases. On the other hand, for the case that HFs propagate through BP interfaces instead of opening it, fractures

can intersect more BP interfaces which can act as high–permeability leak–off tunnel since fracture height is less confined.

Observed (or calculated) bottom–hole net pressure versus injection time curves are used routinely for monitoring the HF treatment. Such a curve retrieved from the simulation runs (**Fig. 50)**, corresponds to the case with one perforation cluster, mechanical anisotropy (Scenario 2) and BP dip of 30°. By analyzing both the fracture evolution maps and the pressure plot, we distinguished three stages during the injection:

- Stage 1, fractures propagate in the rock matrix, only;
- Stage 2, fractures propagate both in rock matrix and along BP interfaces;
- Stage 3, fractures propagate only along BP interfaces.

In stage 1, the treating pressure increases sharply; afterwards comparatively large pressure drops may occur, as seen in the red circle. Despite the observed individual sharp pressure drops indicating extensive fracture propagation, the rock failure in macroscopic scale is triggered by a continuous accumulation and nucleation of point defects and dislocations, which are in mesoscale and nanoscale in rock materials (Rollett et al. 2004). Since the matrix permeability is ultra–low, the leak–off rate in stage 1 is almost negligible.

At the start of stage 2, the fracture tip touches a BP interface, and fluid infiltrates into the BP. Pressure accumulation is slowing down due to this secondary leak–off. Once the fracture starts to propagate along a BP interface, a small pressure drop occurs in the pressure plot.

In stage 3, most fractures propagate along BP interfaces, and the pressure fluctuations are dumped. In this stage, the injected fluid is mostly used up by the large

overall fluid leak–off rate, and fracture propagation slows, eventually terminating totally. While analyzing simulation results and the bottom–hole pressure curve simultaneously provides a deep insight, it is also clear that the net pressure curve itself contains less detectable features at larger injection times. Simply put, the classical Nolte–Smith interpretation becomes more difficult with more anisotropy, larger dip angles and longer injection times.

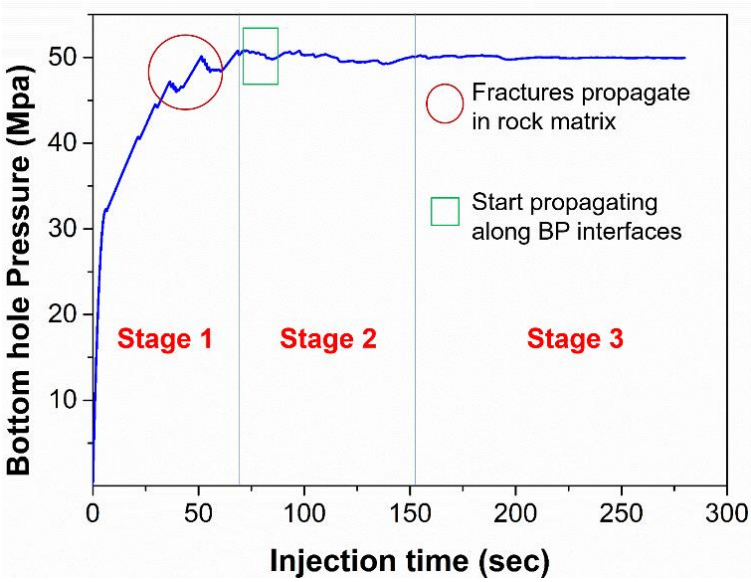

Fig. 50-Plot for bottom–hole pressure versus injection time.

6.3 Multi−fracture propagation in laminated reservoirs

6.3.1 Simulation setup

Table 14 gives the basic input parameters for simulation cases of simultaneous multiple hydraulic fractures interacting with BPs. In each case, the BPs have the same properties, including BP length, orientation, mechanical properties and initial permeability. If the values of input parameters differ from those in **Table 14,** we give those values.

Matrix parameters		**Bedding plane parameters**	
Permeability ($\times 10^{-3}$ μm^2)	0.001	Permeability ($\times 10^{-3}$ μm^2)	1
Minimum horizontal stress (MPa)	35	Tensile strength (MPa)	1
Maximum horizontal stress (MPa)	37	Cohesion (MPa)	2
Young's modulus (GPa)	40.0	Friction angle (°)	30.0
Poisson's ratio	0.21	**Treatment parameters**	
Tensile strength (MPa)	2.0	Injection rate (m^3/s)	0.24
Cohesion (MPa)	6.0	Fluid viscosity (Pa·s)	0.003
Friction angle (°)	30.0	Perforation cluster spacing (m)	10

Table 14-Input parameters for simultaneous multiple hydraulic fractures interacting with BPs.

The size of the 2D domain is 150 m by 300 m, and the horizontal well starts from (0,150) m and ends at (150,150) m (**Fig. 51**). There are four perforation cluster in the simulation domain. Several BPs with same spacing are in the simulation domain. We assumed that one cluster can initiate only one fracture.

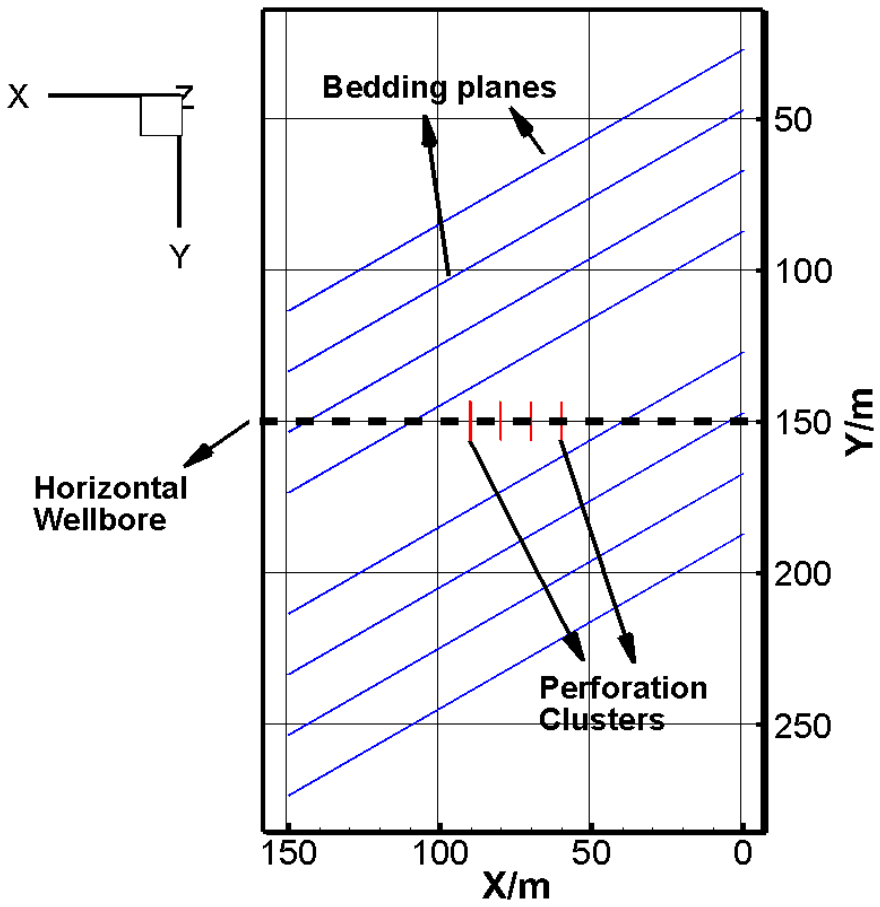

Fig. 51-Schematic of 2D simulation domain with BPs and four perforation clusters.

6.3.2 Results and discussion

We studied the effect of fluid viscosity on simultaneous multiple hydraulic fractures interacting with BPs. Greater fluid viscosity resulted in more uniform, shorter, and wider fractures **(Fig. 52)**. For the case with very great fluid viscosity (0.3 Pa.s), fluid pressure at the near–wellbore area was extremely high with fractures propagation, and longitudinal fractures may be generated, since the fluid pressure may exceed the maximum horizontal stress. Though smaller fractured area was generated in the case with larger fluid viscosity, the fracture width was comparatively large, so that the fractures could accept larger proppant. **Fig. 53** shows the fracture width distribution for different cases. However, for the case with lesser fluid viscosity, a substantial pressure and width drop occurred at the point where fracture began propagating along BPs. This location can act as a narrow throat which can block proppant transport. This suggests that increasing fluid viscosity in some cases may result in larger propped fracture volume than the case using slick water for simultaneous multiple hydraulic fractures interacting with BPs.

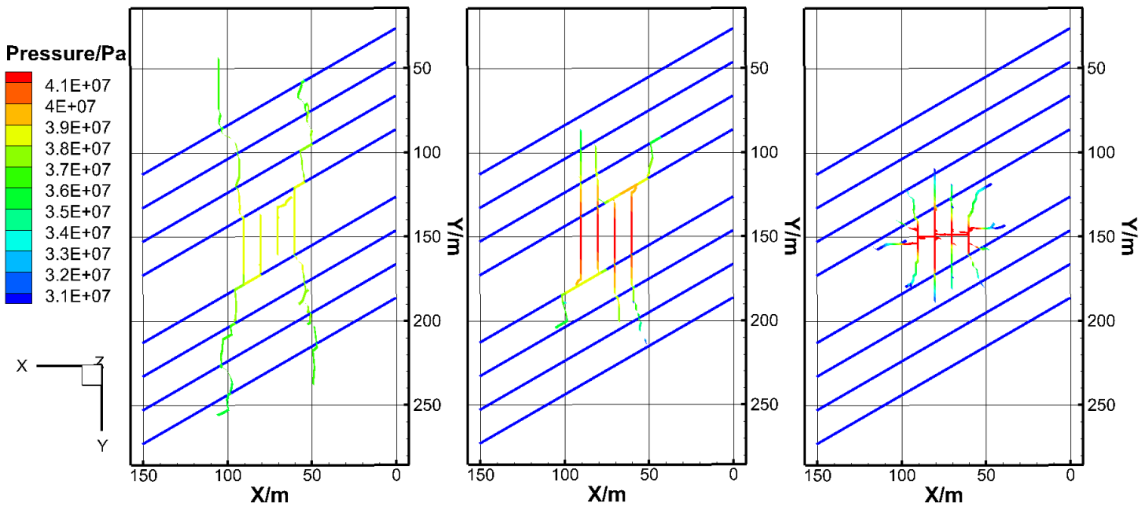

Fig. 52-2D simulation results of simultaneous multiple hydraulic fractures interacting with BPs. Left: Fluid viscosity= 0.003 Pa.s; Middle: Fluid viscosity= 0.03 Pa.s; Right: Fluid viscosity= 0.3 Pa.s.

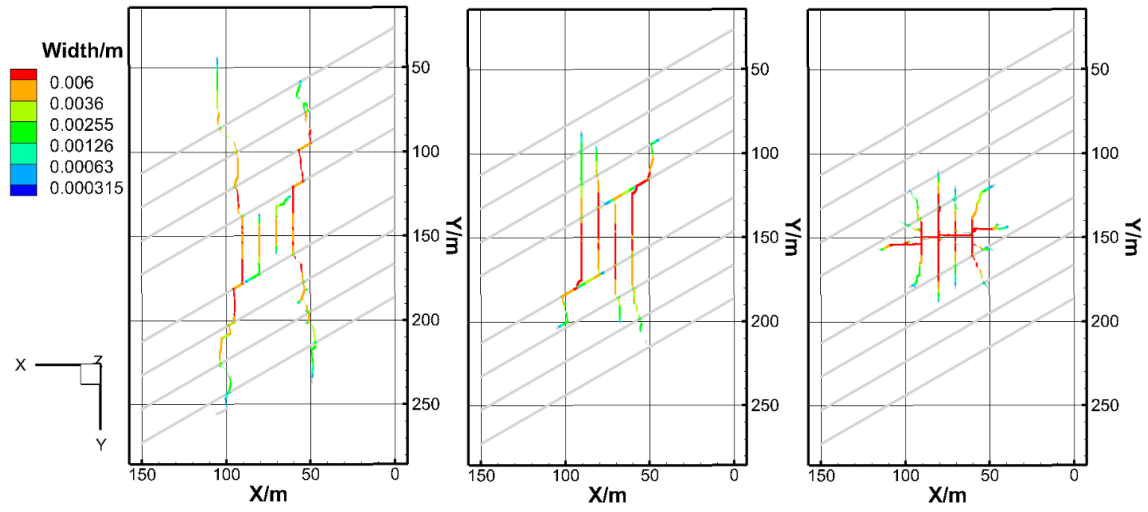

Fig. 53-2D simulation results with fracture width distributions of simultaneous multiple hydraulic fractures interacting with BPs. Left: Fluid viscosity= 0.003 Pa.s; Middle: Fluid viscosity= 0.03 Pa.s; Right: Fluid viscosity= 0.3 Pa.s.

We also investigated the effect of mechanical anisotropy on simultaneous multiple hydraulic fractures interacting with BPs. In the mechanical isotropic case, fractures tend to propagate crossing the BPs, and BPs are rarely opened (**Fig. 54**). For the cases of mechanical anisotropy, fracture height is confined, and the opened BP length increases with the increase of mechanical anisotropy. This observation is in accordance with the results from Li et al. (2016b). Moreover, due to the strong stress shadowing effect, the two inner fractures have higher fluid pressure, shorter height and less fractured reservoir area; the two outer fractures tend to propagate along BPs.

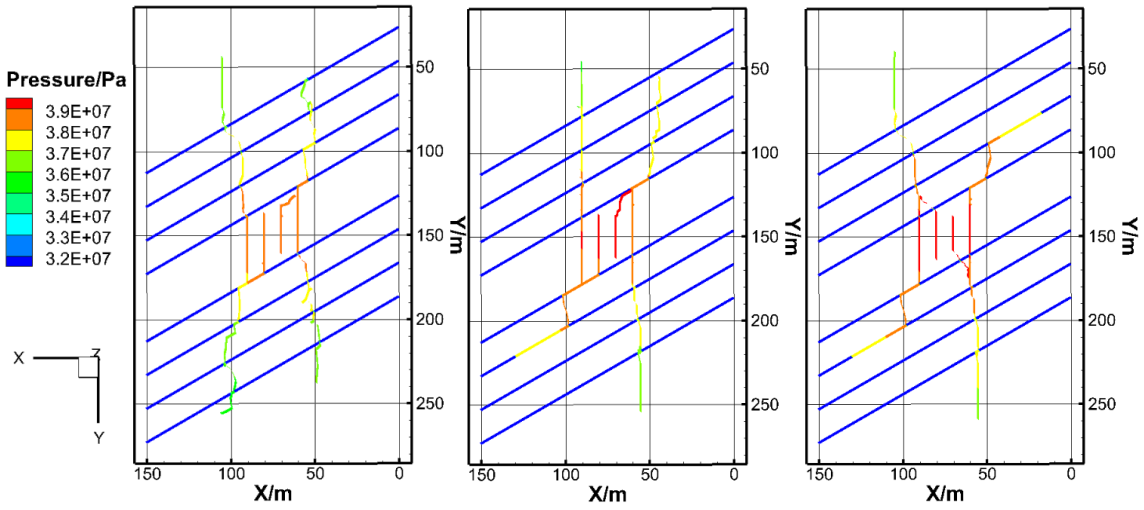

Fig. 54-2D simulation results for fracture height patterns for cases with different mechanical properties. Left: Mechanical isotropic scenario ($E_h=E_v$, $V_h=V_v$); Middle: Mechanical anisotropic scenario ($E_h=1.2E_v$, $V_h=0.9V_v$); Right: Mechanical anisotropic scenario 2 ($E_h=1.5E_v$, $V_h=0.8V_v$).

Simulations with different fluid injection rates were conducted. **Fig. 55** shows fracture height patterns with different pumping rates. With the increase of fluid injection rate, fractures tend to propagate along BPs instead of crossing them. For the same injected fluid volume, less treatment time is needed with larger pumping rate, which results in less leak–off during pumping. So large fluid pressures in two interior fractures induces larger local stress around the two exterior fractures, which makes propagation along BPs become preferable.

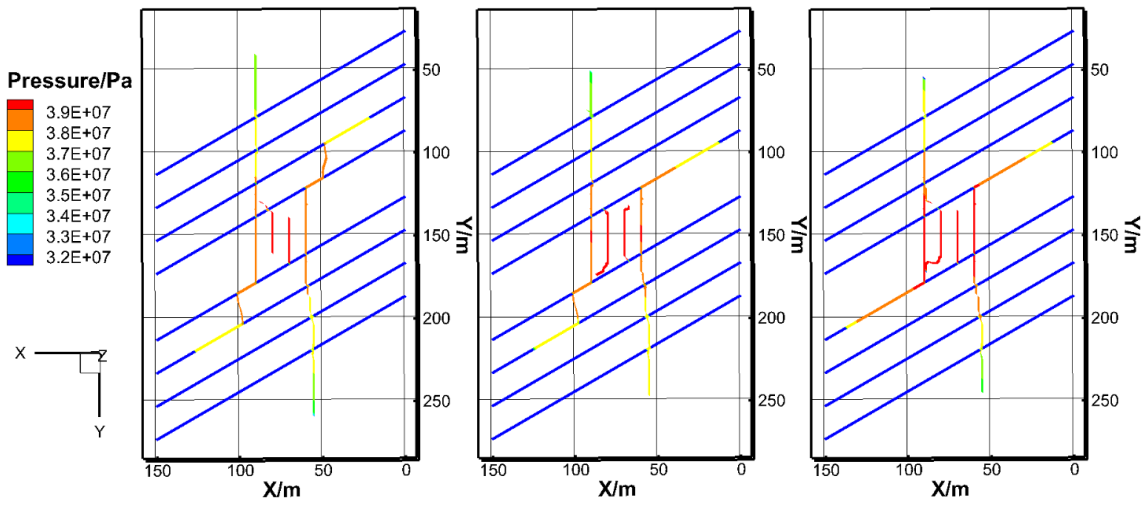

Fig. 55-2D simulation results for fracture height patterns for cases with different fluid injection rates. Left: injection rate= 0.12 m^3/s; Middle: injection rate= 0.18 m^3/s; Right: injection rate= 0.24 m^3/s.

6.4 Novel fracturing treatment designs for laminated reservoirs development

Alternating fracturing (Texas two–step) method has been proposed in recent years for optimizing hydraulic fracturing design. For this technique, the first and second stages of fractures are created at first, and a third stage is placed between the previous two (Rafiee et al. 2012). This approach was proposed to generate complex network of fractures by altering stress distribution in the formation. However, this approach is still hard to apply in fracturing operations, due to many operational issues (Rafiee et al. 2012), and applying this approach to naturally fractured, laminated reservoirs to increase fracture complexity is still questionable. For hydraulic fracturing treatment in laminated reservoirs, we purposed a novel sequential fracturing approach to maximize SRV. The simulation results are compared with those from Texas two–step technique.

Table 15 gives the summary of simulation results for sequential fracturing and alternating fracturing. The injection volume in each fracture cluster is the same for all cases. That is, the total injection volume for the case with nine fracture clusters is 1.5 times of the fluid volume with six fracture clusters. By comparison, average fractured area per fracture cluster with sequential fracturing is larger than the area with alternating fracturing. Moreover, as can be seen in **Fig. 56**, severe near wellbore tortuosity occurs in cases with alternating fracturing. Since fracturing fluid can be diverted to BPs with relatively high permeability, induced stress from BPs can change the local stress distribution of the potential fracture paths of the next stage.

	Sequential fracturing		**Texas two–step**	
Total number of fracture clusters	9	6	9	6
Total fractured area (m^2)	1122.7	731.7	1044.3	701.5
Average fractured area per fracture cluster	124.7	121.9	116.0	116.9
Near wellbore tortuosity	2	0	3	1
Injection time (s)	96	96	96	96

Table 15-Comparison of sequential fracturing and alternating fracturing.

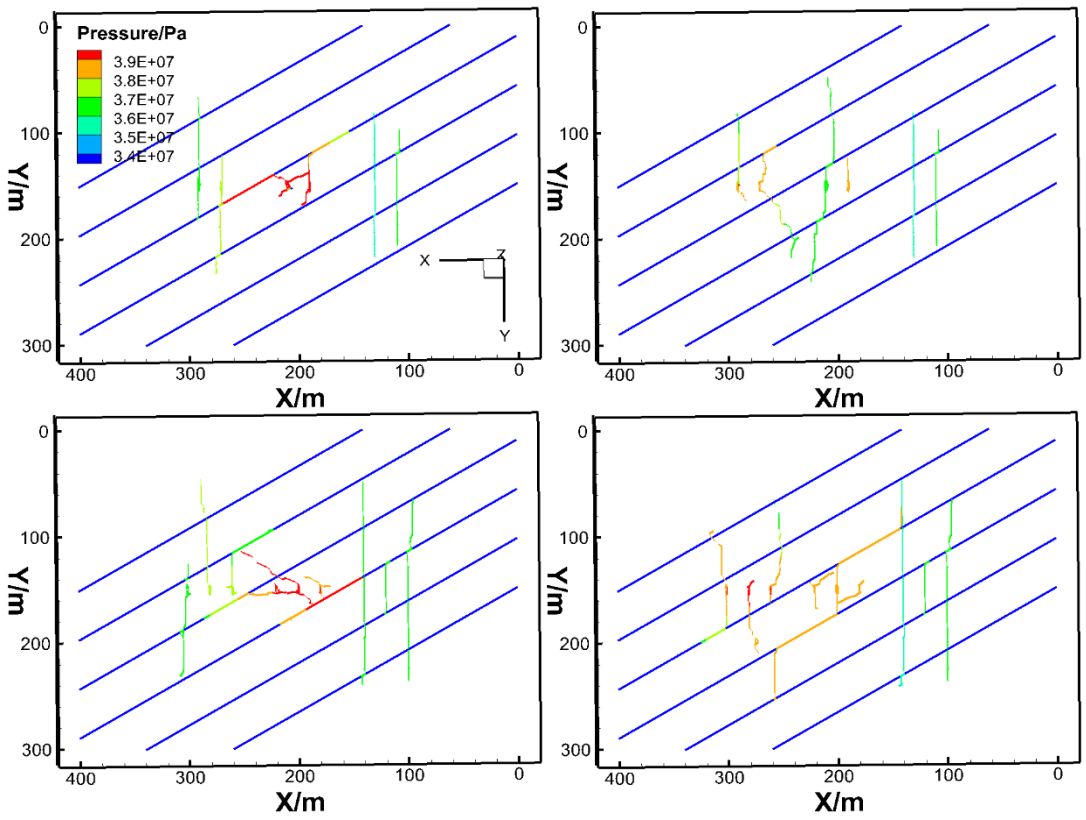

Fig. 56-Predicted fracture network maps for cases with different hydraulic fracturing treatment approaches. Left: Alternating fracturing; Right: Sequential fracturing.

The evolution of complex fracture geometry is demonstrated by the stress distribution contour maps. Contour plots in **Fig. 57** give the stress distribution σ_{xx} and σ_{yy} at the start of pumping the middle stage (that is stage 2 for sequential fracturing and stage 3 for alternating fracturing.) For the case of sequential fracturing, the magnitude of σ_{xx} around the center point of the simulation domain is almost equal to σ_{yy}. Complex fracture geometry can be generated due to the local isotropic stress state. On the other hand, around the same point the magnitude of σ_{yy} is significantly higher than σ_{xx} for the

alternating fracturing case, potentially causing the initiation of longitudinal fractures. For the geological scenario where the minimum principal stress is perpendicular to wellbore trajectory, the initiation of horizontal fractures will lead to fracture kinking in the near–wellbore region (Li et al. 2016a). Fracture kinking is disadvantageous; it can block the pathway of proppant and can lead to early screen–out. In the geological scenario with high density of BPs, another potential risk is that fractures propagating along BPs can connect with the ones originating from neighboring clusters. Under such circumstances some perforation clusters will be ineffective during production. In conclusion, our results suggest that for formations with high BP density and low initial stress anisotropy, alternating fracturing should be avoided.

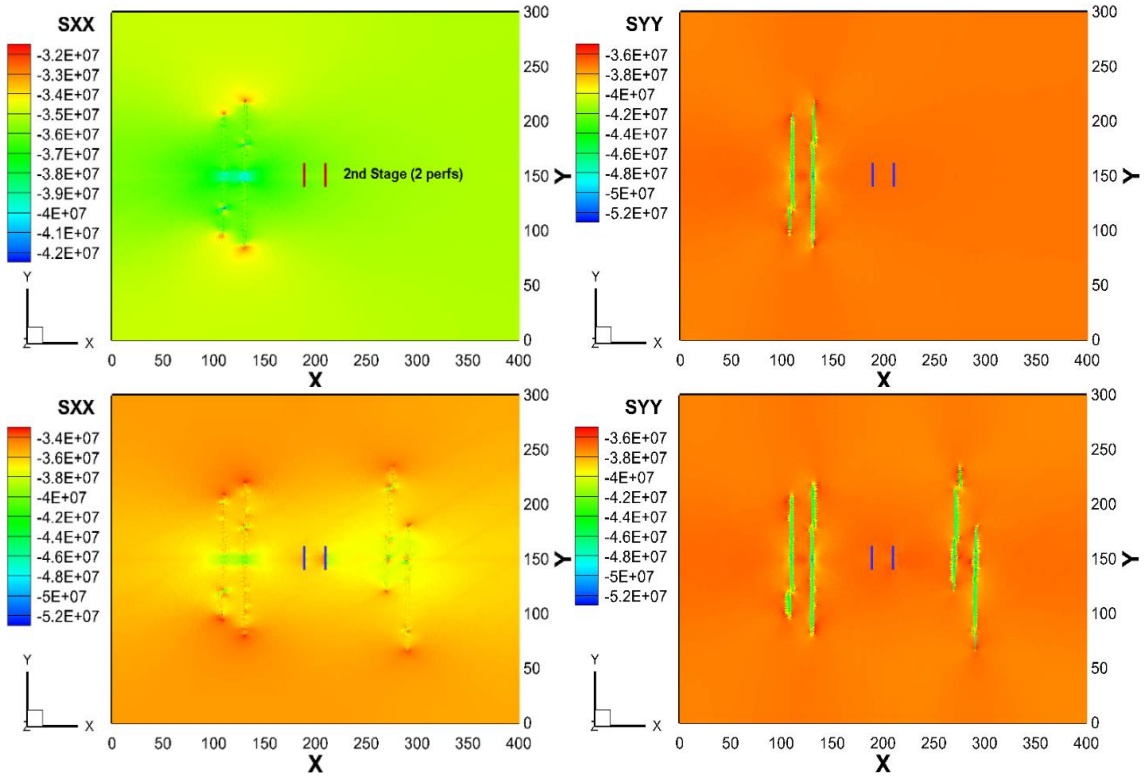

Fig. 57-2D contour plots of stress distribution for cases with different hydraulic fracturing treatment approaches. Top: Sequential fracturing; Bottom: Alternating fracturing.

The previous comparison of sequential and alternating fracturing already implies that a well–designed sequential fracturing approach should consider both the instantaneous (direct) and future (indirect) consequences of any decision and optimize the treatment sequence. It is noted that since there are many geological properties involved, it is unpractical to find a specific fracturing design which is the optimal choice for all kinds of geological scenarios. Here we consider formations with large thickness and small ratio of vertical to minimum horizontal stress. The reason we focus on such formations is that

BPs will play a key role under such circumstances, and design can have a noticeable effect on the outcome.

The input parameters of simulations can be seen in **Table 16**. For simulations with sequential fracturing, three–stage fracturing treatments were conducted. Two wells are parallel with each other, and fracturing treatments for each stage of two wells were conducting simultaneously. The fluid injection volume is same for every stage. There are seven fracturing treatment designs with different number of fracture clusters in each stage. Case number of each design can be seen in **Table 17**. For example, for case five, there are two, one and two perforation clusters in stage one, two and three respectively in well #1, and there are one, two and one perforation clusters in stage one, two and three respectively in well #2. We assume that one perforation cluster can only initiate one fracture.

Matrix parameters		**Bedding plane parameters**	
Permeability ($\times 10^{-3}$ μm^2)	0.001	Permeability ($\times 10^{-3}$ μm^2)	1.0
Minimum horizontal stress (MPa)	35	Tensile Strength (MPa)	2.0
Vertical stress (MPa)	39	Cohesion (MPa)	2.0
Young's modulus (GPa)	40.0	Friction angle (°)	30.0
Poisson's ratio	0.21	**Treatment parameters**	
Tensile Strength (MPa)	2.0	Fluid viscosity (Pa·s)	0.003
Cohesion (MPa)	6.0	Injection volume of each stage (m^3)	7.2
Friction angle (°)	30.0	Well spacing (m)	200

Table 16-Summary of input parameters.

Fracturing treatment design	3-1-3 3-1-3	3-1-3 1-3-1	3-2-3 3-2-3	2-1-2 2-1-2	2-1-2 1-2-1	3-3-3 3-3-3	4-1-4 4-1-4
Case Number	1	2	3	4	5	6	7

Table 17-Case number for all sequential fracturing designs.

Summarization of simulation results can be seen in **Fig. 58**. X axis are the case number of fracture treatment designs. As can be seen in **Fig. 58(a)**, case one, four and seven always have larger fractured area compared with other cases. Interestingly, these three cases have similar designs: the number of perforation clusters for stage one and stage

three are same in both wells, and stage two only has one perforation cluster. For cases with more than one perforation cluster in stage two, local stress distribution around perforation clusters at stage two becomes very complex. Stress around perforation clusters at stage two during pumping becomes relatively high and stress distribution becomes near isotropic. This results in initiation of fracture kinking around the wellbore region, which is proved by **Fig. 58(b)**. Moreover, the complex stress distribution resulted from stage two can have strong effect on stage three, which is proved by the complex fracture geometry around perforation clusters at stage three. With the increase of fluid injection rate, total fractured area is increasing. Since BPs have comparatively high permeability, longer injection time can cause much fluid flow through BPs. Some of the observation can also be found in **Fig. 59**. It is noted that for cases with smaller total fractured area, many fracture kinking in near–wellbore region is observed. This should be avoided to maximize SRV and minimize the occurrence of tip screen out.

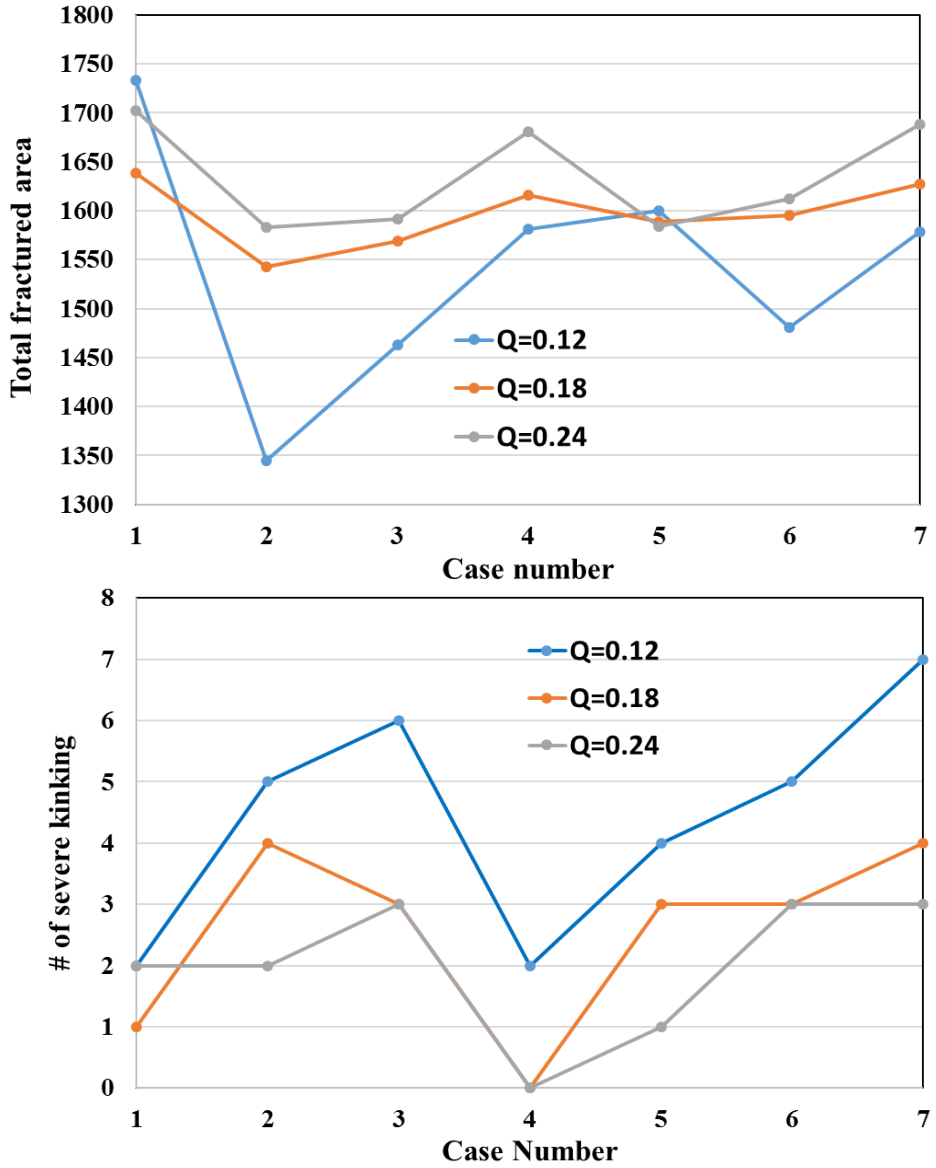

Fig. 58-Summary of fracturing quality of all designs. (a). Plot of total fractured area (m^2); (b) Plot for the number of severe kinking.

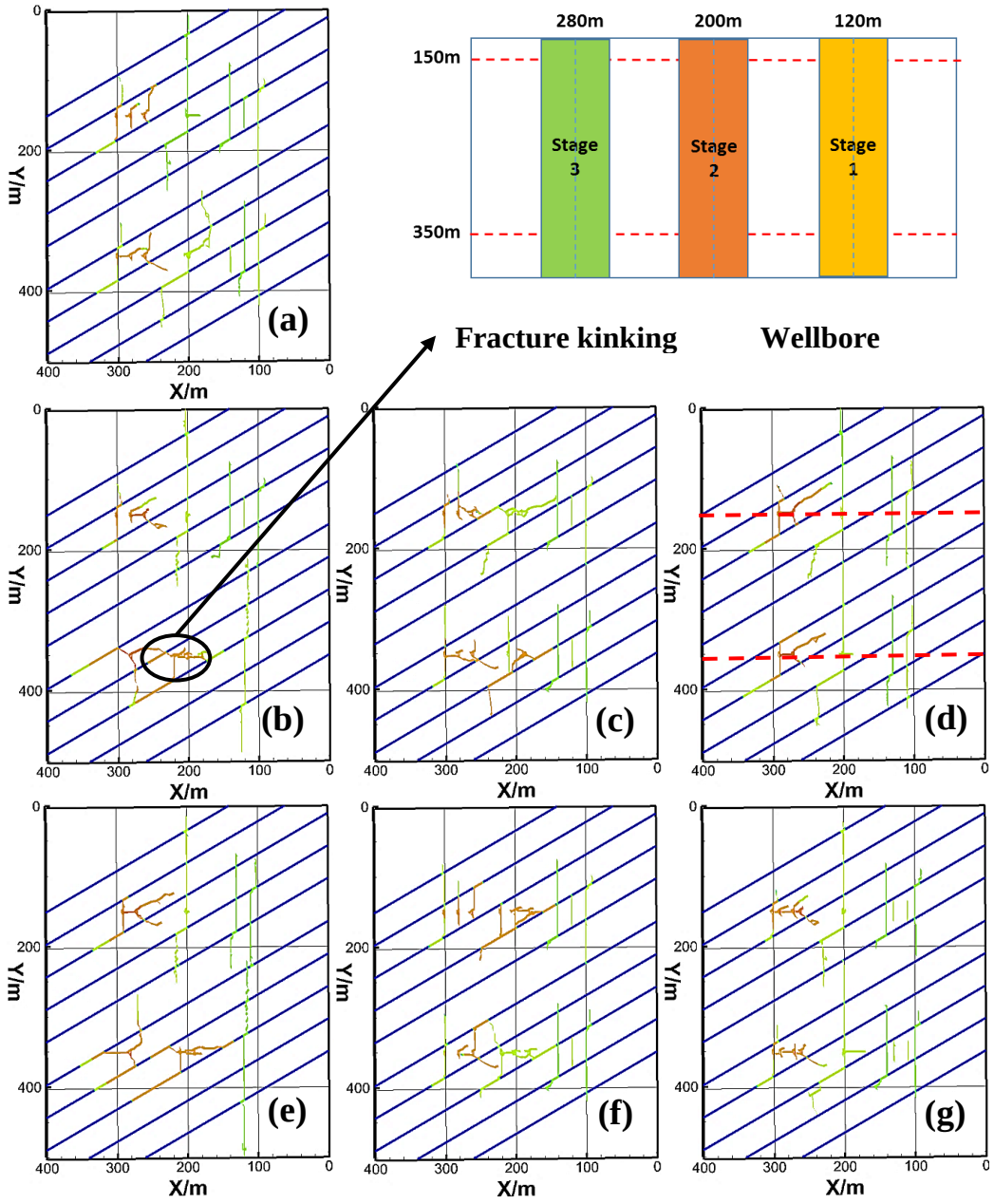

Fig. 59-2D simulation results of cases with injection rate= 0.12 m^3/s and different fracturing treatment designs. (a). Case 1; (b). Case 2; (c) Case 3: (d). Case 4; (e). Case 5; (f). Case 6; (g). Case 7.

We also have simulation results with fracture width distribution. **Fig. 60** shows predicted fracture maps for four selected cases. We select four cases for comparison of fracture width distribution. As can be seen in the Figure, fractures close to kinking always has comparatively small fracture width, and fracture width along a fracture which is close to around kinking is highly variable. This observation suggests that the stress distribution around fracture kinking is very large and complex. With the increase of the number of perforation clusters in one stage, the length of fracture with extremely small fracture width ($<3.15 \times 10^{-4}\ m$) become longer. Since 105 μm is the smallest diameter size of common proppant, we define the fractures whose width is smaller than $3.15 \times 10^{-4}\ m$ (three times of 105 μm) as unpropped fractures. We concluded that with the increase of the number of perforation clusters in one stage, the unpropped fracture length will becomes longer.

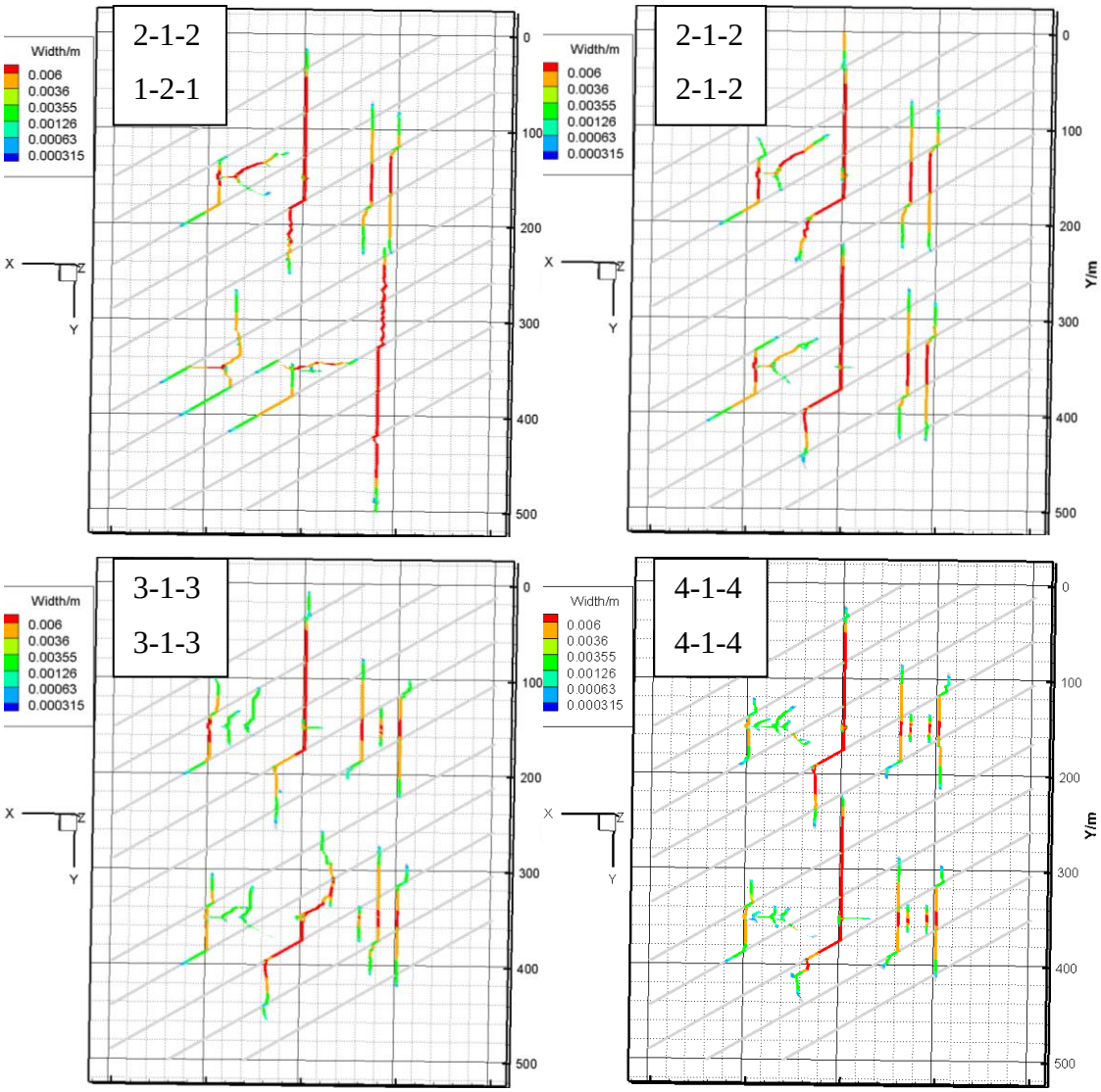

Fig. 60-2D simulation results for four cases (case 1, 4, 5 and 7) with fracture width distributions.

6.5 Conclusions

The module controlling HF–BP interaction is incorporated into the FDEM model to study the hydraulic fracture evolution for both mechanical isotropic and anisotropic formations in the presence of BPs. With the increase of mechanical anisotropy and BP dipping angle, HFs tend to propagate more along BP interfaces, and fracture height is more confined. Small BP dipping angle has negligible effect on fracture height. In case with mechanical anisotropy characterized by $E_h > E_v$, fluid can easily leak off into BP interfaces. HFs crossing the BP interfaces propagate not exactly in vertical direction, due to the stress shadowing effect originated by pressurized fluid within opened BP interfaces.

For the specific ranges of tensile and shear strengths, BP dipping angle and mechanical anisotropy factor, step–over fractures (offset geometry) can be generated. The classical Nolte–Smith interpretation of treating pressures becomes difficult for cases with increasing mechanical anisotropy, larger dipping angles and longer injection times.

Moreover, the investigation of simultaneous multiple HFs height growth, and the effect of BP properties, mechanical anisotropy and treatment properties on fracture height evolution in laminated reservoirs has been conducted. Novel multi–fracture, multi–stage hydraulic fracturing treatment designs have been proposed, which can be utilized to improve hydrocarbon production for laminated shale formations with large thickness and small vertical stress/minimum horizontal stress ratio. This section provides a framework for more realistic prediction of fracture height and fracture evolution in laminated shale formations for hydraulic fracturing treatment.

7. SUMMARY AND CONCLUSIONS

This dissertation presents a comprehensive numerical study on complex fracture network propagation in laminated, naturally fractured reservoirs. A novel coupled fluid flow and rock deformation numerical model based on finite–discrete element method was proposed to simulate complex fracture propagation in unconventional reservoirs. The following list summarizes the physical processes and theories employed in the model.

- The dynamic stress equilibrium equation was considered for rock deformation. The weak form of the governing equation was developed based on the principle of minimum potential energy, and it was solved by dynamic relaxation method.
- The fluid flow within fractures was governed by the lubrication equation. Materials balance and fluid leak–off correlations were incorporated in the model. Standard Galerkin Finite Element method was utilized to discretize the governing equation and develop the FEM model of the fluid flow equation.
- Mechanical interaction between two neighboring matrix elements was determined by the constitutive law. Neighboring matrix elements were connected by two virtual springs which are charged for stress and strain delivery.
- Mohr Coulomb criterion and maximum tensile stress criterion were utilized to predict rock failure in shear mode and tensile mode respectively.
- A BP module was developed and incorporated into the model. Mechanical anisotropy of rock materials was considered in the simulation. A NFs network

builder was developed based on the characterization and observation of NFs geological and mechanical properties.

- Picard iterative algorithm was used to solve the coupling of fluid flow and rock deformation.

Simulations were conducted to investigate single and multiple HFs propagation in laminated, naturally fractured reservoirs. Conclusions are presented in below:

1. Non–planar multiple fractures propagation in homogenous reservoirs:
   - For the case with high injection fluid viscosity, hydraulic fracturing treatments can generate shorter and wider fractures. Moreover, if the initial horizontal stress difference is small, the pumping schedule should be carefully designed since long time injection using high viscosity fracturing fluid may result in the near–wellbore fracture tortuosity, and it can block proppants transporting through the complex fractures in the near–wellbore damaged region.
   - For the case with small initial horizontal stress difference, simultaneous fracturing is a good choice which can give larger effective fractured area. Using sequential fracturing and alternating fracturing techniques will lead to smaller effective fractured area, and it is highly likely that near–wellbore fracture tortuosity can be generated.
   - For cases with large initial horizontal stress difference, sequential fracturing and alternating fracturing techniques are better choice since they can lead to very large

fractured area at stage 1, and total effective fractured area are larger than the case using simultaneous fracturing technique.

2. Fracture propagation in naturally fractured reservoirs:
    - For multiple fractures propagation in naturally fractured reservoirs, stress shadowing effect plays a key role in fracture network evolution and the opening of NFs.
    - For cases with small values of power law exponent ***a*** (controlling the NF length distribution), results show that fractures tend to propagate along strike orientation of NFs, and the length of fractures opened by tensile failure is increasing.
    - When there are several NF sets (more than two) well developed in a formation, the fracture network propagation direction becomes diversified. This results in complex local induced stress, which may result in strong stress shadowing effect in this specific region. The opened NFs in this specific region will have extremely small fracture width, which can block proppant transportation.
    - For cases with fracture clustering in a designed area, results show that opened fracture density is large and opened fracture network is complex in this area. The complexity suggest that the fracture network not only has high fracture density, but also has diversified fracture propagation directions.
3. Fracture evolution in laminated reservoirs:
    - With the increase of mechanical anisotropy and BP dipping angle, HFs tend to propagate more along BP interfaces, and fracture height is more confined.

- Small BP dipping angle has negligible effect on fracture height and stimulated reservoir volume.
- For the specific ranges of tensile and shear strengths, BP dipping angle and mechanical anisotropy factor, step–over fractures (offset geometry) can be generated. The classical Nolte–Smith interpretation of treating pressures becomes difficult with increasing mechanical anisotropy, larger dipping angles and longer injection times.
- Novel multi–fracture, multi–stage hydraulic fracturing treatment designs have been proposed, which can be utilized to improve hydrocarbon production for laminated shale formations with large thickness and small vertical stress/minimum horizontal stress ratio. The details regarding this design is presented in Section 6.

REFERENCES

Abbas, S., Lecampion, B., and Prioul, R. 2013. Competition between Transverse and Axial Hydraulic Fractures in Horizontal Wells. Presented at the SPE Hydraulic Fracturing Technology Conference, The Woodlands, Texas, 4–6 February. SPE-163848-MS. http://dx.doi.org/10.2118/163848-MS.

Abbs, A. F. and Needham, A. D. 1985. Grouted Piles in Weak Carbonate Rocks. Presented at the Offshore Technology Conference, Houston, Texas, 6–9 May. SPE-4852-MS. http://dx.doi.org/10.4043/4852-MS.

Adachi, J., Siebrits, E., Peirce, A. et al. 2007. Computer Simulation of Hydraulic Fractures. *Int J Rock Mech Min Sci* **44** (5): 739–757. https://doi.org/10.1016/j.ijrmms.2006.11.006.

Al–Busaidi, A., Hazzard, J. F., and Young, R. P. 2005. Distinct Element Modeling of Hydraulically Fractured Lac du Bonnet Granite. *J Geophys Res.* **110** (B6): 2156–2202. http://dx.doi.org/10.1029/2004JB003297.

Alfi, M., Yan, B., Cao, Y. et al. 2015. Microscale Porosity Models as Powerful Tools to Analyze Hydrocarbon Production Mechanisms in Liquid Shale. *J Nat Gas Sci Eng* **26**: 1495–1505. http://doi.org/10.1016/j.jngse.2015.08.002.

AlTammar, M. J. and Sharma, M. M. 2017. Effect of Geological Layer Properties on Hydraulic Fracture Initiation and Propagation: An Experimental Study. Presented at the SPE Hydraulic Fracturing Technology Conference, The Woodlands, Texas, 24–26 January. SPE-184871-MS. http://dx.doi.org/10.2118/184871-MS.

Amadei, B. 1983. *Rock anisotropy and the theory of stress measurements*. Berlin, Germany: Springer-Verlag.

Batchelor, G. K. 1967. *An introduction to fluid dynamics*. Cambridge, UK: Cambridge University Press.

Blanton, T. L. 1986. Propagation of hydraulically and dynamically induced fractures in naturally fractured reservoirs. Presented at the SPE/DOE Unconventional Gas Technology Symposium. Louisville, Kentucky, 18–21 May. SPE-15261-MS. http://dx.doi.org/10.2118/15261-MS.

Bunger, A. P., Zhang, X., and Jeffrey, R. G. 2012. Parameters Affecting the Interaction among Closely Spaced Hydraulic Fractures. *SPE J* **17** (1): 292–306. SPE-140426-PA. https://doi.org/10.2118/140426-PA.

Castonguay, S.T., Mear, M.E., Dean, R.H. et al. 2013. Predictions of the Growth of Multiple Interacting Hydraulic Fractures in Three Dimensions. Presented at SPE Annual Technical Conference and Exhibition, New Orleans, Louisiana, 30 September–2 October. SPE-166259-MS. http://dx.doi.org/10.2118/166259-MS.

Cheng, Y. 2009. Boundary Element Analysis of the Stress Distribution Around Multiple Fractures: Implications for the Spacing of Perforation Clusters of Hydraulically Fractured Horizontal Wells. Presented at the SPE Eastern Regional Meeting, Charleston, West Virginia, 23–25 September. SPE-125769-MS. http://dx.doi.org/10.2118/125769-MS.

Chuprakov, D. A. and Prioul, R. 2015. Hydraulic Fracture Height Containment by Weak Horizontal Interfaces. Presented at the SPE Hydraulic Fracturing Technology

Conference, The Woodlands, Texas, 3–5 February. SPE-173337-MS. http://dx.doi.org/10.2118/173337-MS.

Cipolla, C. L. 2000. State-of-the-Art in Hydraulic Fracture Diagnostics. Presented at the SPE Asia Pacific Oil and Gas Conference and Exhibition, Brisbane, Australia, 16–18 October. SPE-64434-MS. http://dx.doi.org/10.2118/64434-MS.

Cooke, M. L. and Underwood, C. A. 2001. Fracture Termination and Step–over at Bedding Interfaces due to Frictional Slip and Interface Opening. *J Struct Geol* **23** (2): 223–238. https://doi.org/10.1016/S0191-8141(00)00092-4.

Cundall, P. A. 1971. A Computer Model for Simulating Progressive, Large–Scale Movements in Blocky Rock Systems. *Proc.*, Symposium of the International Society for Rock Mechanics, Nancy, France, 5–6 October, 2: 8–12.

Damjanac, B., Board, M., Lin, M.et al. 2007. Mechanical Degradation of Emplacement Drifts at Yucca Mountain—A Modeling Case Study: Part II: Lithophysal Rock. *Int J Rock Mech Min Sci* **44** (3): 368–399. https://doi.org/10.1016/j.ijrmms.2006.07.010.

Daneshy, A. A. 2009. Factors Controlling the Vertical Growth of Hydraulic Fractures. Presented at the SPE Hydraulic Fracturing Technology Conference, The Woodlands, Texas, 19–21 January. SPE-118789-MS. http://dx.doi.org/10.2118/118789-MS.

Daneshy, A. A. 2014. Fracture Shadowing: Theory, Applications and Implications. Presented at the SPE Annual Technical Conference and Exhibition, Amsterdam,

The Netherlands, 27–29 October. SPE-170611-MS. http://dx.doi.org/10.2118/170611-MS.

Dean, R. H. and Advani, S. H. 1984. An Exact Solution for Pistonlike Leak–Off of Compressible Fluids. *ASME J Energy Resour* **106** (4): 539–542.

Dershowitz, W. and Doe, T. W. 2011. Modeling Complexities of Natural Fracturing Key in Gas Shales, *The American Oil & Gas Reporter*, http://www.aogr.com/magazine/cover-story/modeling-complexities-of-natural-fracturing-key-in-gas-shales (accessed August 2011).

Dohmen, T., Zhang, J., and Blangy, J. 2014. Measurement and Analysis of 3D Stress Shadowing Related to the Spacing of Hydraulic Fracturing in Unconventional Reservoirs. Presented at the SPE Annual Technical Conference and Exhibition, Amsterdam, The Netherlands, 27–29 October. SPE-170924-MS. http://dx.doi.org/10.2118/170924-MS.

Dong, Z., Holditch, S. A., McVay, D. et al. 2011. Global Unconventional Gas Resource Assessments. Presented at the SPE Canadian Unconventional Resources Conference, Calgary, Alberta, Canada, 15–17 November. SPE-148365-MS. http://dx.doi.org/10.2118/148365-MS.

Dreuzy, J., Davy, P., and Bour, O. 2001. Hydraulic Properties of Two–Dimensional Random Fracture Networks Following a Power Law Length Distribution: 2. Permeability of Networks based on Lognormal Distribution of Apertures. *Water Resour Res* **37** (8): 2079–2095. http://dx.doi.org/10.1029/2001WR900010.

Economides, M. J. and Nolte, K. G. 2000. *Reservoir Stimulation*, third edition. New York, USA: John Wiley & Sons.

Eisner, L., Thornton, M., and Griffin, J. 2011. Challenges for Microseismic Monitoring. Presented at the 2011 SEG Annual Meeting, San Antonio, Texas, 18–23 September. SEG-2011-1519.

Energy Information Administration. 2016. Annual Energy Outlook 2016 with Projections to 2040. DOE/EIA-0383, U.S. Department of Energy, Washington, DC (15 September 2016).

Energy Information Administration. 2017. Annual Energy Outlook 2017 with Projections to 2050. AEQ 2017, U.S. Department of Energy, Washington, DC (5 January 2017).

Engelder, T., Lash, G. G., and Uzcátegui, R. S. 2009. Joint Sets that Enhance Production from Middle and Upper Devonian Gas Shales of the Appalachian Basin. *AAPG Bull* **93** (7): 857–889. https://doi.org/10.1306/03230908032.

Fidler, L. J. 2011. *Natural fracture characterization of the New Albany Shale, Illinois Basin, United States*. MS thesis, The University of Texas at Austin, Austin, Texas (December 2011).

Fu, P., Johnsonm, S. M., Hao, Y. et al. 2011. Fully coupled geomechanics and discrete flow network modeling of hydraulic fracturing for geothermal applications. *Proc.*, Thirty–sixth workshop on geothermal reservoir engineering, Stanford, California, January 31–February 2, SGP-TR-191.

Gale, J. F., Reed, R. M., and Holder, J. 2007. Natural fractures in the Barnett Shale and their importance for Hydraulic Fracture Treatments. *AAPG bull* **91** (4): 603–622. https://doi.org/10.1306/11010606061.

Gale, J. F., Laubach, S. E., Olson, J. E. et al. 2014. Natural fractures in shale: A review and new observations. *AAPG bull* **98** (11): 2165–2216. https://doi.org/10.1306/08121413151.

Geertsma, J. and de Klerk, F. A. 1969. A rapid method of predicting width and extent of hydraulically induced fractures. *J. Pet Technol* **21** (12): 1571–1781. https://doi.org/10.2118/2458-PA.

Geiser, P., Lacazette, A. and Vermilye, J. 2012. Beyond "dots in a box": An empirical view of reservoir permeability with tomographic fracture imaging. *First Break* **30** (7): 63–69.

Gong, J. and Rossen, W. R. 2014. Modeling Flow in Naturally Fractured Reservoirs: Effect of Fracture Aperture Distribution on Critical Sub–Network for Flow. *Proc.*, 1st International Conference on Discrete Fracture Network Engineering, Vancouver, Canada, 19-22 October.

Grebe, J. J. and Stoesser, M. 1935. Increasing crude production 20,000,000 bbl. from established fields. *World Petroleum J* **August**: 473–482.

Gu, H., Weng, X., Lund, J. B. et al. 2011. Hydraulic fracture crossing natural fracture at non–orthogonal angles, a criterion, its validation and applications. Presented at the SPE Hydraulic Fracturing Technology Conference, The Woodlands, Texas, 24-26 January. SPE-139984-MS. http://dx.doi.org/10.2118/139984-MS.

Guo, T., Zhang, S., Zou, Y. et al. 2015. Numerical Simulation of Hydraulic Fracture Propagation in Shale Gas Reservoir. *J Nat Gas Sci Eng* **26**: 847–856. https://doi.org/10.1016/j.jngse.2015.07.024.

Hamza, F., Chen, C., Gu, M. et al. 2015. Characterization of Anisotropic Elastic Moduli and Stress for Unconventional Reservoirs Using Laboratory Static and Dynamic Geomechanical Data. Presented at the SPE/CSUR Unconventional Reservoirs Conference, Calgary, Alberta, Canada, 20–22 October. SPE-175907-MS. http://dx.doi.org/10.2118/175907-MS.

Han, G. 2011. Natural fractures in unconventional reservoir rocks: identification, characterization, and its impact to engineering design. Presented at the 45th U.S. Rock Mechanics/Geomechanics Symposium, San Francisco, California, 26-29 June. ARMA-11-509.

Hancock, P. L. 1985. Brittle Microtectonics: Principles and Practice. *J Struct Geol* **7** (3-4): 437–457. https://doi.org/10.1016/0191-8141(85)90048-3.

Hodgson, R. A. 1961. Regional study of jointing in Comb Ridge–Navajo Mountain area, Arizona and Utah. *AAPG Bull* **45** (1): 1–38. http://dx.doi.org/10.1306/0BDA6278-16BD-11D7-8645000102C1865D.

Hussain, M., Saad, B., Negara, A. et al. 2016. Hydraulic Fracture Propagation in a Highly Laminated Shale Reservoir with Complex Natural Fracture Network–Case Study Using Higher–Accuracy, Full 3-D Simulation. Presented at the SPE Annual Technical Conference and Exhibition, Dubai, UAE, 26-28 September. SPE-181530-MS. http://dx.doi.org/10.2118/181530-MS.

Israelsson J. I. 1996. Short Descriptions of UDEC and 3DEC. *Developments in Geotechnical Engineering* **79**: 523–528. https://doi.org/10.1016/S0165-1250(96)80041-1.

Itasca. 2007. 3DEC Version 4.1, Three–dimensional Distinct Element Code. Minneapolis, Minnesota: Itasca Consulting Group.

Itasca. 2011. UDEC Version 4.0, Universal Distinct Element Code. Minneapolis, Minnesota: Itasca Consulting Group.

Jaeger, J. C., Cook, N. G. W. and Zimmerman, R. W. 2007. *Fundamental of Rock Mechanics*, fourth edition. Malden, Massachusetts: Blackwell Publishing Ltd.

Khristianovich, S. A. and Zheltov, V. P. 1955. Formation of vertical fractures by means of highly viscous liquid. *Proc.,* 4th world petroleum congress, Rome, Italy, 6–15 June, WPC-6132.

King, G. E. 2012. Hydraulic Fracturing 101: What Every Representative, Environmentalist, Regulator, Reporter, Investor, University Researcher, Neighbor, and Engineer Should Know About Hydraulic Fracturing Risk. Presented at the SPE Hydraulic Fracturing Technology Conference, The Woodlands, Texas, 6-8 February. SPE-152596-MS. http://dx.doi.org/10.2118/152596-MS.

Kresse, O., Weng, X., Gu, H. et al. 2013a. Numerical modeling of hydraulic fracture interaction in complex naturally fractured formations. *Rock Mech Rock Eng* **46** (4): 555–568. https://doi.org/10.1007/s00603-012-0359-2.

Kresse, O., Weng, X., Chuprakov, D. et al. 2013b. Effect of Flow Rate and Viscosity on Complex Fracture Development in UFM Model. Presented at ISRM International

Conference for Effective and Sustainable Hydraulic Fracturing, Brisbane, Australia, 20-22 May. ISRM-ICHF-2013-027.

Klopott, F. 2015. Officially Bans Fracking with Release of Seven-Year Study, *Bloomberg Business*, 29 June 2015, http://www.bloomberg.com/news/articles/2015-06-29/n-y-officially-bans fracking-with-release-of-seven-year-study (accessed 28 January 2016).

Lekhnitskii, S. G. 1963. *Theory of elasticity of an anisotropic body*, first edition. San Francisco, California: Holden-day.

Lemos, J. V. 2011. Recent Developments and Future Trends in Distinct Element Methods-UDEC/3DEC and PFC Codes. *Proc.,* 10th International Conference on Analysis of Discontinuous Deformation, Honolulu, Hawaii, 6-8 December, ICADD-10.

Li, D. Q., Zhang, S. C., and Zhang, S. A. 2014. Experimental and Numerical Simulation Study on Fracturing through Interlayer to Coal Seam. *J Nat Gas Sci Eng* **21**: 386–396. https://doi.org/10.1016/j.jngse.2014.08.022.

Li, H., Zou, Y., Liu, G. et al. 2016a. Prediction of Fracture Initiation Pressure and Fracture Geometries in Elastic Isotropic and Anisotropic Formations. *Rock Mech Rock Eng* **50** (3): 705–717. https://doi.org/10.1007/s00603-016-1002-4.

Li, H., Zou, Y., Valko, P. P. et al. 2016b. Hydraulic Fracture Height Predictions in Laminated Shale Formations Using Finite Element Discrete Element Method. Presented at the SPE Hydraulic Fracturing Technology Conference, The Woodlands, Texas, USA, 9-11 February. SPE-179129-MS. http://dx.doi.org/10.2118/179129-MS.

Lisjak, A., Figi, D., and Grasselli, G. 2014. Fracture development around deep underground excavations: Insights from FDEM modelling. *Journal of Rock Mechanics and Geotechnical Engineering* **6** (6): 493–505. https://doi.org/10.1016/j.jrmge.2014.09.003.

Ma, G., Zhou, W., Chang, X. L. et al. 2014. Combined FEM/DEM Modeling of Triaxial Compression tests for Rockfills with Polyhedral Particles. *Int J Geomech* **14** (4): 0401–4014. https://doi.org/10.1061/(ASCE)GM.1943-5622.0000372.

Mahabadi, O. K., Lisjak, A., Munjiza, A. et al. 2012. Y–Geo: New Combined Finite-Discrete Element Numerical Code for Geomechanical Applications. *Int J Geomech* **12** (6): 676–688.

McClure, M. W. 2012. *Modeling and characterization of hydraulic stimulation and induced seismicity in geothermal and shale gas reservoirs*. PhD Dissertation, Stanford University, Stanford, California (December 2012).

McClure, M., Babazadeh, M., Shiozawa, S. et al. 2015. Fully Coupled Hydromechanical Simulation of Hydraulic Fracturing in Three–Dimensional Discrete Fracture Networks. Presented at the SPE Hydraulic Fracturing Technology Conference, The Woodlands, Texas, 3-5 February. SPE-173354-MS. http://dx.doi.org/10.2118/173354-MS.

McGinley, M., Zhu, D., and Hill, A. D. 2015. The Effects of Fracture Orientation and Elastic Property Anisotropy on Hydraulic Fracture Conductivity in the Marcellus Shale. Presented at the SPE Annual Technical Conference and Exhibition,

Houston, Texas, 28-30 September. SPE-174870-MS. http://dx.doi.org/10.2118/174870-MS.

Meyer, B. R. and Bazan, L. W. 2011. A discrete fracture network model for hydraulically induced fractures: theory, parametric and case studies. Presented at the SPE Hydraulic Fracturing Technology Conference, The Woodlands, Texas, 24-26 January. SPE-140514-MS. http://dx.doi.org/10.2118/140514-MS.

Moës, N., Dolbow, J., and T. Belytschko. 1999. A Finite Element Method for Crack Growth without Remeshing. *Int J Numer Meth Eng* **46**: 131–150. http:// doi.org/10.1002/(SICI)1097-0207(19990910)46:1<131::AID- NME726>3.0.CO;2-J.

Moës, N., Gravouil, A., and Belytschko, T. 2002. Non–planar 3D Crack Growth by the Extended Finite Element and Level Sets – Part I: Mechanical Model. *Int J Numer Meth Eng* **53** (11): 2549–2568. http://dx.doi.org/10.1002/nme.429.

Munjiza, A., Owen, D. R. J., and Bicanic, N. 1995. A Combined Finite–Discrete Element Method in Transient Dynamics of Fracturing Solids. *Eng computation* **12** (2): 145–174. https://doi.org/10.1108/02644409510799532.

Nagel, N. B., and Sanchez–Nagel, M. 2011. Stress Shadowing and Microseismic Events: A Numerical Evaluation. Presented at the SPE Annual Technical Conference and Exhibition, Denver, Colorado, 30 October-2 November. SPE-147363-MS. http://dx.doi.org/10.2118/147363-MS.

Nagel, N. B., Sanchez–Nagel, M., and Lee, B. 2012. Gas shale hydraulic fracturing: a numerical evaluation of the effect of geomechanical parameters. Presented at the

SPE Hydraulic Fracturing Technology Conference and Exhibition, Woodlands, Texas, 6–8 February. SPE-152192-MS. http://dx.doi.org/10.2118/152192-MS.

Nicol, A., Walsh, J. J., and Gillespie, P.A. 1996. Fault size distributions—are they really power–law? *J Struct Geol* **18** (2): 191–197. https://doi.org/10.1016/S0191-8141(96)80044-7.

Nordgren, R.P. 1972. Propagation of a vertical hydraulic fracture. *SPE J* **12** (8): 306–314. SPE-3009-PA. https://doi.org/10.2118/3009-PA.

Odling, N.E. 1997. Scaling and Connectivity of Joint Systems in Sandstones from Western Norway. *J Struct Geol* **19** (10): 1257–1271. https://doi.org/10.1016/S0191-8141(97)00041-2.

Olson, J. E. 2008. Multi-fracture propagation modeling: application to hydraulic fracturing in shales and tight gas sands. Presented at the 42nd US Rock Mechanics Symposum and 2nd U.S.–Canada Rock Mechanics Symposium, San Francisco, June 29-July 2. ARMA-08-327.

Olson, J. E., Bahorich, B., and Holder, J. 2012. Examining hydraulic fracture–natural fracture interaction in hydrostone block experiments. Presented at the SPE Hydraulic Fracturing Technology Conference, The Woodlands, Texas, 6–8 February. SPE-152618-MS. http://dx.doi.org/10.2118/152618-MS.

Ouchi, H., Agrawal, S., Foster, J. T. et al. 2017. Effect of Small Scale Heterogeneity on the Growth of Hydraulic Fractures. Presented at the SPE Hydraulic Fracturing Technology Conference and Exhibition, The Woodlands, Texas, 24–26 January. SPE-184873-MS. http://dx.doi.org/10.2118/184873-MS.

Padin, A., Torcuk, M. A., Katsuki, D. et al. 2016. Experimental and Theoretical Study of Water–Solute Transport in Organic–Rich Carbonate Mudrocks. Presented at the SPE Annual Technical Conference and Exhibition, Dubai, UAE, 26-28 September. SPE-181585-MS. http://dx.doi.org/10.2118/181585-MS.

Perkins, T.K. and Kern, L.R. 1961. Widths of Hydraulic Fractures. *Journal of Pet Technol* **13** (9): 937–949. SPE-89-PA. https://doi.org/10.2118/89-PA.

Philipp S. L., Afsar, F., and Gudmundsson, A. 2013. Effects of Mechanical Layering on Hydrofracture Emplacement and Fluid Transport in Reservoirs. *Front Earth Sci* **1** (4): 1–19. https://doi.org/10.3389/feart.2013.00004.

Pollard, D. D. and Aydin, A. 1988. Progress in Understanding Jointing over the Past Century. *GSA Bulletin* **100**: 1181–1204.

Rafiee, M., Soliman, M. Y., and Pirayesh, E. 2012. Hydraulic Fracturing Design and Optimization: A Modification to Zipper Frac. Presented at the SPE Annual Technical Conference and Exhibition, San Antonio, Texas, 8–10 October. SPE-159786-MS. http://dx.doi.org/10.2118/159786-MS.

Rahman, M. M. and Rahman, M. K. 2010. A Review of Hydraulic Fracture Models and Development of an Improved Pseudo–3D Model for Stimulating Tight Oil/Gas Sand. *Energ Source Part A* **32** (15): 1416–1436.

Rollett, A., Humphreys, F. J., Rohrer, G. S. et al. 2004. *Recrystallization and related annealing phenomena*, second edition. Oxford, UK: Elsevier Science.

Roussel, N. and Sharma, M. 2010. Optimizing fracture spacing and sequencing in horizontal–well fracturing. Presented at the SPE International Symposium and

Exhibiton on Formation Damage Control, Lafayette, Louisiana, 10–12 February. SPE-127986-MS. http://dx.doi.org/10.2118/127986-MS.

Roussel, N. and Sharma, M. 2011. Strategies to Minimize Frac Spacing and Stimulate Natural Fractures in Horizontal Completions. Presented at the SPE Annual Technical Conference and Exhibition held in Denver, Colorado, 30 October–2 November. SPE-146104-MS. http://dx.doi.org/10.2118/146104-MS.

Settari, A. and Cleary, M. P. 1982. Development and Testing of a Pseudo–Three–Dimensional Model of Hydraulic Fracture Geometry. *SPE Prod Eng* **1** (6): 449–466. SPE-10505-PA. https://doi.org/10.2118/10505-PA.

Singh, I. and Miskimins, J. L. 2010. A Numerical Study of the Effects of Packer–Induced Stresses and Stress Shadowing on Fracture Initiation and Stimulation of Horizontal Wells. Presented at the Canadian Unconventional Resources and International Petroleum Conference, Calgary, Alberta, Canada, 19–21 October. SPE-136856-MS. http://dx.doi.org/10.2118/136856-MS

Sneddon, I. N. and Elliot, H. A. 1946. The opening of a Griffith crack under internal pressure. *Quart Appl Math* **4**(3): 262–267.

Sone, H. 2012. *Mechanical properties of shale gas reservoir rocks, and its relation to the in–situ stress variation observed in shale gas reservoirs*. PhD Dissertation, Stanford University, Stanford, California (March 2012).

Suarez–Rivera, R., Burghardt, J., Stanchits, S. et al. 2013. Understanding the effect of rock fabric on fracture complexity for improving completion design and well performance. Presented at the International Petroleum Technology Conference,

Beijing, China, 26–28 March. IPTC-17018-MS. http://dx.doi.org/10.2523/IPTC-17018-MS.

Sun, G., Tan, S., and Korsunsky, A. M. 2016. Review of the Hybrid Finite-Discrete Element Method (FDEM). *Proc.,* World Congress on Engineering, London, UK, June 29–July 1, 2: 843-847.

Suppachoknirun, T., Tutuncu, A. N., and Kazemi, H. 2016. Evaluation of Multistage Hydraulic Fracturing Techniques for Production Optimization in Naturally Fractured Reservoirs Using Coupled Geomechanics Fracture and Flow Model. Presented at International Petroleum Technology Conference, Bangkok, Thailand, 4-16 November. IPTC-18916-MS. http://dx.doi.org/10.2523/IPTC-18916-MS.

Taleghani, A. D. and Olson, J. E. 2009. Analysis of Multistranded Hydraulic Fracture Propagation: An Improved Model for the Interaction Between Induced and Natural Fractures. Presented at the SPE Annual Technical Conference and Exhibition, New Orleans, Louisiana, 4–7 October. SPE-124884-MS. http://dx.doi.org/10.2118/124884-MS.

Tavallali, A. and Vervoort, A. 2010. Effect of layer orientation on the failure of layered sandstone under Brazilian test conditions. *Int J Rock Mech Min Sci* **47** (2): 313–322. https://doi.org/10.1016/j.ijrmms.2010.01.001.

Thiercelin, M., Roegiers, J. C., Boone, T. J. et al. 1987. An investigation of the material parameters that govern the behavior of fractures approaching rock interfaces. Presented at the 6th ISRM Congress, Montreal, Canada, 30 August–3 September. ISRM-6CONGRESS-1987-049.

Thiercelin, M. J., and Plumb, R. A. 1994. A core–based prediction of lithologic stress contrasts in east Texas formations. *SPE Form Eval* **9** (04): 251–258. SPE-21847-PA. https://doi.org/10.2118/21847-PA.

Valko, P. P. and Economides, M. J. 1995. *Hydraulic fracture mechanics*. Chichester, UK: John Wiley & Sons.

Veatch, R. W., and Moschovidis, Z. A. 1986. An Overview of Recent Advances in Hydraulic Fracturing Technology. Presented at the International Meeting on Petroleum Engineering, Beijing, China, 17–20 March. SPE-14085-MS. http://dx.doi.org/10.2118/14085-MS.

Warpinski, N.R. and Teufel, L.W. 1987. Influence of Geologic Discontinuities on Hydraulic Fracture Propagation. *J Pet Technol* **39** (2): 209–220. SPE-13224-PA. https://doi.org/10.2118/13224-PA.

Warpinski, N.R., Kramm, R.C., Heinze, J.R. et al. 2005. Comparison of single– and dual–array microseismic mapping techniques in the Barnett shale. Presented at the SPE Annual Technical Conference and Exhibition, Dallas, Texas, 9–12 October. SPE-95568-MS. http://dx.doi.org/10.2118/95568-MS.

Waters, G. A., Heinze, J. R., Jackson, R. et al. 2006. Use of Horizontal Well Image Tools to Optimize Barnett Shale Reservoir Exploitation. Presented at the SPE Annual Technical Conference and Exhibition, San Antonio, Texas, 24–27 September. SPE-103202-MS. http://dx.doi.org/10.2118/103202-MS.

Weng, X., Kresse, O., Cohen, C. et al. 2011. Modeling of hydraulic fracture network propagation in a naturally fractured formation. Presented at the SPE Hydraulic

Fracturing Technology Conference, The Woodlands, Texas, 24–26 January. SPE-140253-MS. http://dx.doi.org/10.2118/140253-MS.

Weng, X. 2015. Modeling of Complex Hydraulic Fractures in Naturally Fractured Formation. *Journal of Unconventional Oil and Gas Resources* **9**:114–135. https://doi.org/10.1016/j.juogr.2014.07.001.

Williams–Stroud, S., Kilpatrick, J. E., Eisner, L. et al. 2010. Natural Fracture Characterization from Microseismic Source Mechanisms: A Comparison with FMI Data. Presented at the Canadian Unconventional Resources and International Petroleum Conference, Calgary, Alberta, Canada, 19–21 October. SPE-138107-MS. http://dx.doi.org/10.2118/138107-MS.

Wu, K. and Olson, J. E. 2014. Mechanics analysis of interaction between hydraulic and natural fractures in shale reservoirs. Presented at the Unconventional Resources Technology Conference (URTEC), Denver, Colorado, 25-27 August. URTEC-1922946-MS. http://dx.doi.org/10.15530/URTEC-2014-1922946.

Wu, K. 2014. *Numerical Modeling of Complex Hydraulic Fracture Development in Unconventional Reservoirs*. PhD dissertation. The University of Texas at Austin, Austin, Texas (December 2014).

Wu, K. and Olson, J. E. 2015a. Simultaneous Multifracture Treatments: Fully Coupled Fluid Flow and Fracture Mechanics for Horizontal Wells. *SPE J* **20** (02): 337–346. SPE-167626-PA. https://doi.org/10.2118/167626-PA.

Wu, K. and Olson, J. E. 2015b. Numerical Investigation of Complex Hydraulic Fracture Development in Naturally Fractured Reservoirs. Presented at the SPE Hydraulic

Fracturing Technology Conference, The Woodlands, Texas, 3–5 February. SPE-173326-MS. http://dx.doi.org/10.2118/173326-MS.

Wong, S. W., Geilikman, M., and Xu, G. 2013. Interaction of Multiple Hydraulic Fractures in Horizontal Wells. Presented at the SPE Unconventional Gas Conference and Exhibition, Muscat, Oman, 28-30 January. SPE-163982-MS. http://dx.doi.org/10.2118/163982-MS.

Zhang, X. and Jeffrey, R. G. 2007. Hydraulic fracture propagation across frictional interfaces. Presented at the 1st Canada–U.S. Rock Mechanics Symposium, Vancouver, Canada. 27-31 May. ARMA-07-204.

Zhao, Q., Lisjak, A., Mahabadi, O. et al. 2014. Numerical Simulation of Hydraulic Fracturing and Associated Microseismicity using Finite–Discrete Element Method. *Journal of Rock Mechanics and Geotechnical Engineering* **6** (6): 574–581. https://doi.org/10.1016/j.jrmge.2014.10.003.

Zhi, Y. and Ahmad, G. 2016. Deformation Properties of Saw–Cut Fractures in Barnett, Mancos and Pierre Shales. Presented at the 50th U.S. Rock Mechanics/Geomechanics Symposium, Houston, Texas, 26-29 June. ARMA-16-420.

Zhou, T., Zhang, S., Zou, Y. et al. 2016. A Study of Hydraulic Fracture Geometry Concerning Complex Geologic Condition in Shales. Presented at the International Petroleum Technology Conference, Bangkok, Thailand, 14-16 November. IPTC-19014-MS. http://doi.org/10.2523/IPTC-19014-MS.

Zivaljic, N., Smoljanovic, H., and Nikolic, Z. 2013. A Combined Finite–Discrete Element Model for RC Structures under Dynamic Loading. *Eng computation* **30** (7): 982–1010. https://doi.org/10.1108/EC-03-2012-0066.

Zou, Y. 2015. *Investigation into the Mechanism of Fracture–network fracturing in Shale Gas Reservoirs*. PhD dissertation. China University of Petroleum, Changping, Beijing, China (July 2015).

Zou, Y., Zhang, S., Zhou, T. et al. 2016. Experimental Investigation into Hydraulic Fracture Network Propagation in Gas Shales using CT Scanning Technology. *Rock Mech Rock Eng* **49** (1): 33–45. https://doi.org/10.1007/s00603-015-0720-3.